THE SEARCH FOR DARK MATTER ANNIHILATION IN GALAXY CLUSTERS AT VERITAS

A Dissertation

Submitted to the Faculty

of

Purdue University

by

James V. Tucci

In Partial Fulfillment of the

Requirements for the Degree

of

Doctor of Philosophy

May 2016

Purdue University

West Lafayette, Indiana

To my wife Elissa, and my parents Lisa and Stephen

ACKNOWLEDGEMENTS

There are many people in my life I would like to give thanks for. They have each contributed in their own way to my academic career and the progression of this document. To Drs. Lister, Peterson, and Kruczenski, thank you for teaching the classes that sparked my interest to learn more about this field. Thank you for your patience and sound advice to help my thesis ideas take root and grow. To my mentor Dr. Finley, thank you for your wisdom and wit. You are the drive that propelled my mind to new meaning after each meeting. You have given me many opportunities that have made me a better scientist. And you have done it all with a joviality that is rare to find these days.

To my Purdue colleagues Ben, Mark, Angelo, Qi, Suzanne, and Brett, thank you for your support during this process. I gained a lot of exposure to a wide variety of topics as I followed your papers and scripts to completion. To Glenn, thank you for teaching me everything I needed to know about data analysis and servers. I ended up switching computer clusters no less than three times during my analysis for various reasons, and each time you helped ease that transition. To Pascal, thank you for making my extended site visit so rewarding. I have a much fuller understanding of the hardware aspects of VERITAS because of you.

From the VERITAS main wikipage: “This research is supported by grants from the U.S. Department of Energy Office of Science, the U.S. National Science Foundation and the Smithsonian Institution, and by NSERC in Canada. We acknowledge the excellent work of the technical support staff at the Fred Lawrence Whipple Observatory and at the collaborating institutions in the construction and operation of the instrument.”

“The VERITAS Collaboration is grateful to Trevor Weekes for his seminal contributions and leadership in the field of very high energy γ-ray astrophysics, which made this study possible.” I was fortunate to spend time with him during the last year of his life when I spent a semester at VERITAS in 2013. Rest in peace, Trevor.

To my family, thank you for providing the opportunities and nourishment to let me follow my dreams. You have showed me the way and I will go far. Your love is how I know I will make the world a better place.

To my wife Elissa, thank you for the endless support during this experience. Your fun energy and great smile are what have kept my spirits high even when I could not find my way. I look forward to many more years of happy marriage with you.

TABLE OF CONTENTS

Page

LIST OF TABLES

Table Page

LIST OF FIGURES

Figure Page

Figure Page

Figure Page

Figure Page

Figure Page

Figure Page

ABSTRACT

Tucci, James V. Ph.D., Purdue University, May 2016. The Search for Dark Matter Annihilation in Galaxy Clusters at VERITAS. Major Professor: John P. Finley.

Recent data and cosmological models point to a significant fraction of the Universe comprised of Cold Dark Matter (DM), though little is known about it directly as it does not interact electromagnetically. The most likely explanation for DM is a Weakly Interacting Massive Particle (WIMP) having a mass as low as ~10 GeV to as high as ~10 TeV. Many direct and indirect detection schemes have been proposed to search for the elusive particle. Galaxy clusters, consisting of hundreds to thousands of galaxies, are the largest collections of matter in the Universe held together by gravity. As such, galaxy clusters also contain the highest concentrations of DM found anywhere. Observational evidence for DM can be found in the rotational velocity curves of galaxies as well as gravitational lensing around galaxy clusters. WIMPs are believed to be their own antiparticles and self-annihilate into a variety of lighter quarks, leptons, bosons, and γ-rays. VERITAS (Very Energetic Radiation Imaging Telescope Array System) is composed of four 12-meter Imaging Atmospheric Cherenkov Telescopes (IACTs) that can detect the γ-ray signature of DM annihilation.

This thesis presents results on the VERITAS observations of 12 galaxy clusters. We seek to detect the γ-rays originating from the DM interactions within clusters. If a DM detection is not made, the limit to thermally-averaged DM annihilation velocity-weighted cross-section can then computed from the γ-ray flux upper limit. Then it is seen whether the limit can be improved by combining the different datasets with a stacking procedure.

CHAPTER 1. DARK MATTER IN GALAXY CLUSTERS

1.1 Dark Matter Properties

Dark matter (DM) is an elusive form of matter that comprises 84.5% of the mass of the Universe (DM is 26.8%, luminous matter is 4.9%, and dark energy is 68.3% of the total mass-energy density) [1]. Telescopes cannot observe it directly as it does not interact electromagnetically, but we can infer its presence from its gravitational effects on neighboring stars and galaxies. The most popular interpretation for DM is that it is a weakly interacting massive particle (WIMP). Competing theories include exotic particles like axion-like particles (ALPs) or sterile neutrinos to account for the observed properties [2] [3]. Additionally theories such as modified Newtonian dynamics (MOND) or tensor-vector-scalar gravity (TeVeS) claim that gravitational anomalies in massive systems give rise to the perceived missing mass [4] [5]. This work will focus on DM arising from WIMPs within the constraints of Lambda Cold Dark Matter (ΛCDM) cosmology, the accepted standard model for large-scale structure formation arising from non-relativistic DM.

According to this current cosmological theory, in the early Universe when the average temperature exceeded the WIMP mass (i.e., $k_B T > M_\chi c^2$) a balance between the amount of WIMPs and photons that were spontaneously created or annihilated was established for a time. Once the temperature dropped below the WIMP mass, the number of WIMPs began to fall exponentially. WIMPs are believed to be stable particles but also are their own antiparticle, hence they self-annihilate via the weak interaction into photons or other lighter particles. Eventually the combination of the Universe's expansion and the

annihilation of WIMPs shrank the WIMP number density to the point that further annihilations were unlikely to occur. As time went on, the mean free path for WIMP interactions extended out to the Hubble distance, thus fixing the interaction cross-section [6]. This remnant of the hot Universe called the thermal relic is present today and has the value:

$$\langle \sigma v \rangle_{WIMP} \approx 3 \times 10^{-26} \frac{cm^3}{sec} \quad (1.1)\ [7]$$

where $<\sigma v>_{WIMP}$ is the velocity-weighted cross-section for WIMP annihilation. This estimated value arising from the time-dependent Boltzmann equation has remained essentially unchanged since the early Universe due to the freeze-out process described above. It also fits the measured DM density of several cosmological datasets including the Planck survey, baryon acoustic oscillations, and Type 1a supernovae lightcurves. The ratio of the DM density to the critical density of the Universe (see Section 1.5) is given as:

$$\Omega_{DM} h^2 = 0.1123 \pm 0.035 \quad (1.2)$$

where Ω_{DM} is the DM density and h is the dimensionless Hubble parameter at the current epoch ($z = 0$) [8] [9]. Alternatively, theories for the decay of DM into other Standard Model particles have been proposed with the decay time being a free parameter.

At Earth (8.33 kpc from the center of the Milky Way) the DM density has been estimated to be 0.3 ± 0.1 GeV/cm^3 [10]. The DM takes the form of a large spherical halo around the Milky Way galaxy. DM must be present in this concentration for the Solar System and other stars to traverse the galaxy in orbits that satisfy the Jeans equation and other best-fit halo models. The evolution of the halo and substructures traces the hierarchical development of the galaxy. The standard picture from numerical simulations is that smaller clumps of DM coalesced with the galaxy's halo over megayears (Myrs), growing in size similar to the way smaller satellite galaxies merged with the galaxy's disk [11]. While DM does clump under the influence of self-gravity, it should not virialize or

form a disk because DM is believed to be nearly collisionless. It does not have to transfer and lose angular momentum the way interacting gas and dust do during collapse [12].

1.2 Evidence for Dark Matter

The Swiss astronomer Fritz Zwicky was the first to surmise the presence of DM which he termed *dunkle materie*. He noticed something unusual about the movement of galaxies within the Coma cluster (Abell 1656). He applied the time-averaged virial theorem:

$$2\bar{T} + \bar{\Omega} = 0 \quad (1.3)$$

where T is the average kinetic energy of the galaxies in the cluster and Ω is the average gravitational potential energy of the cluster. The value of Ω he arrived at by summing up the potentials of the galaxies was ~400 times smaller than the measured kinetic energy required to keep the system in equilibrium. The gravitational influence of the luminous matter alone was unable to account for the rapid motions of the individual galaxies. The result, that dark matter is present in much larger quantities than luminous matter, surprised him greatly [13]. While later studies of the Coma cluster revealed a slightly lower mass-to-light ratio (M/L) of ~350 (from improved mass resolution), the critical importance of his discovery continues to shape the face of modern astrophysics [14].

The velocity of stars orbiting around the center of a galaxy should fall off as a function of the radial distance$^{-0.5}$ if bound by the gravity of the luminous matter that is mostly concentrated in the bulge of the galactic disk. Keplerian orbital dynamics for stars outside of the bulge gives:

$$F_{cent} = \frac{GMm}{R^2} = \frac{mv^2}{R}, \qquad v = \sqrt{\frac{GM}{R}} \quad (1.4)$$

Within the bulge, the velocity increases proportionally to *R*. In the 1970's Vera Rubin made measurements of local galaxies with a high-resolution spectrograph. Her observations indicated that the radial velocity curves stay flat out to large radii [15]. Figure 1-1 points out the discrepancy between the observed and expected radial velocity curve for the galaxy NGC 3198. The missing mass is believed to lie in a spherical halo of dark matter around the galaxy.

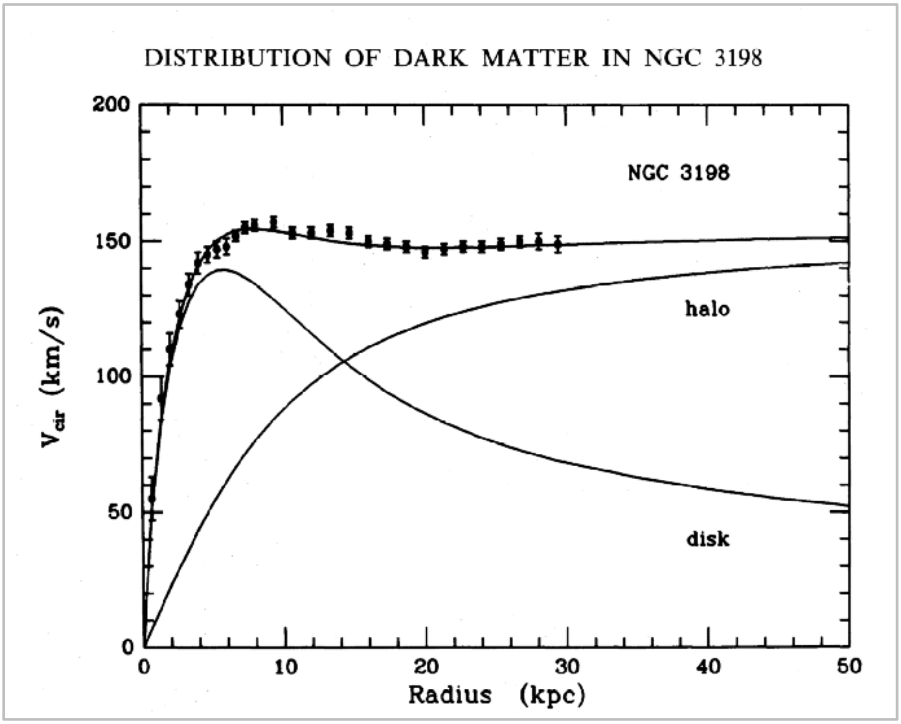

Figure 1-1: NGC 3198 galactic rotation profile (credit: T. S. van Albada [16]). The points with error bars are the observed radial velocities of stars in the galaxy. The three curves are model predictions of the relative gravitational strengths on the radial velocity. The halo curve (DM) plus the disk (galactic bulge) curve yield the combined model prediction.

Another place the effects of DM can be observed is in the gravitational lensing of distant galaxies by intervening galaxy clusters. Gravitational lensing is divided into two categories: strong and weak. In strong lensing the lightpath of the background galaxy becomes distorted from passing in close proximity to the curved space-time of the

massive cluster. The galaxy image seen from Earth appears as an arc of light. Certain spatial configurations will also give rise to an unbroken ring around the cluster known as an Einstein ring. If the light takes separate paths around the cluster and reconverges at Earth then multiple copies of the background galaxy will be visible. In weak lensing however, the degree of distortion is much lower so its effect is not immediately obvious. Instead analysis software measures the shapes and orientations of hundreds of galaxies in the field. The galaxies will shear perpendicularly with respect to the displacement vector between them and the center of the foreground cluster. From that an estimate of the cluster mass can be inferred. Both lensing methods confirm that there is significantly more gravitational mass present in galaxy clusters than can be accounted for solely by luminous matter [17]. Figure 1-2 shows possible paths the light from a distant galaxy might take towards Earth.

One of the more striking cases for the existence of DM is the Bullet cluster at a redshift of 0.3 (1.1 Gpc distant). The cluster is actually the result of a recent merger between two galaxy clusters. In the middle of the cluster is a region of extremely hot, shocked plasma ($T \sim 10^8$ K) called the intracluster medium (ICM) that is visible in X-rays. Two large bow shocks bearing some semblance to a bullet exiting a rifle pointed in opposite directions reveal the nature of the merging plasma. The galaxies in the merger have crossed through the central region with little interaction and are concentrated in lobes on either side. Though the plasma is diffuse, it contains an order of magnitude more mass than the galaxies. Weak lensing maps however place the gravitational center of mass of each lobe coincident with the galaxies, not the plasma. Evidently the DM haloes of the two original clusters, containing yet another order of magnitude more mass than the ICM, crossed paths in the center but only interacted gravitationally in a very limited way. They did not stay trapped in the central region and thus became disentangled from the X-ray emitting plasma cloud. This finding favors DM composed of WIMPs over MOND or TeVeS at the 8 σ level [18]. Figure 1-3 shows on the left panel a Magellan Telescopes optical image of the galaxies and on the right panel a Chandra X-ray Observatory image of the plasma both overlaid with weak lensing DM contours.

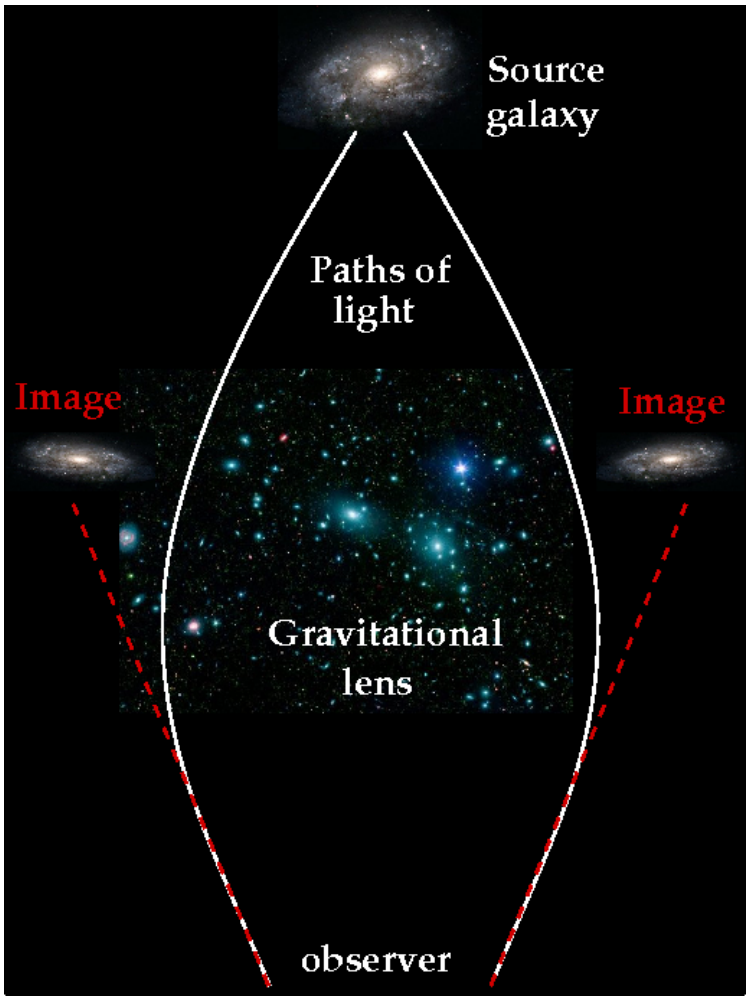

Figure 1-2: Gravitational lensing concept (credit: Matthew Francis [19])

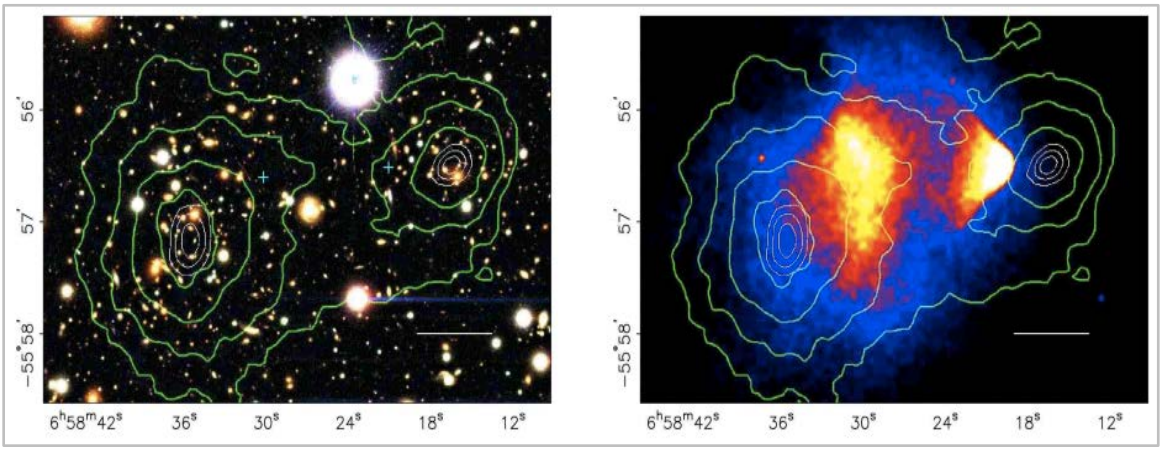

Figure 1-3: 1E 0657-558 or the Bullet cluster (credit: Jesse Rogerson [20]). Left: optical, Right: X-rays. The weak lensing contours show the mass distribution concentrated in two lobes.

1.3 DM Detection Searches and Experiments

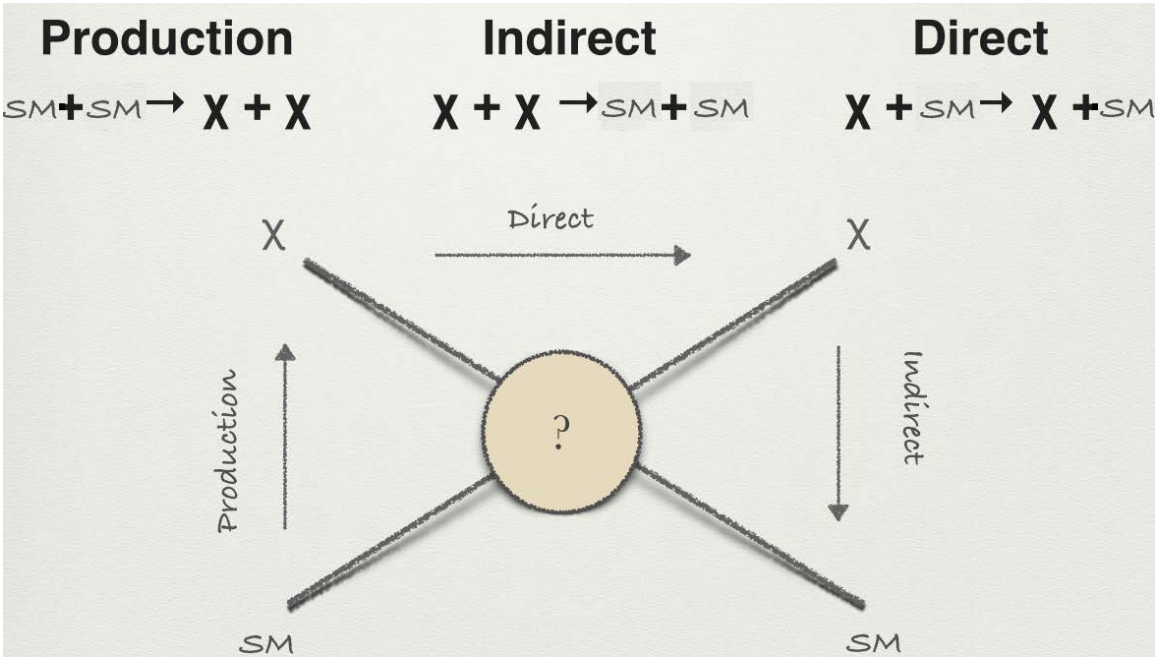

Figure 1-4: The three schemes to detect signatures of DM (credit: Sally Shaw [21]). The graphic can proceed in any of the three orientations to give valid Feynman diagrams for direct production, indirect detection, or direct detection. Here, χ represents the WIMP and SM stands for a variety of possible standard model final states (see Table 1-1).

Many current and proposed experiments have sought to uncover the nature of the mysterious WIMP. They broadly fall into three categories: direct DM detection, indirect DM detection, and direct production experiments. Direct DM detection searches look for the recoil of a WIMP interacting with an atom in the detector. The detector consists either of a large block of supercooled scintillator crystal or a large tank of a liquefied, heavy noble gas. A WIMP interaction with an atom in the crystal, typically germanium or calcium tungstate, will produce photons and also raise the temperature of the experiment slightly via ionization. Electronics read out the signal from the crystal and perform calorimetry measurements to determine if a DM interaction has taken place. WIMP

nuclear recoils are predicted to produce lower ionization than α- or β-decays do. Some examples of this type are CRESST, CDMS, and EDELWEISS [22] [23] [24].

In the other type, noble gases like argon or xenon serve as the targets for WIMP interactions. Photomultiplier tubes on the edge of the experiment pick up the light produced when a WIMP recoils off one of the atoms in the tank. Examples include ArDM, XENON, and LUX [25] [26] [27]. These experiments are buried under kilometers of rock in underground mines or deep within mountains to reduce contamination from atmospheric muons. Lead shielding and veto layers prevent the natural radioactivity of the surrounding rock from impacting their measurements. Direct detection experiments are typically most sensitive to DM in the 5 – 100 GeV mass range. Figure 1-5 offers a sensitivity comparison of the direct DM detection experiments.

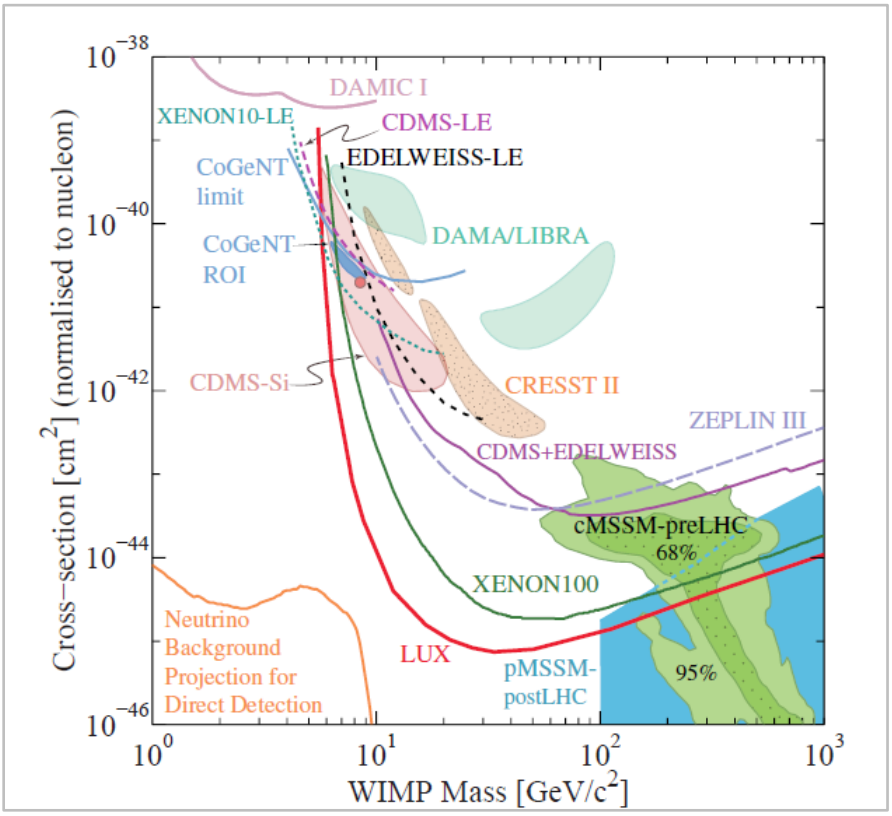

Figure 1-5: Experiment sensitivity as cross-section vs. mass
(credit: Particle Data Group [28])

Alternatively, indirect DM detection searches look for the visible byproducts after an annihilation has occurred. Dark matter is believed to be its own antiparticle and multiple annihilation channels exist. Table 1-1 lists many of the possible annihilation channels. Note how the final states of most DM annihilations include γ-rays [29]. Popular astrophysical targets for indirect DM detection include dwarf spheroidal galaxies (dSphs), galaxy clusters, and the Galactic Center (GC). The following Sections 1.3.1 through 1.3.5 detail the current and next generations of γ-ray observatories and their indirect DM annihilation programs. Section 1.3.6 describes the work being done at the Large Hadron Collider for production of new DM for the first time since the DM freeze-out in the early Universe. VERITAS will be covered in Section 2.4 .

1.3.1 Fermi-LAT

The Fermi-LAT (Large Area Telescope) is a 0.8 m^2 pair-production imaging device consisting of silicon microstrip detectors and cesium iodide scintillator crystals onboard its parent satellite sensitive to γ-rays with energy 20 MeV to 300 GeV [30]. It is named in honor of Enrico Fermi who won the Nobel Prize in 1938 for pioneering work on neutron physics [31]. It was launched into Low Earth Orbit (mean height 545 km) on June 11, 2008 aboard a Delta II rocket from Cape Canaveral, FL. The LAT can survey one sixth of the sky at any given time (~2 sr) and completes an orbit every 95 minutes. It can resolve sources with an angular resolution < 0.15° at GeV energies [32].

In a 2014 paper, it derived stringent limits on WIMP DM annihilation from 25 dwarf spheroidal galaxies (dSphs) using a joint stacking analysis [33]. A search for DM annihilation line emission (directly to two γ-rays) using the LAT's highest energy photons produced some promising excesses around 130 GeV but were not quite strong enough for a detection [34] [35].

Figure 1-6: Fermi-LAT satellite (credit: Aurore Simmonet [36])

1.3.2 HESS

The High Energy Stereoscopic System (HESS) is an array of five γ-ray telescopes located in the Khomas Highlands of Namibia (23.27° S, 16.50° E, 1,800 meters above sea level) [37]. HESS is better suited to see sources in the Southern sky, in contrast to VERITAS or MAGIC. It is named in honor of Victor Hess who won the Nobel Prize in 1936 for his discovery of cosmic-rays aboard balloon flights [38]. The HESS-I array, finished in 2003, consisted of the four outer telescopes evenly spaced by 120 meters similar in size and performance to VERITAS. The large middle telescope HESS-II was added in 2012 and reduced the energy threshold to 30 GeV [39] [40].

HESS has taken data on Southern Hemisphere dSphs looking for signatures of DM annihilation there as well [41]. The Galactic Center culminates at a much lower

zenith angle for HESS than for VERITAS or MAGIC [42], so HESS results on the GC give more stringent DM limits at higher energies on an exclusion plot [43].

Figure 1-7: HESS-I (four 12-meter telescopes) and HESS-II (28-meter telescope) (credit: Hans van de Groenendaal [44])

1.3.3 MAGIC

The Major Atmospheric Gamma Imaging Cherenkov (MAGIC) telescopes are a pair of γ-ray telescopes located at the Roque de los Muchachos Observatory on La Palma in the Canary Islands (28.76° N, 17.89° W, 2,200 meters above sea level) [45]. The first telescope MAGIC-I came online in 2004 followed by MAGIC-II in 2010 [46]. MAGIC-II has an identical design and sits 85 meters away. The large mirror surfaces allow MAGIC to detect the Cherenkov light from lower energy γ-ray photons, giving a threshold energy of 25 GeV [47] [48].

MAGIC has taken deep observations on the same dSph galaxies that VERITAS sees because both observatories lie at roughly the same Northern latitude (e.g., Segue 1 [49], Draco [50], or Willman 1 [51]). Additionally they have taken observations on the Perseus cluster and the active galaxy NGC 1275 at its center to separate and categorize the galactic and DM annihilation components of the γ-ray signal [52] [53]).

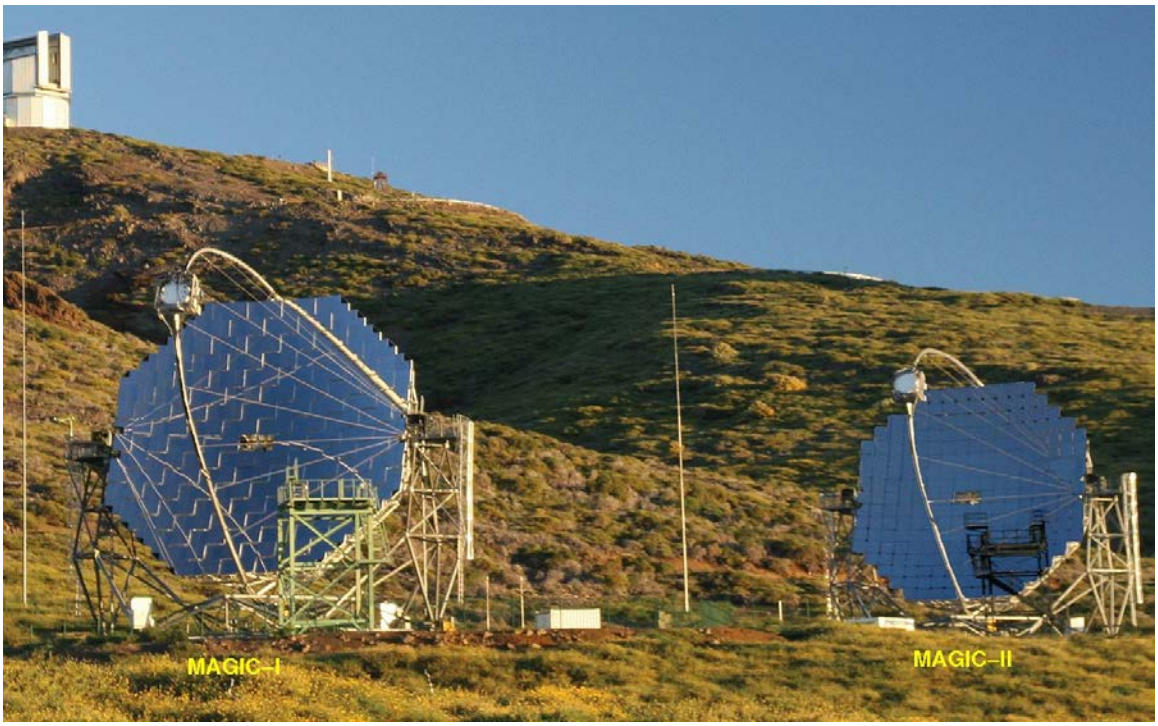

Figure 1-8: MAGIC-I and MAGIC-II (two 17-meter telescopes)
(credit: ETH Institute for Particle Physics [54])

1.3.4 HAWC

The High Altitude Water Cherenkov (HAWC) Experiment is a γ-ray and cosmic-ray observatory located in the Pico de Orizaba National Park in Mexico (18.99° N, 97.31° W, 4,100 meters above sea level) [55]. It consists of 300 large tanks each holding 188 m^3 of purified water. The final tank was completed in early 2015. The secondary charged particles from γ-rays/cosmic-rays enter the top of a tank and produce Cherenkov radiation

(see Section 2.1) with a much higher opening angle than in air (41° vs. 1°). Instead of using several tens of kilometers of atmosphere to propagate the Cherenkov flash, all this fits within the five meter height of the tank [56]. The observatory takes data 24 hours a day and samples one sixth of the sky (~2 sr) at any given time. It is sensitive to γ-rays/cosmic-rays with energies from 100 GeV to 100 TeV [57].

Although the angular resolution of HAWC is much broader than the "pencil-beam" ground-based observatories, HAWC attains far greater sky coverage each year. γ-ray sources were not well-localized (>5° error circle on the sky) before the full array was operational, but the increased dataset is shrinking sources' error circles on the HAWC combined skymap [58]. This improved sensitivity is allowing HAWC to probe promising DM targets including dSphs, M31, the Virgo cluster, and the GC. After several years of operation, the full array will have better sensitivity to multi-TeV WIMP annihilation than the other current observatories [59] [60].

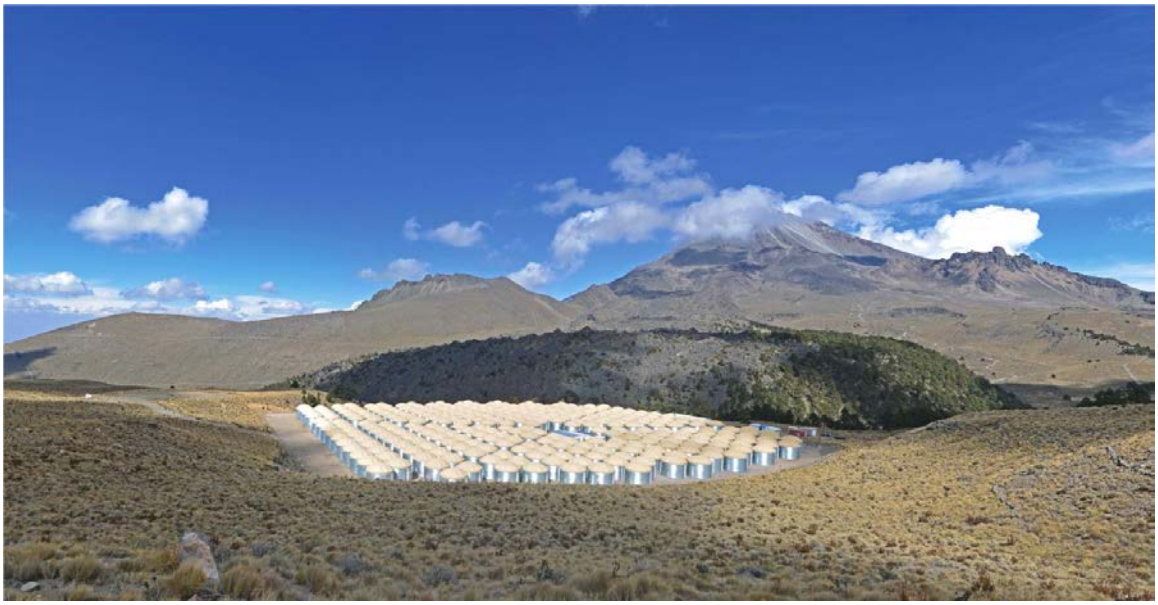

Figure 1-9: A view of HAWC (credit: HAWC Collaboration [61])

1.3.5 CTA

The Cherenkov Telescope Array (CTA) is the next generation of γ-ray observatory that is expected to make its first light in 2020 [62]. CTA will consist of two complementary sites: 100 telescopes arranged over 4 km^2 in the Southern Hemisphere and 19 telescopes arranged over 0.4 km^2 in the Northern Hemisphere. In the summer of 2015 a site selection team chose Paranal, Chile for the Southern site and La Palma for the Northern site. Both sites will have 4 large-size telescopes similar in size to HESS-II and 15 or 24 (North and South, respectively) medium-size telescopes similar in size to VERITAS or HESS-I. Additionally CTA South will have 72 small-size telescopes that are half the size of the medium-size telescopes and will catch the signatures of the most energetic γ-rays [63].

The observatory will boast sensitivity an order of magnitude greater than current arrays and will detect γ-rays with energy 10 GeV to 100 TeV [64] [65]. This sensitivity boost should allow CTA to probe for DM approaching the thermal relic value at much higher energies than the current arrays can achieve. For further information on CTA, the journal Astroparticle Physics dedicated its entire March 2013 edition (volume 43) to the science explored by CTA [66].

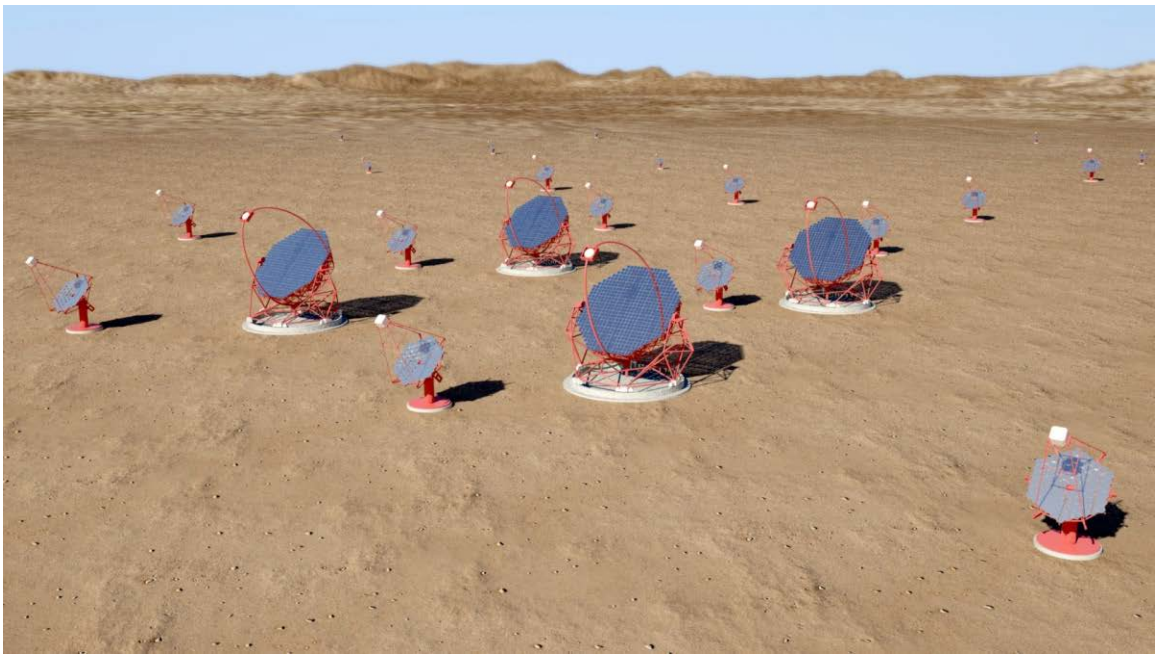

Figure 1-10: Computer rendering of the proposed CTA South site
(credit: Gabriel Pérez Díaz [67])

1.3.6 LHC

The Large Hadron Collider (LHC) is a 27-kilometer circumference particle accelerator located along the border of France and Switzerland near Geneva. The beamline is buried 100 meters below ground to minimize the contaminating effects of atmospheric radiation. 1,232 superconducting NbTi dipole magnets cooled to 1.9 K by liquid helium cryostats and carrying 11.7 kA deliver 8.3 T to bend the path of the ultrarelativistic protons (or lead ions) through the experiment. Radio frequency cavities accelerate both counterrotating proton beams to energies up to 7 TeV and congregate them into 2,808 ‘bunches,’ represented as the colored dots in Figure 1-11. Each bunch carries around 10^{11} protons and traverses the ring 11,000 times a second. Bunch crossings occur at the four major experiments where the proton flux, called ‘luminosity’ in particle physics, rises to 10^{34} $cm^{-2}s^{-1}$. The experiments record a combined 600 million *pp* collisions every second. The experiments’ sophisticated, layered design of the silicon

tracker plus the electromagnetic, hadronic, and muonic calorimeters facilitates complete particle track reconstruction of a collision [68].

A notable milestone in the timeline of the LHC's operation came in 2012 with the discovery of the 125 GeV Higgs boson. CERN scientists are actively running a number of campaigns to search for new physics at higher energies, several of which include DM detection [69]. The interaction of two or more quarks in a 14 TeV (center-of-mass) *pp* collision creates conditions energetically favorable for the direct production of multi-TeV WIMPs. Once created, the WIMPs would exit the LHC leaving no trace. However, their absence in the particle track reconstruction does not go unnoticed. An asymmetry in the direction of the jets of particles produced from the collision will stand out. Energy must be conserved, therefore this asymmetric missing transverse energy can be accounted for by the fleeting WIMPs [70] [71].

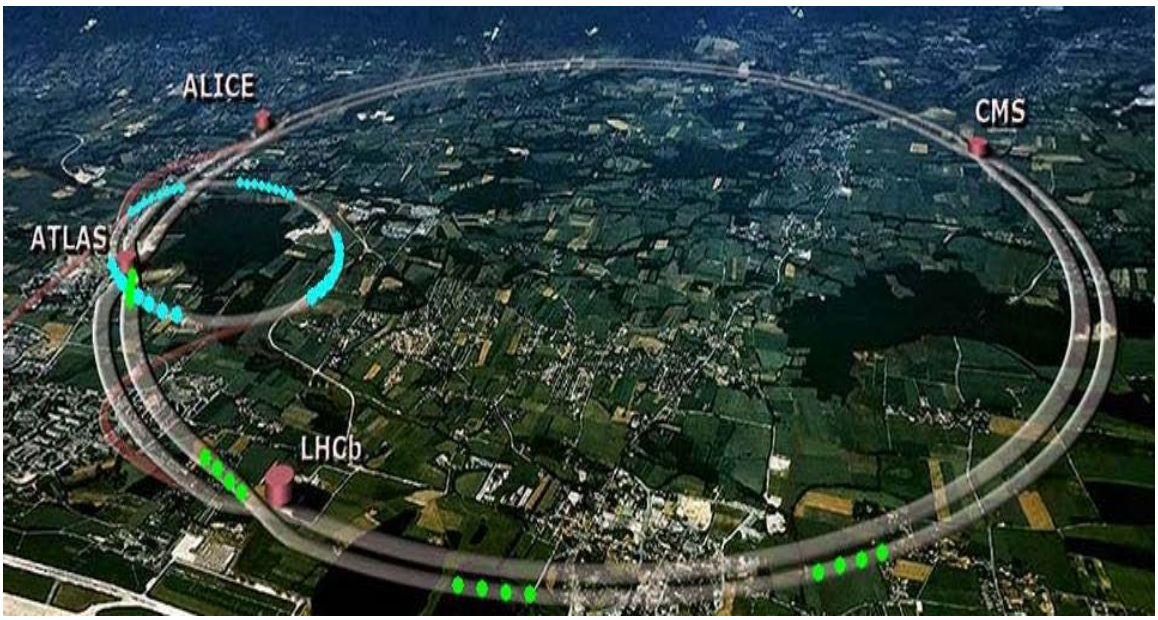

Figure 1-11: The LHC with major experiments' locations marked
(credit: Ethan Siegel [72])

1.4 DM Annihilation Channels and γ-Ray Flux Production

Table 1-1: Various WIMP annihilation channels (credit: Jim Buckley [73])

Annihilation Channel	Secondary Decays	Signatures
$\chi + \chi \rightarrow Z^0 + Z^0$	$Z^0 \rightarrow l^+ + l^-$, $Z^0 \rightarrow \nu_l + \bar{\nu}_l$, $Z^0 \rightarrow q + \bar{q} \rightarrow \pi's$ $\pi^0 \rightarrow \gamma + \gamma$, $\pi^+ \rightarrow \mu^+ + \nu_\mu$, $\pi^- \rightarrow \mu^- + \overline{\nu_\mu}$	$p, e, \nu, \boldsymbol{\gamma}$
$\chi + \chi \rightarrow W^+ + W^-$	$W^+ \rightarrow l^+ + \nu_l$, $W^- \rightarrow l^- + \bar{\nu}_l$, $W^\pm \rightarrow u\bar{d}/d\bar{u} \rightarrow \pi's$	$p, e, \nu, \boldsymbol{\gamma}$
$\chi + \chi \rightarrow q + \bar{q}\ or\ g + g$	$q + \bar{q} \rightarrow p + \bar{p} + \pi's$ $g + g \rightarrow p + \bar{p} + \pi's$	$p, e, \nu, \boldsymbol{\gamma}$
$\chi + \chi \rightarrow \tau^+ + \tau^-$	$\tau^\pm \rightarrow \nu_\tau + l^\pm + \nu_l/\bar{\nu}_l$, $\tau^\pm \rightarrow \nu_\tau + W^\pm \rightarrow \pi's$	$p, e, \nu, \boldsymbol{\gamma}$
$\chi + \chi \rightarrow \mu^+ + \mu^-$	$\mu^+ \rightarrow e^+ + \overline{\nu_\mu} + \nu_e$, $\mu^- \rightarrow e^- + \overline{\nu_e} + \nu_\mu$	$e, \nu, \boldsymbol{\gamma}$
$\chi + \chi \rightarrow e^+ + e^-$	$e^+ + e^- \rightarrow \gamma + \gamma$	$e, \boldsymbol{\gamma}$
$\chi + \chi \rightarrow \gamma + \gamma$		$\boldsymbol{\gamma}$
$\chi + \chi \rightarrow \nu_l + \bar{\nu}_l$		ν

As seen in Table 1-1, there are many ways for annihilating DM to produce γ-rays. The seventh channel illustrates the most direct route to γ-rays. This process would show up as a sharp line in the γ-ray energy spectrum peaking at the WIMP mass. The other decay modes generate γ-rays through hadron fragmentation and the decays of secondary particles, usually the bremsstrahlung of pions (see Section 2.2). These modes would tend to produce a broader, continuum emission in the γ-ray spectrum. Another possibility is that additional γ-ray photons are produced somewhere in the middle of the chain before the final decay products. This process called internal bremsstrahlung would produce an admixture of line and continuum emission [74].

The DM annihilation proceeds through one or more of these processes within the cluster. It is possible, however, for γ-rays to be created spatially displaced from the actual DM activity. This can occur through two different processes: inverse Compton (IC) scattering or synchrotron radiation. In IC scattering, relativistic leptons are produced in DM annihilation and begin moving out of the cluster. Also present are infrared and visible photons emitted by stars in the cluster. These will act as seed photons for IC scattering. IC scattering can proceed when a photon of energy E_γ impinges on a relativistic electron of total energy $E_e = \Gamma m_e c^2$. A quantum mechanical phenomenon permits the electron to transfer energy to the photon if they fall within the differential cross-section given by the Klein-Nishina formula:

$$\frac{d\sigma}{d\Omega} = \frac{r_0^2}{2}\frac{1+\cos^2\theta}{(1+\Gamma(1-\cos^2\theta))^2}\left[1+\frac{\Gamma^2(1-\cos^2\theta)}{(1+\cos^2\theta)(1+\Gamma(1-\cos\theta))}\right] \quad (1.5)$$

where $r_0$is the classical electron radius ($e^2/m_e c^2$) and Γ is the Lorentz factor of the electron. As long as $E_\gamma E_e \sim (m_e c^2)^2$, the photon's energy gets boosted by a factor of Γ^2. In practice, the photon's energy will be boosted from ~eV to GeV–TeV. The power emitted due to the IC radiation is:

$$P_{IC} = \frac{4}{3}\sigma_T c U_{rad}(\Gamma^2 - 1) \quad (1.6)$$

where σ_T is the Thomson cross-section (6.65×10^{-25} cm^2) and U_{rad} is the energy density of the photon field [75]. Figure 1-12 gives the relevant Feynman diagram for IC scattering.

Charged particles moving in a magnetic field will experience the Lorentz force and will spiral around magnetic field lines. At lower energies the radiation the charged particle emits as it is accelerated is called cyclotron radiation. The energy of the emitted photons is proportional to the gyrofrequency $\omega_{gyro} = |q|B/m$. The Lorentz force is always directed inwards towards the magnetic field line, so the emission pattern follows that of a dipole antenna aligned with the tangential velocity according to the Larmor formula. When the particle increases energy to relativistic speeds, the radiation pattern

dilates in the forward direction due to relativistic coordinate transform. It then becomes known as synchrotron emission and radiates energy per unit time:

$$P_{sync} = \frac{2(KE_{rel})e^2\Gamma^4 c}{3r^2} \quad (1.7)$$

where KE_{rel} is the relativistic kinetic energy and r is the gyroradius of the charged particle. The synchrotron emission peaks at $E_{sync} \approx (5 \times 10^{-9})\Gamma^2 B_{\perp} eV$. The highest fields in a cluster are found near the largest galaxies usually concentrated in the center. For TeV-scale WIMPs interacting in the microGauss magnetic field of a large cluster, γ-rays from synchrotron radiation are possible as well [8]. Figure 1-13 shows how the radiation pattern changes between cyclotron and synchrotron emission.

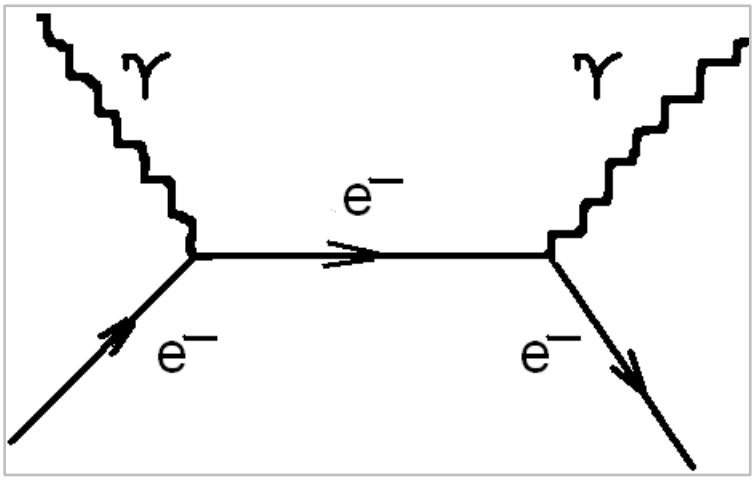

Figure 1-12: The Feynman diagram for inverse Compton scattering

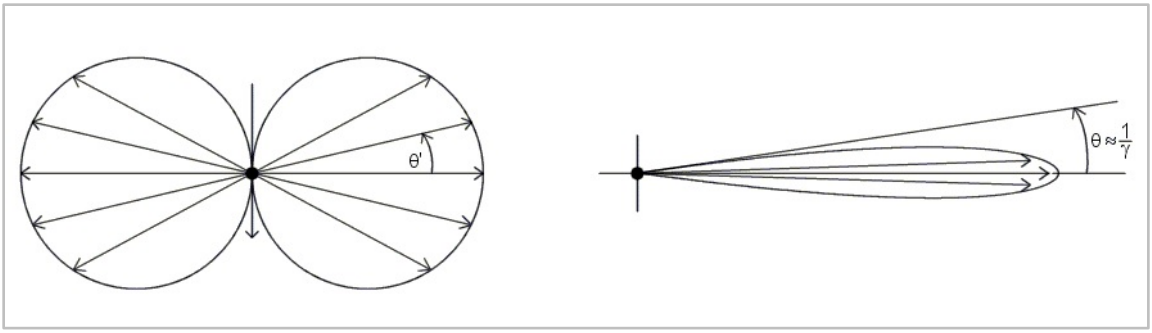

Figure 1-13: Diagram comparing the radiation pattern from non-relativistic and relativistic electrons viewed in the direction of the centripetal acceleration (credit: Patryk Kawecki [76]). The left panel shows the dipole shape of the cyclotron radiation created from a non-relativistic electron. The right panel shows at relativistic speeds the dipole becomes length-contracted into a beam of angle $\theta = 1/\gamma$ (the Lorentz factor).

The integrated γ-ray flux at Earth one would expect from WIMPs of mass $M\chi$ and velocity-weighted annihilation cross-section $\langle\sigma v\rangle$ distributed in a spherical halo takes the form:

$$\Phi_\gamma(\Delta\Omega) = \frac{1}{4\pi}\frac{\langle\sigma v\rangle}{2M_\chi^2}\left(\int_{E_{min}}^{E_{max}} \frac{dN_\gamma}{dE}\,dE\right)J(\Delta\Omega) \quad (1.8)$$

where the energy integral is a particle physics term representing the spectrum of the photons produced via the annihilation channels' branching fractions and $J(\Delta\Omega)$ is the J-factor, an astrophysical term used to define the square of the DM density along the line of sight (l.o.s.) integrated over some solid angle $\Delta\Omega$ corresponding to the size of the cluster. The J-factor is directly proportional to the γ-ray luminosity from DM annihilation quoted in terms of GeV^2cm^{-5} (particle physics) or $M_\odot^2 kpc^{-5}$ (astrophysics). Specifically the J-factor is defined as:

$$J(\Delta\Omega) = \int_{\Delta\Omega}\int_{l.o.s.} \rho^2\big(r(l,\theta)\big)\,dl\,d\Omega \quad (1.9)$$

The radial term is the displacement vector drawn between the Earth – center of the cluster vector ($\vec{d}$) and the Earth – edge of the cluster's halo vector ($\vec{l}$). The two Earth vectors are offset by an angle θ. The magnitude of the displacement vector ($\vec{r}$) can be computed by:

$$|r(l,\theta)| = (d^2 + l^2 - 2dl\cos\theta)^{\frac{1}{2}} \quad (1.10)$$

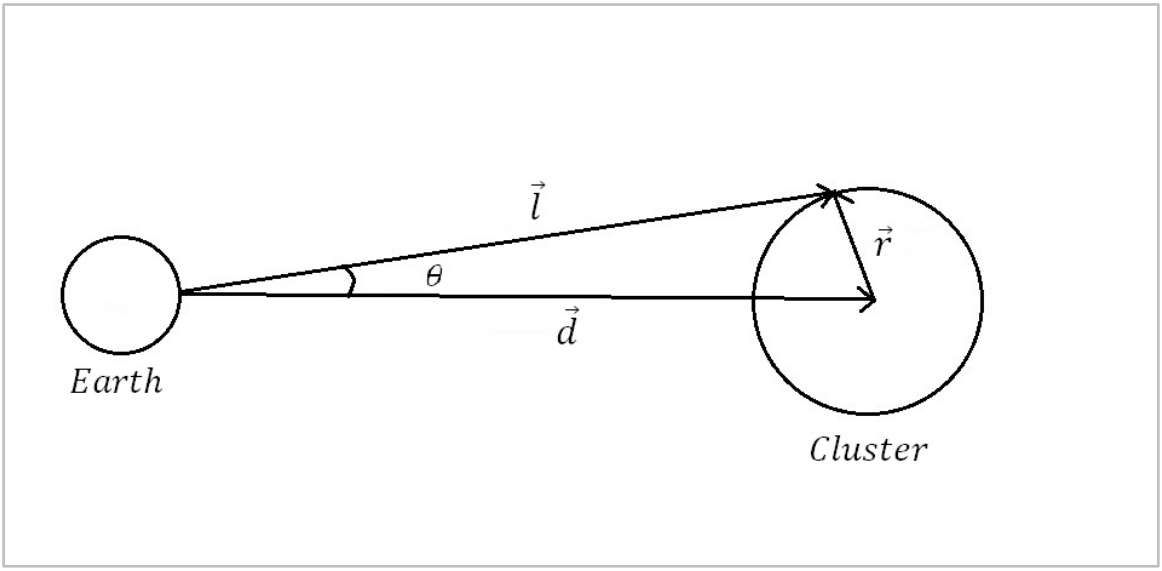

Figure 1-14: Vector representation of the radial term

Given the γ-ray fluxes from DM targets a plot similar to Figure 1-14 can be constructed for various values of $M\chi$ and $<\sigma v>$. As no DM source has yet been detected by any of the current instruments only flux upper limits exist, hence they form the basis for an exclusion plot. Deeper exposures and improved instrument sensitivity will reduce the flux upper limit until a detection can be made that would determine the mass and cross-section of the annihilating WIMP [77] [78].

1.5 Dark Matter Profiles

A number of profiles to model the DM density distribution $\rho(r)$ have been proposed. The most widely used of these are the Einasto profile and the Navarro-Frenk-White (NFW) profile, both named after their respective authors. Jaan Einasto envisioned a DM profile falling off with radius according to a curved power law:

$$\rho(r) = \rho_0 e^{-\left(\frac{r}{r_0}\right)^{\frac{1}{N}}} \quad (1.11)$$

where ρ_0 the core density, r_0 is the core radius, and N is a parameter called the Sersic index that is allowed to vary depending on the degree of curvature desired [79]. For example an exponential cutoff takes $N = 1$ while the de Vaucouleurs surface brightness profile takes $N = 4$ [80]. Julio Navarro, Carlos Frenk, and Simon White constructed their profile in a different manner by matching sophisticated N-body simulations to high-resolution spectroscopic measurements of cluster member velocities:

$$\rho(r) = \frac{\rho_c}{\left(\frac{r}{R_s}\right)\left(1 + \frac{r}{R_s}\right)^2} \quad (1.12)$$

where ρ_c is the critical density of the Universe ($3H^2/8\pi G$) at a given redshift and R_s is the scale radius. The scale radius is proportional to the virial radius or R_{200}, the radius at which the density is 200 times the critical density, by a factor c called the concentration parameter that varies by galaxy cluster [81]. The concentration parameter of each cluster is found empirically by fitting the luminosity profile to the lensing profile based on standard cosmological parameters (see Section 3.4). Using the NFW profile, 90% of the DM annihilation flux originates from the region within the scale radius.

Several key differences between the two models must be considered before choosing one over the other. The NFW profile is categorized as cuspy because its density diverges when r goes to zero. The ability to tune the Sersic index gives the Einasto a smaller RMS spread to the data at inner radii. On the other hand the NFW profile does a

better job at modeling larger radii because it falls off as r^{-3}, less severe than the exponential falloff of the Einasto profile. Several of the galaxy clusters in the VERITAS dataset have diameters on the order of Mpc, translating to over a degree on the sky, so the NFW profile will more accurately model the extent of the clusters. Other DM profiles such as the Burkert, Isothermal, or Generalized-NFW were considered initially, but after some trials the two above were selected for use in the analysis [82] [83].

1.6 Galaxy Clusters

Galaxy clusters are the largest collections of matter in the Universe held together by gravity. (Note: Superclusters are larger structures but are not gravitationally bound. Over time the Hubble flow will separate all the clusters in a supercluster.) They consist of hundreds to thousands of galaxies orbiting a common center with a combined mass in the $10^{13} – 10^{15}$ $M_{\odot}$ mass range. As such, clusters also contain the highest concentrations of DM known anywhere, making them attractive targets for indirect DM detection. In between the galaxies in a cluster are large regions of hot, low-density plasma of the ICM. The characteristics of a cluster (i.e., velocity dispersion, scaling relation, plasma temperature) vary greatly if the cluster has just undergone a merger. Once the cluster has virialized however, the data fits the theoretical models as a function of cluster mass with little spread [84].

There are a number of factors that impact the prospect of indirect DM detection in galaxy clusters. For one, the clusters VERITAS observed are several hundred Mpc distant. This affects the value of the J-factor that varies as distance^{-5}. Additionally the region of space surrounding a cluster rarely is free of other γ-ray sources. Several clusters in this archival search were not the targets of the array pointing, but rather appeared serendipitously in the field of view. Galactic γ-ray sources such as pulsar wind nebulae (PWNe) and supernova remnants (SNRs) will also contribute to a γ-ray signal. In some clusters the luminous cores of a class of galaxies called active galactic nuclei (AGNs) are

known γ-ray emitters that would contaminate the DM annihilation signal, so therefore they must be excluded. The true gravitational profile of clusters derived from weak lensing maps shows irregularities from a perfect spherical halo, making modeling somewhat more involved. To smooth out these perturbations and allow enough room within the field of view (FOV) for background estimation, clusters will be defined by their R_{500} angular extent (~1.6 times smaller than R_{200}). The DM profile within R_{500} is more spherically symmetric than the outer edge of the weak lensing contours [85].

Taken as a whole, the J-factors of this search's galaxy clusters are comparable to that of dSphs or the GC. Given in terms of dimensionless $\log_{10}[J/(\mathrm{GeV}^2\mathrm{cm}^{-5})]$, clusters fall in the range of 15 – 18, dSphs occupy the 16 – 19 space, and the GC is estimated to be 21. Even though dSphs contain many orders of magnitude less mass than clusters do, their distances are measured in kpc not Mpc. The GC is a unique source for DM annihilation due to its close proximity and accurately-modeled mass distribution. The Keplerian motion of stars and gas clouds that orbit the central supermassive black hole (SMBH) called Sgr A* allow for close estimates of its size, some $4.1 \pm 0.6 \times 10^6 M_{\odot}$ [86]. HESS finds a γ-ray source (HESS J1745-290) within its error circle at the location of Sgr A* but cannot claim for a fact that it is Sgr A* doing the emitting [87]. The γ-ray spectrum Fermi-LAT sees from the GC suggests that DM annihilation is a likely explanation [88]. A population of unresolved γ-ray emitters like PWNe or MSPs cannot reproduce the hard Fermi-LAT spectrum below 1 GeV. Any search for a DM γ-ray signal from the GC requires careful source/background region selection to account for the presence of a diffuse γ-ray background [89].

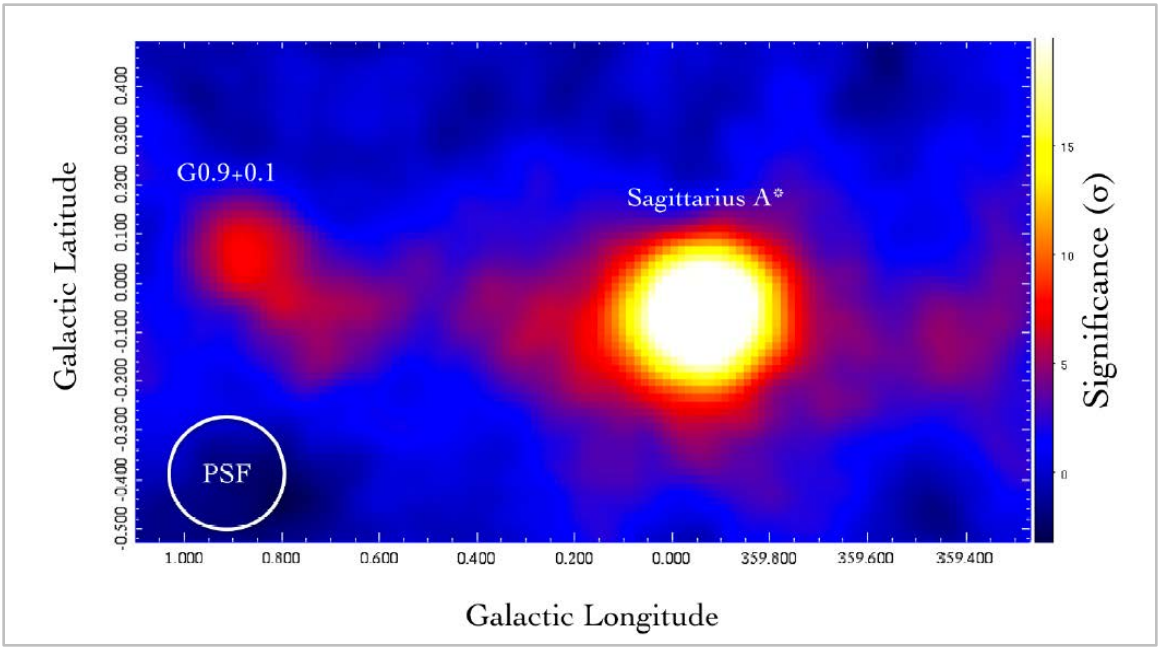

Figure 1-15: VERITAS skymap of the GC region above 2 TeV (credit: Andy Smith [90]). Significant emission can be seen from Sgr A*, G0.9+0.1 (a SNR), and diffuse emission from the 'bridge' between the two sources.

1.7 Galaxy Cluster Surveys

Two surveys of galaxy clusters at low redshift ($z < 0.1$) were cross-referenced against the VERITAS dataset to identify any overlaps. The surveys gave positional data (redshift and sky coordinates) as well as angular size (R_{500}). The first of these is the HIghest X-ray FLUx Galaxy Cluster Sample (HIFLUGCS) by Thomas Reiprich and Hans Böhringer [91]. They analyzed data from the ROSAT All-Sky Survey [92] and selected the 63 clusters away from the plane of our galaxy with the greatest X-ray flux. Measurements of the plasma temperature and density allowed the authors to estimate the total X-ray luminosity of a cluster and derive the gravitational mass as well.

We also used the Joo Yoon et al. survey, which identified nearby clusters (also $z < 0.1$) from the Sloan Digital Sky Survey (SDSS) Data Release 5 archive [93]. By

narrowing down the over 215 million objects in the survey according to their optical photometric and spectroscopic properties, the authors were able to identify 924 galaxy clusters. The coordinates of the cluster centers from both surveys were checked with a tool called VListBuilder [94] to determine if any VERITAS observations included the cluster in the field of view (FOV). From this and the selection cuts mentioned in Section 3.3, 12 galaxy clusters were selected for further analysis.

The selected galaxy clusters were then checked against Digital Sky Survey 2 (DSS2) flexible image transport system (FITS) images with the aid of the visualization software ds9 to ensure that no bright stars would overlap and interfere with the cluster measurements [95] [96]. Each skymap (except for the Perseus cluster) measures $5° \times 5°$. The two green ‘X’s mark the VERITAS observation target and the center of the cluster. The green crosses show the tracking positions and the red ring represents the corresponding array FOV. The dotted and solid black rings represent each cluster’s R_{200} and R_{500} respectively. Stars from the SAO J2000 star catalog with B-band magnitude < 8.0 were circled to simulate the regions that the γ-ray analysis software would exclude from the background. Fortunately no bright stars were found to coincide with the target cluster positions. The skymaps are presented in the following 12 figures.

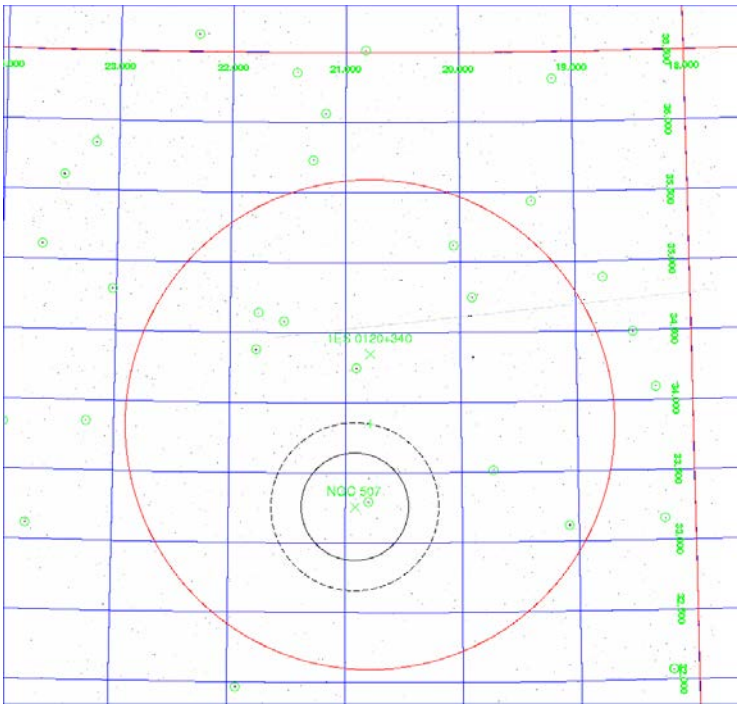

Figure 1-16: Target: 1ES 0120+340, Cluster: NGC 507. Green 'X's: VERITAS target and cluster. Green crosses: tracking positions wobbled around the target. Red rings: array FOV from the tracking positions. Black rings: the cluster's R_{200} (dashed) and R_{500} (solid). Small circles: stars in the field

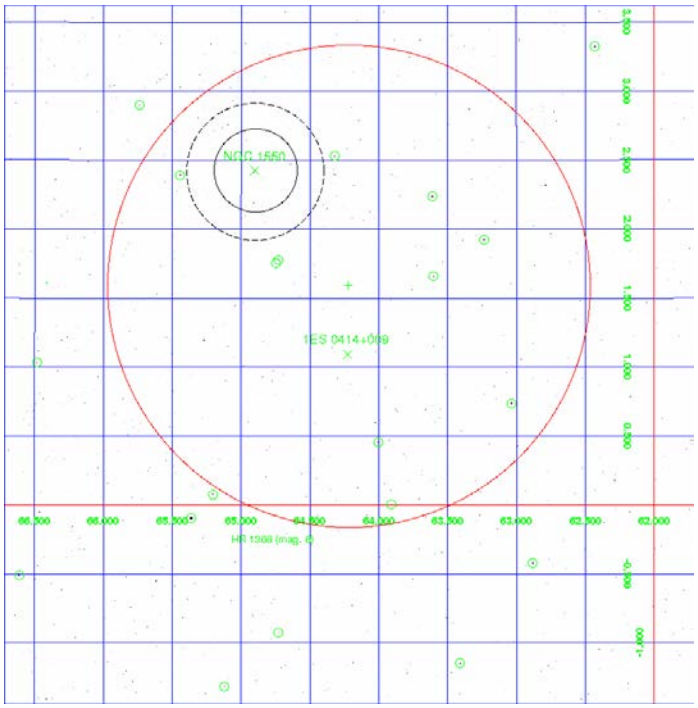

Figure 1-17: Target: 1ES 0414+009, Cluster: NGC 1550 (same as Figure 1-16)

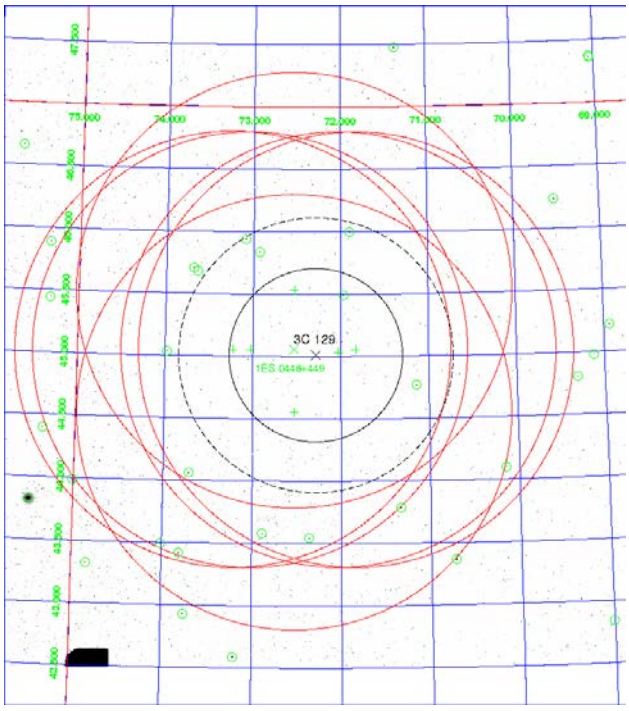

Figure 1-18: Target: 1ES 0446+449, Cluster: 3C 129 (same as Figure 1-16)

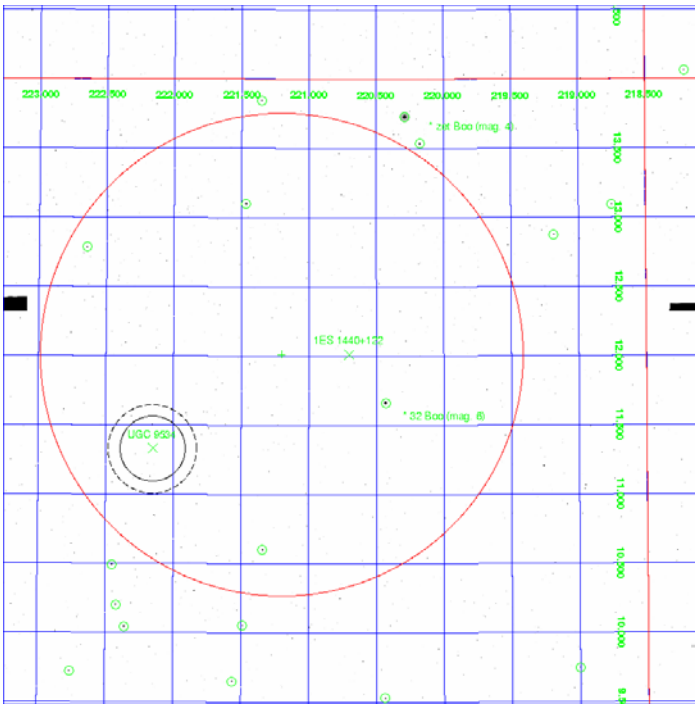

Figure 1-19: Target: 1ES 1440+122, Cluster: UGC 9534 (same as Figure 1-16)

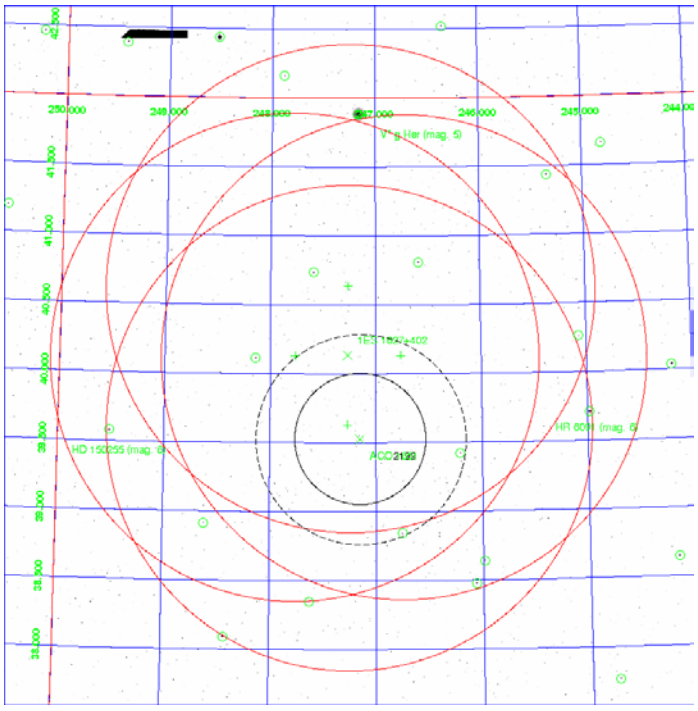

Figure 1-20: Target: 1ES 1627+402, Cluster: A2199 (same as Figure 1-16)

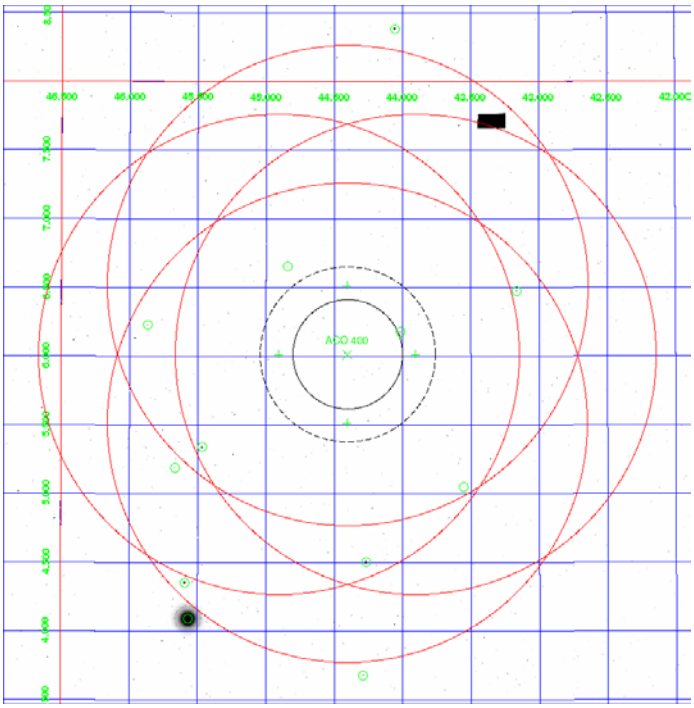

Figure 1-21: Target and Cluster: A400 (same as Figure 1-16)

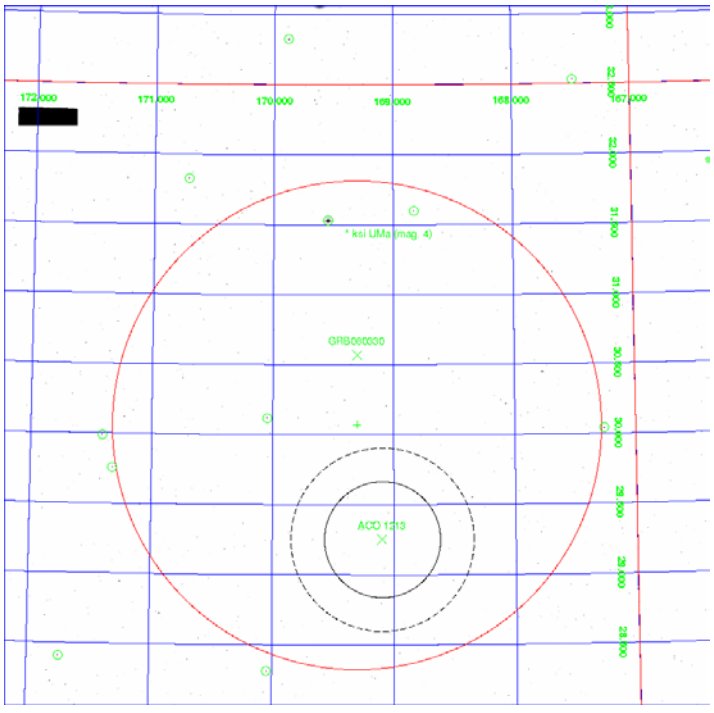

Figure 1-22: Target: GRB 080330, Cluster: A1213 (same as Figure 1-16)

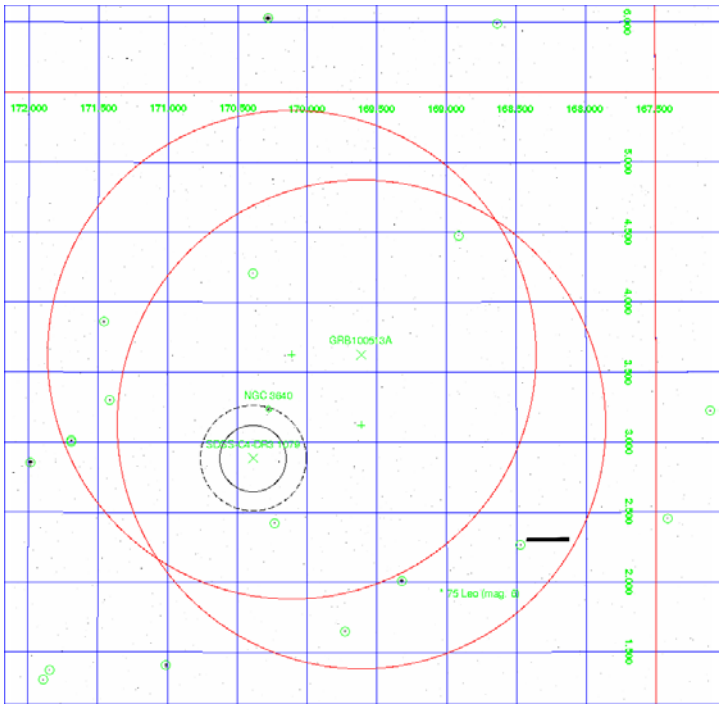

Figure 1-23: Target: GRB 100513A, Cluster: SDSS-C4-DR3 1079 (same as Figure 1-16)

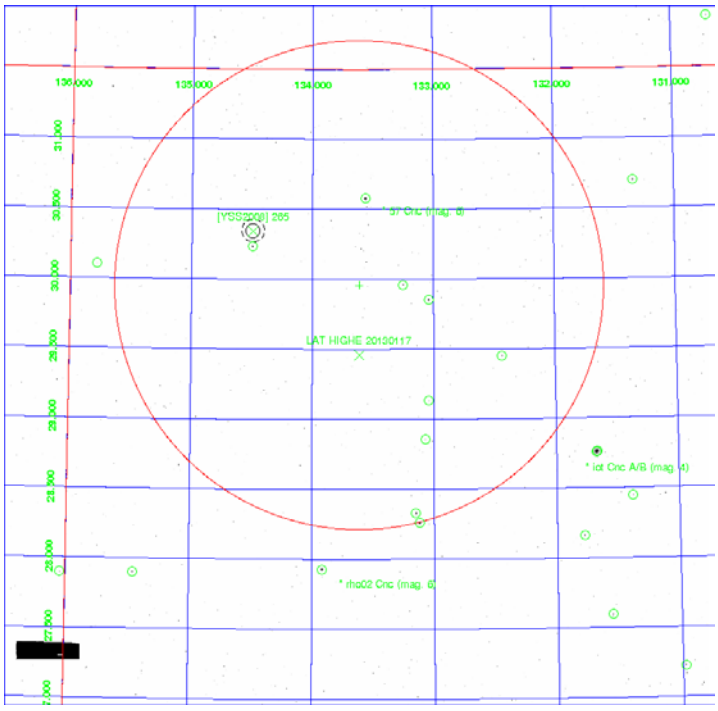

Figure 1-24: Target: LAT HIGHE 20130117, Cluster: [YSS 2008] 265 (same as Figure 1-16)

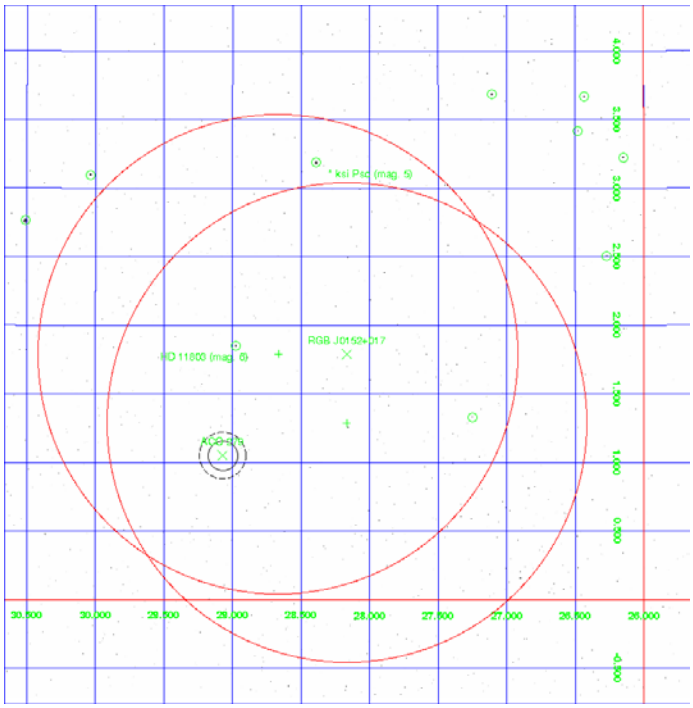

Figure 1-25: Target: RGB J0152+017, Cluster: A279 (same as Figure 1-16)

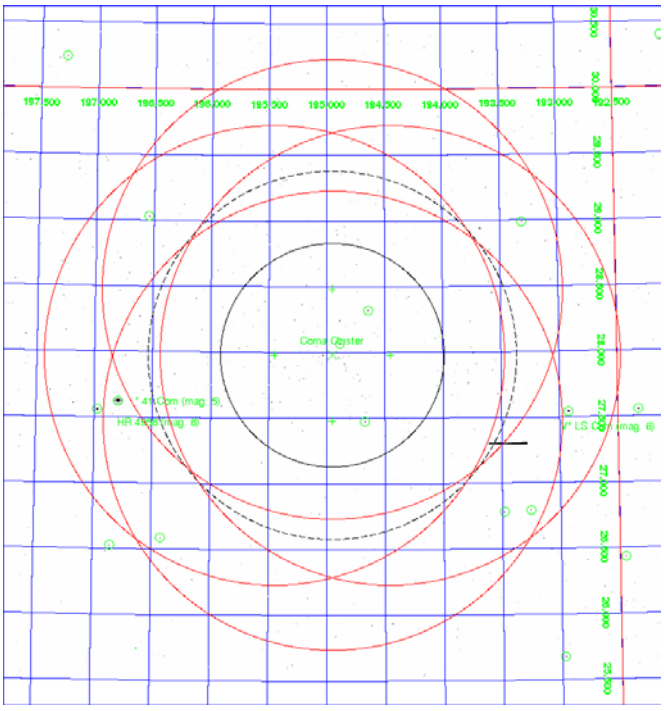

Figure 1-26: Target and Cluster: Coma cluster (same as Figure 1-16)

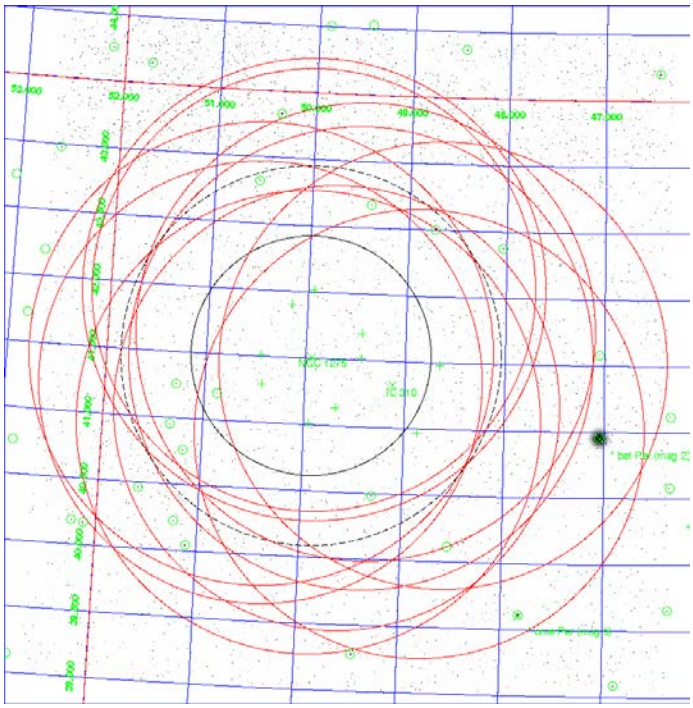

Figure 1-27: Target and Cluster: Perseus cluster (same as Figure 1-16, see Figure B-1)

Taken together, γ-ray observatories have the capability to see signatures of DM annihilation, and galaxy clusters are prime targets to witness such interactions. But how exactly does the latest generation of ground-based Cherenkov telescope arrays such as VERITAS see γ-ray photons, especially considering the Earth's atmosphere completely attenuates them before reaching the ground? This phenomenon will be explored in the next chapter while also delving into the hardware and analysis software of VERITAS.

CHAPTER 2. ATMOSPHERIC CHERENKOV TECHNIQUE AND VERITAS

2.1 Cherenkov Radiation

Cherenkov radiation is produced when an energetic charged particle moves through a dielectric medium at a velocity higher than the speed of light in that medium. The electric field of the particle polarizes the adjacent molecules of the medium. Once the particle passes, the molecules return to their original dipole configuration by releasing a brief pulse of continuum electromagnetic radiation peaked in UV and blue wavelengths. This radiation is named after the Russian scientist Pavel Cherenkov, who was the first to study it in detail [97].

The radiation fans out in the shape of a cone along the direction of the particle's path. As Figure 2-1 demonstrates, the emission of the molecules in the wake of the particle interferes constructively via the Huygens–Fresnel principle. The opening angle of this cone for a medium with refractive index *n* is given by:

$$\cos\theta_C = \frac{(\frac{c}{n})t}{v_s t} = \frac{c}{n v_s} \quad (2.1)$$

where θ_C is called the Cherenkov angle, v_s is the speed of the particle, and c is the speed of light measured in a vacuum. Alternatively when a particle moves at speeds less than the speed of light for the medium, no coherent emission is detected because the particle never leads the surface of the Mach cone.

The angular relationship above imposes a cutoff velocity below which no Cherenkov radiation is generated. The minimum Cherenkov angle $\theta_C = 0$ is reached when

$v_s = c/n$. The threshold relativistic energy E_{th} of such a particle with rest mass M_0 and Lorentz factor Γ is defined by:

$$\Gamma = \frac{1}{\sqrt{1 - \frac{v_s^2}{c^2}}}\ ,\ E_{th} = \Gamma M_0 c^2 = \frac{M_0 c^2}{\sqrt{1 - \frac{1}{n^2}}} \quad (2.2)$$

Computing the threshold energy of an electron or positron (having rest mass of 511 keV) created by a γ-ray passing through the atmosphere (refractive index of 1.00029 at sea level) yields 21 MeV. Similarly for a cosmic-ray proton of rest mass 938 MeV, the threshold energy for Cherenkov radiation is 39 GeV. Taking the highest energy limit as $v_s \rightarrow c$, equation 2-1 becomes:

$$\theta_{C,max} = \cos^{-1}\frac{1}{n} \quad (2.3)$$

In the lower atmosphere this corresponds to a maximum Cherenkov angle of ~1.4°. The refractive index drops with vertical height, so in the region where VHE γ-ray showers develop to their maximum size (8 – 10 kilometers above the ground) the opening angle of the cone is closer to 0.8° [98].

The change in refractive index *n* as a function of altitude means that the light pool at ground level takes the shape of a flattened disk or pancake. In Figure 2-2 there is a bump at ~125 meters where the wavefronts' edges pile up. For higher energy γ-rays, the photon density (brightness) rises but the spatial distribution remains generally unchanged.

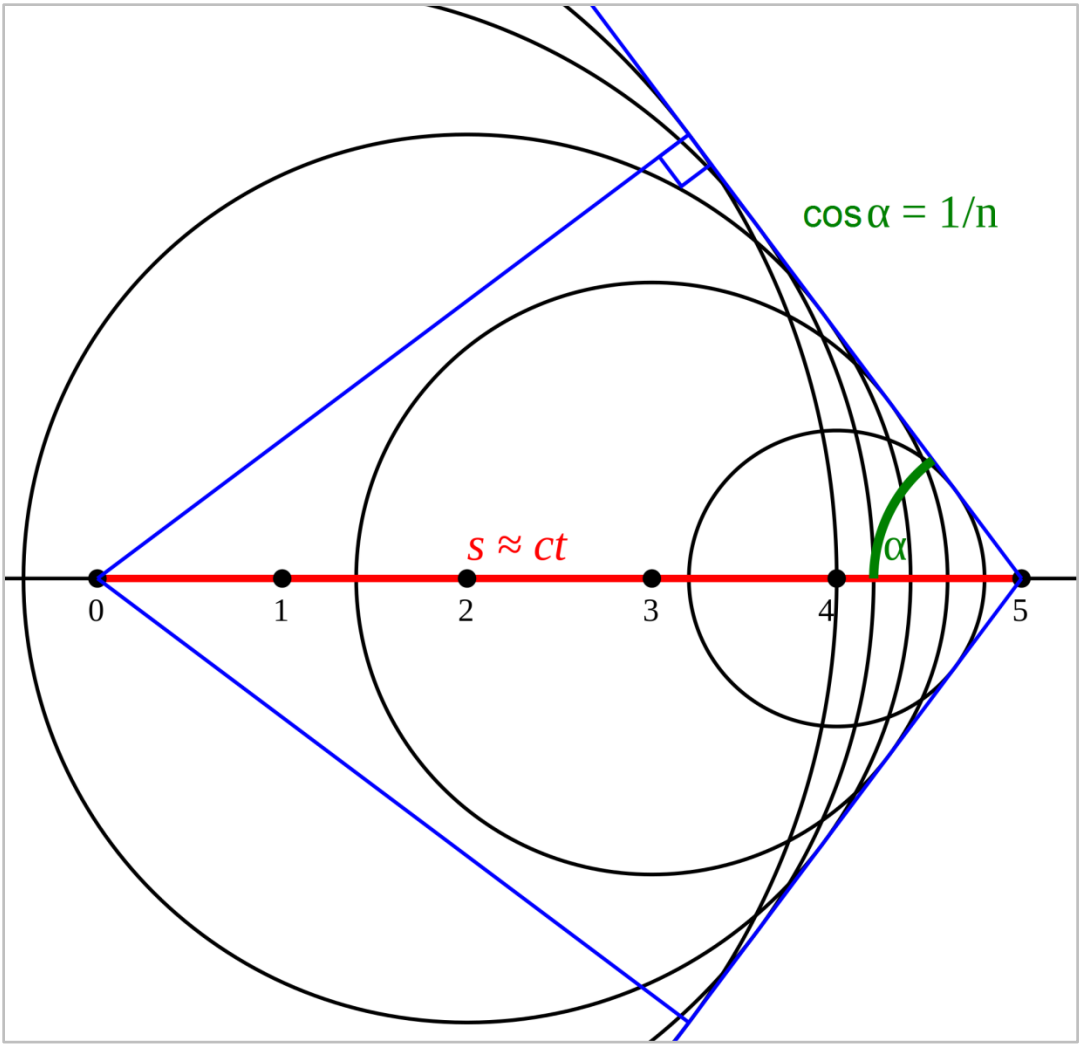

Figure 2-1: Cherenkov wavefronts combining constructively via the Huygens–Fresnel principle. The particle moves from position 0 through 5 at $v_s \sim c$. Spherical pulses of Cherenkov radiation move outward from each location at the speed of light. The angle α is the Cherenkov angle for the wavefronts and also the (inverted) cone of light that propagates outward.

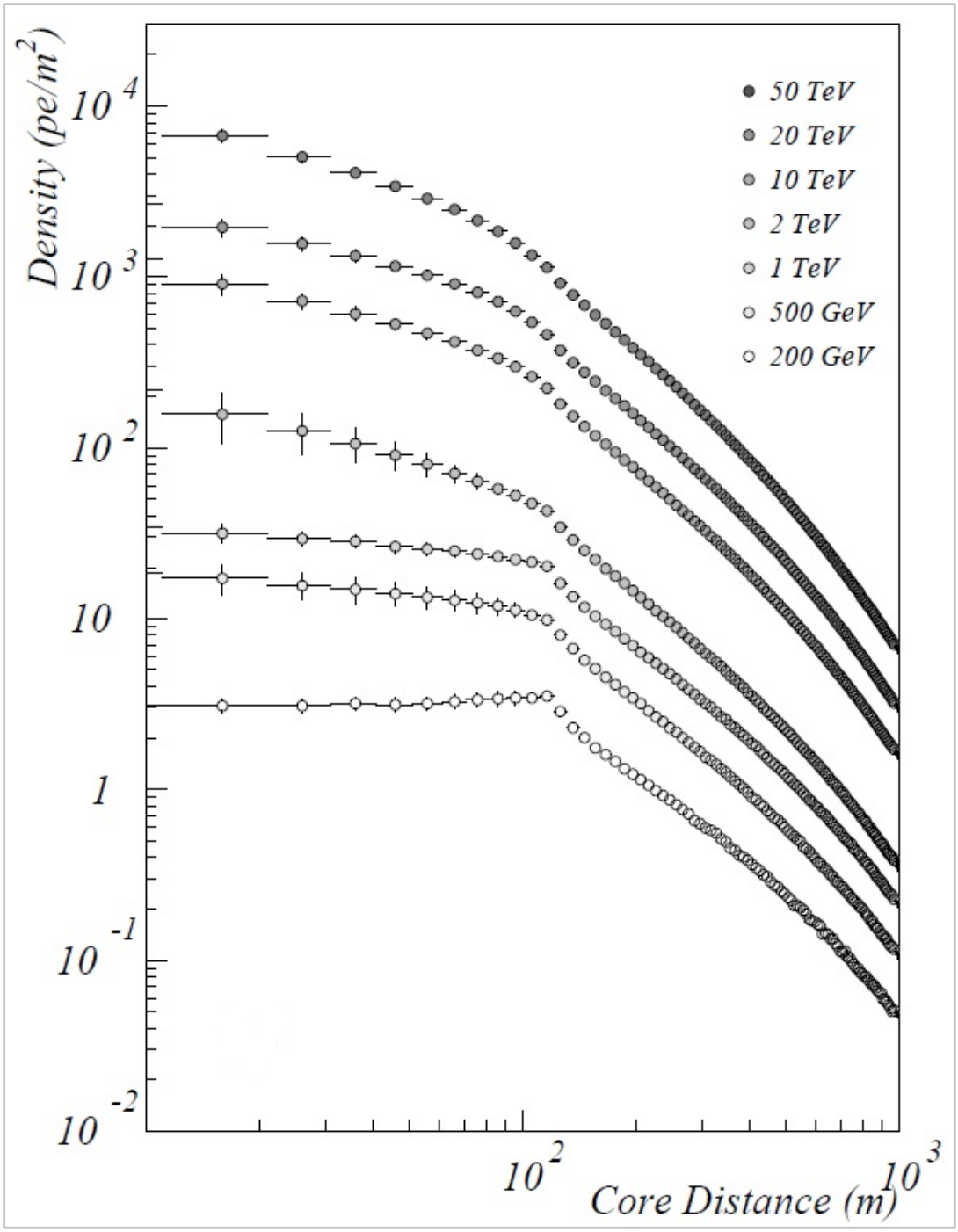

Figure 2-2: Simulated average Cherenkov lateral distribution for showers initiated by γ-rays of various energies (credit: I. de La Calle Pérez [99])

2.2 Extensive Air Shower (EAS) from γ-Rays and Cosmic-Rays

When a γ-ray above 1.022 MeV ($2M_ec^2$) interacts with a nucleus of an oxygen or nitrogen atom in the upper atmosphere, it spontaneously produces electron-positron pairs. Momentum conservation dictates that these particles will travel close to the incident direction of the γ-ray at nearly the speed of light, thereby producing Cherenkov radiation in their wake above the threshold energy. These charged particles are free to interact with other nuclei and lose energy through a free/free process known as Bremsstrahlung while spawning additional γ-rays. Bremsstrahlung translates from German as 'braking radiation.' This occurs because the electron-positron pairs are accelerated by an external electric field. The electron or positron must possess energy greater than 83 MeV to emit Bremsstrahlung in air. The shower of particles and γ-rays continues to multiply until about 8 – 10 kilometers above the ground where radiative losses cap further growth. Bremsstrahlung governs the propagation of an EAS through the atmosphere. Although the EAS is usually reabsorbed by the atmosphere long before it makes it to ground-level, the cone of Cherenkov radiation continues relatively unimpeded to Earth [100].

γ-rays are not the only source of particle showers in the atmosphere. Figure 2-3 shows the spectrum of cosmic-rays that pass through the atmosphere. The spectrum generally follows that of a power law $dN/d\Gamma \propto \Gamma^{-p}$ where Γ is the Lorentz factor of the particles and p is close to 3. There are a number of regimes on the graph demarcated by the 'knee' and 'ankle' with their respective particle populations. The deflection from the magnetic fields of the Earth and Sun contribute to the flatting of the spectrum below 2 GeV. Between 2 GeV and the 'knee' at 4 PeV the spectrum has index $p \sim 2.8$ and is composed predominantly of particles accelerated within the Milky Way by PWNe, X-ray binaries, or possibly the SMBH Sgr A* [101]. Between the 'knee' at 4 PeV and the 'ankle' at 500 PeV the index softens to $p \sim 3.3$. This region is composed of an admixture of galactic- and extragalactic-accelerated particles [102]. Beyond the 'ankle' at 500 PeV the spectrum re-hardens to $p \sim 2.7$ by the time the particle energy reaches 4 EeV. In this regime there are no particles of galactic origin because the Milky Way's magnetic field is

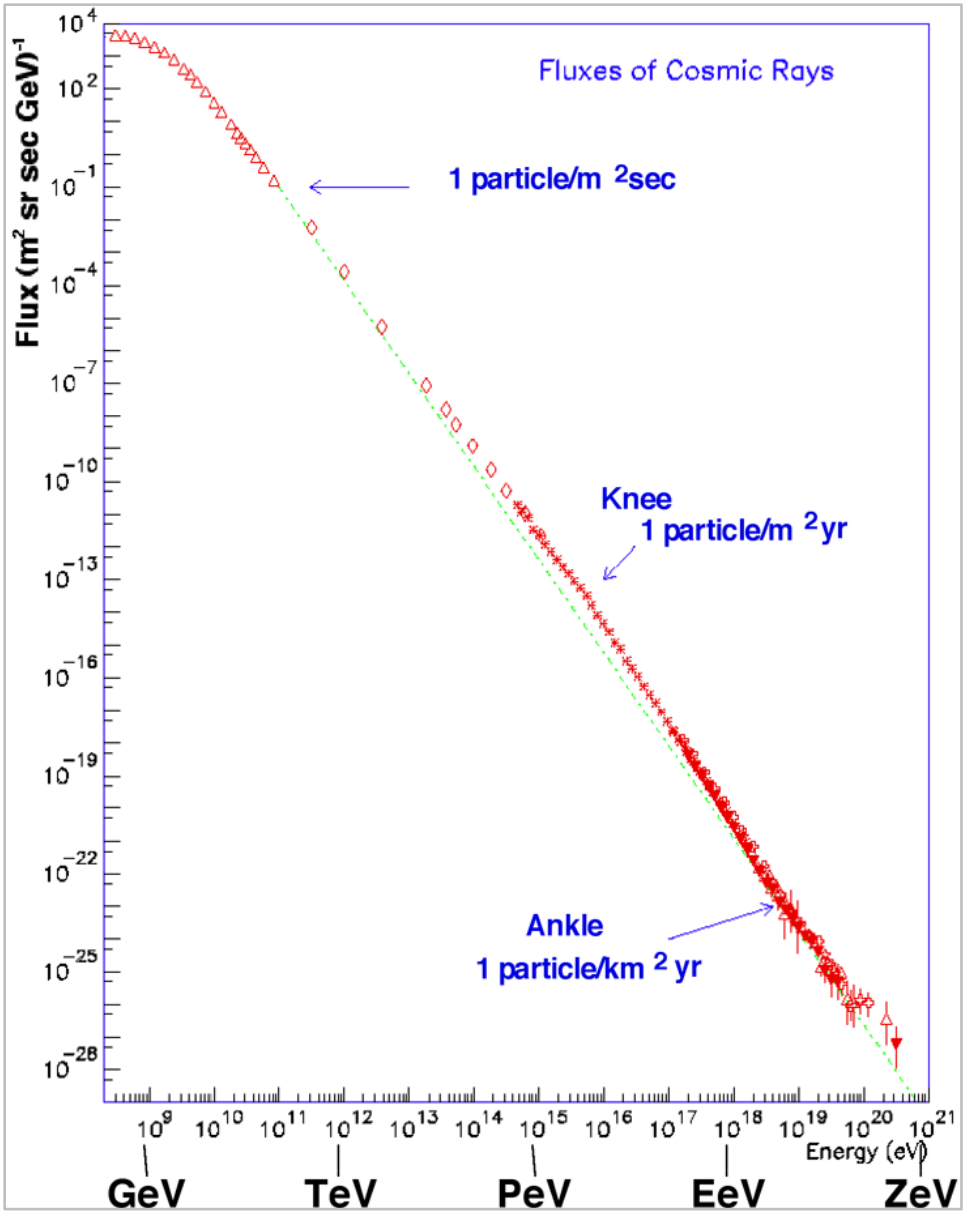

Figure 2-3: Spectrum of cosmic-rays at Earth's surface (credit: JEM-EUSO [103], data compiled by Simon Swordy [104])

insufficient to contain them. This means their gyroradii (see Section 1.4) is larger than the radius of the galaxy [105]. There also exists an anomaly at extreme energies, the UltraHigh Energy Cosmic-Rays (UHECRs). Cosmic-rays should not be detected beyond the upper limit energy called the Greisen–Zatsepin–Kuzmin limit (5×10^{19} eV). UHECRs above this cutoff readily interact with cosmic microwave background photons

and spontaneously lose energy. A small number of UHECRs however have been detected with energies as high as 3×10^{20} eV, prompting theorists to rework their understanding of the Universe at its highest energies [103].

The propagation of a cosmic-ray proton through the atmosphere will produce a more complex EAS due to the variety of interactions possible (listed with decay times):

$$\pi^0 \rightarrow \gamma + \gamma \ \ (8.3 \times 10^{-17} sec) \quad (2.4)$$

$$\pi^+ \rightarrow \mu^+ + \nu_\mu \ \ (2.6 \times 10^{-8}\, sec), \qquad \mu^+ \rightarrow e^+ + \overline{\nu_\mu} + \nu_e \ \ (2.2 \times 10^{-6}\, sec) \quad (2.5)$$

$$\pi^- \rightarrow \mu^- + \overline{\nu_\mu} \ \ (2.6 \times 10^{-8}\, sec), \qquad \mu^- \rightarrow e^- + \overline{\nu_e} + \nu_\mu \ \ (2.2 \times 10^{-6}\, sec) \quad (2.6)$$

Successive strong interactions between quarks of the cosmic-ray and of the nucleus of an oxygen or nitrogen atom will produce a smeared-out particle continuum through a process called hadron fragmentation. Pions account for nearly 90% of the daughter particles from cosmic-rays. π^0's, π^+'s, and π^-'s are produced in relatively equal proportions. The shower from a π^0 is practically indistinguishable from a γ-ray shower, the only difference being the height of the first interaction. The charged pions decay to muons that leave a distinctive ring in the camera plane images. Muons reach the ground due to their longer lifetime, coupled with relativistic time dilation effects [106]. They are produced lower in the atmosphere than the γ-ray maximum and only emit Cherenkov radiation at $\theta_{C,max}$. This happens because the EAS of the hadron loses energy as it progresses until it reaches the point where the pions decay, where they then produce muons which decouple from the shower cascade. Afterwards the muons propagate to Earth with very little energy loss or deflection [107]. The pion carries greater transverse momentum than an electron-positron pair so the EAS from a cosmic-ray will cover more area on the sky compared to a γ-ray when viewed from the ground. . For the proton EAS many electromagnetic subshowers are possible, hence the photon distribution at ground level is more spatially extended (see Figure 2-5). Additionally γ-ray showers give rise to brighter light pools because not all of the particles produced in a cosmic-ray shower interact electromagnetically (i.e., neutrinos).

2.3 Imaging Atmospheric Cherenkov Telescope (IACT) Design

The method for imaging the Cherenkov radiation in the atmosphere incorporates a large optical reflecting dish comprised of tessellated mirror facets focused onto a multipixel camera box. The pixels contain photomultiplier tubes (PMTs) that can register single photons with a time resolution comparable to a Cherenkov flash (a few nanoseconds). The PMTs and their associated back-end electronics record images of the air shower as it progresses in real time as signal above the ambient night-sky background. When the radiation reaches the ground its intensity is quite faint, only ~100 photons/m^2 originating from a 1 TeV γ-ray, so multiple IACTs are often evenly distributed around a site to maximize the effective area of the array [108]. Figure 2-4 shows such an array configuration.

The raw PMT data the array records is a combination of the light from night-sky background, hadronic showers, and γ-ray showers. Various cleaning methods at both the hardware and software level have been developed to recover only the γ-ray signal. The pulse of Cherenkov radiation from a γ-ray will illuminate the array for only a short duration and the time delay from the signal cable of each telescope is known to high precision. Multiple telescopes in the array must trigger within the correct time window for an event to be counted. This effectively removes the random fluctuations of the night-sky background as well as muon showers stemming from hadronic interactions. Muons tend to be produced lower in the atmosphere hence their smaller-size Cherenkov lightpool rarely illuminates more than one telescope.

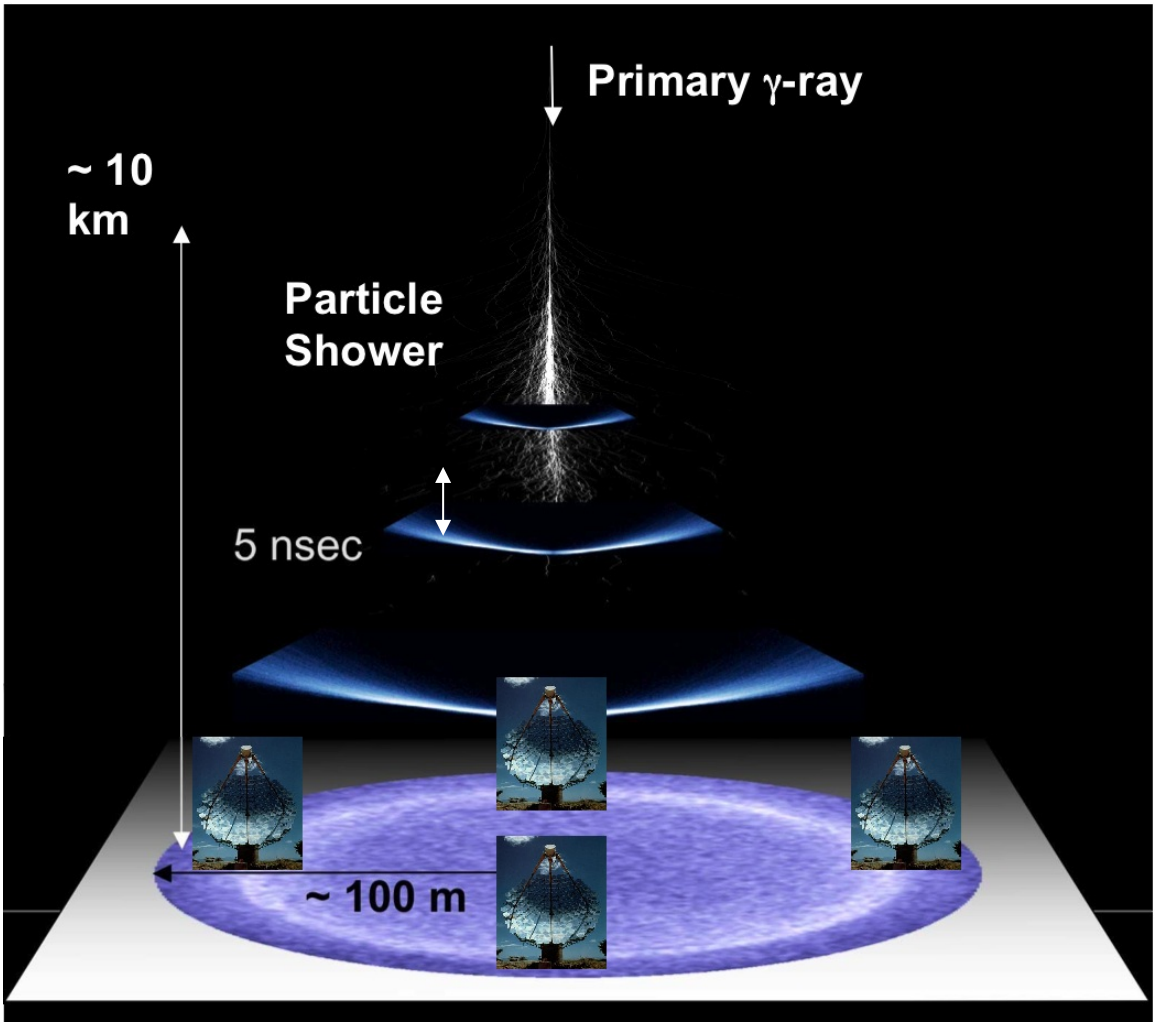

Figure 2-4: IACT array layout to enhance light collection. The telescopes are situated to take advantage of the intrinsic bump in the photon density at the maximum Cherenkov angle for a shower originating directly overhead. They are also spaced far enough apart that a muon emitted lower in the atmosphere from a hadronic shower cannot illuminate multiple telescopes.

To differentiate between hadronic showers and γ-ray showers, the images in the focal plane must be compared. The observed cosmic-ray flux from the Solar wind and extrasolar sources outnumbers the strongest known γ-ray emitter by roughly 2,000 to 1 for current IACTs. Cosmic-rays are distributed isotropically on the sky, whereas γ-rays will emanate from the source position. Cosmic-rays, having net charge, are deflected by magnetic fields at every distance scale (Terrestrial, Solar, Galactic, Intergalactic) along their trajectories, hence their source cannot be localized well. The projection of the shower track onto the ground rarely strikes an IACT directly so the image of a shower at the camera face gets stretched out into the shape of an ellipse. By analyzing the shape of these oblique images subtle differences become apparent between the two shower types. Hadronic showers penetrate deeper into the atmosphere and possess greater transverse momentum, therefore the major and minor axes of their image ellipses tend to be more elongated. γ-ray ellipses on the other hand are tighter and more symmetric from camera to camera. See Figure 2-5 to compare the shower tracks through the atmosphere and camera images of γ-ray showers and hadronic showers. Michael Hillas devised a way of parameterizing the particular moments of an image to perform γ-hadron separation [109]. Stereoscopic event localization and energy reconstruction will be discussed in Section 2.6.3 .

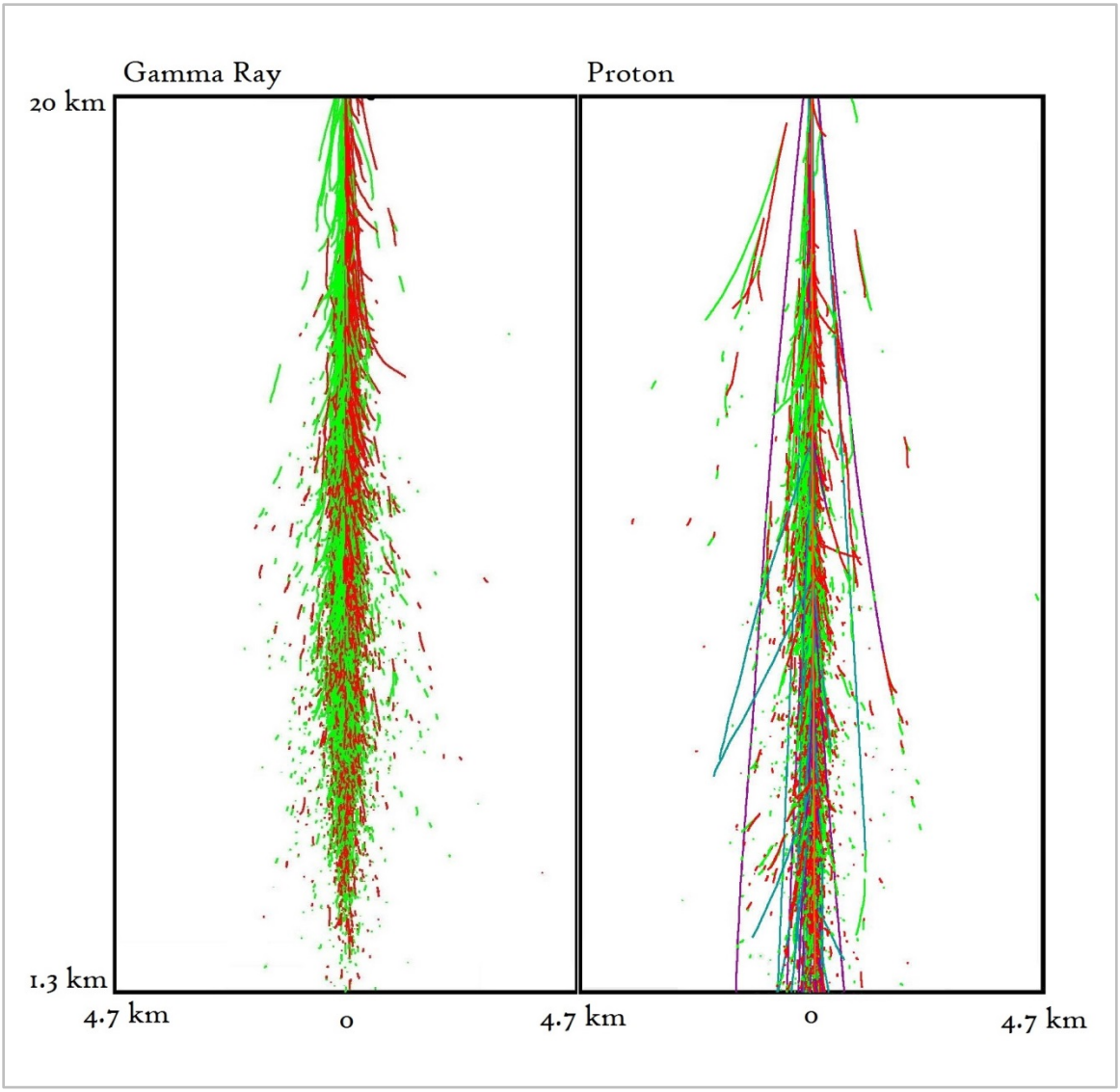

Figure 2-5: γ-ray and proton EASs simulated with KASCADE (credit: Mary Kertzman via private communication). Both primaries begin with 1 TeV energy and each colored line indicates the track of a secondary charged particle propagating through the atmosphere. Green lines represent positrons, red lines represent electrons, and purple lines represent muons. The apparent bifurcation of positrons and electrons is due to the Lorentz force in the Earth's magnetic field. Note the larger lateral dispersion and lower central particle density of the proton compared to the γ-ray.

2.4 VERITAS Observatory

The Very Energetic Radiation Imaging Telescope Array System (VERITAS) is an array of four 12-meter diameter IACTs located at the Fred Lawrence Whipple Observatory in Amado, AZ (31.68° N, 110.95° W, 1,250 meters above sea level) [110]. The array has been fully operational since the spring of 2007. The IACTs are laid out in a skew quadrilateral grid with the lengths of the sides measuring 80, 110, 90, and 130 meters. Telescope 1 (T1) used to be located at a different pad on the site but was moved near the front gate in the summer 2009 to increase the array sensitivity. Figure 2-6 shows the current layout of the site.

All four telescopes incorporate the Davies-Cotton design in their tubular steel Optical Support Structure (OSS) fabricated in Arizona [111]. This design minimizes off-axis aberrations, thereby preserving image quality from showers arriving off the optic axis. However, a consequence of this design manifests itself in a small added time dispersion of the reflected Cherenkov pulse. The servomotors and drive train gear reduction permit the telescopes to slew at up to 1°/sec. The reflector surface is comprised of 345 hexagonal mirror facets, each 0.32 m^2 in area, forming a dish ~110 m^2 in total. These mirrors are spherically shaped with a radius of curvature $R = 24.0 \pm 0.2$ meters, giving the surface an f-number of $f/1.0$. The optical term ‘f-number’ refers to the reflector’s focal length divided by its diameter. In addition, lower f-numbers reduce the extra time dispersion [112]. The mirrors are optimized to reflect the most at the wavelengths of Cherenkov radiation, achieving > 90% reflectivity at 320 nm. The desert dust and temperature variations degrade the mirror performance over time (~3% per year), so the facets are washed monthly and re-anodized every few years [113].

The mirrors are attached to the OSS by means of a triangular mounting bracket and adjustment screws. Each mirror must be properly aligned to focus the light from a point source to create a compact spot on the camera face, called the point spread function (PSF). The size of the PSF also changes with elevation angle, making a hysteresis curve

depending on the flex of the OSS. For calibration purposes, a specialty CCD camera designed at McGill University takes multiple images of a bright star as it raster scans across the face of each mirror. Sophisticated software then processes these images to compute the correction needed for each facet. The final step is bringing the mirrors into alignment by manually adjusting the three screws [114].

Figure 2-6: View of VERITAS from the air (credit: Nicola Galante and Ken Gibbs [115]). The baselines were added by J. Tucci.

The camera box, a 1.8 × 1.8 meter enclosure, is secured in the focal plane by the 12 meter quad-arms of the OSS. Inside, a custom-drilled aluminum faceplate anchors 499 PMTs arranged in a hexagonal lattice forming a circle with an angular spacing of 0.15°. This arrangement of pixels gives the camera a FOV of 3.5°. Figure 2-7 shows the arrangement. When VERITAS was commissioned the cameras were fitted with Photonis XP2970/02 PMTs that performed with a peak quantum efficiency (QE) of ~20%. During the summer of 2012 all pixels were upgraded to super-bialkalai Hamamatsu R10560-100-

20 MOD PMTs having QE > 30%. The boost in sensitivity of the upgraded tubes enables the array to detect fainter, low-energy showers than previously was possible. This led to a reduction in the threshold energy of 30% while increasing the effective area of the array by 25% [116]. Figure 2-8 is an example of an upgraded PMT QE curve. High voltage calibration was completed by 1) the manufacturer 2) the Purdue PMT testing lab and 3) on-site to ensure that all PMTs register the same gain: 200,000. The voltages required, typically ~1,000 V, are tuned until the whole camera is flat-fielded. At this gain a PMT outputs current < 10 μA due to the ambient background light on a clear, moonless night. A block of silvered plastic Winston light cones is fitted in front of the pixels to increase collection efficiency. The cones serve to fill in the gap between pixels and funnel off-axis light towards the PMTs.

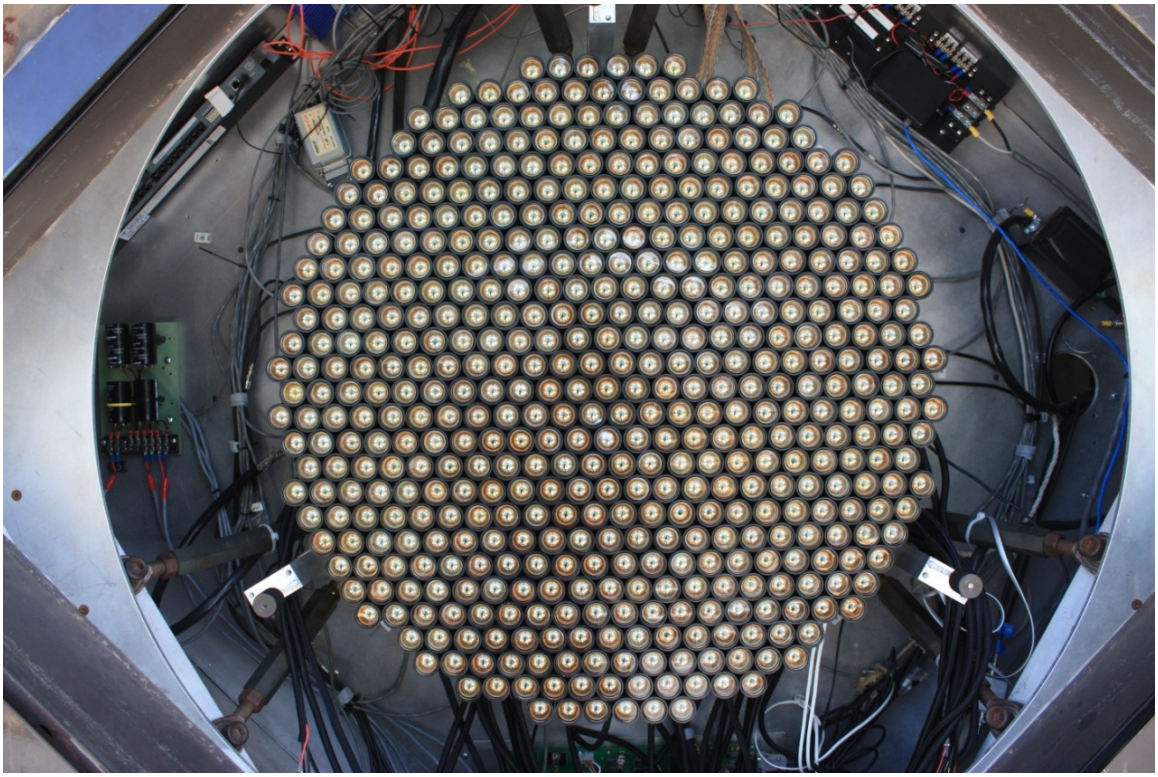

Figure 2-7: View inside the camera box of the 499 PMTs with the light cones removed (credit: Jamie Holder [117])

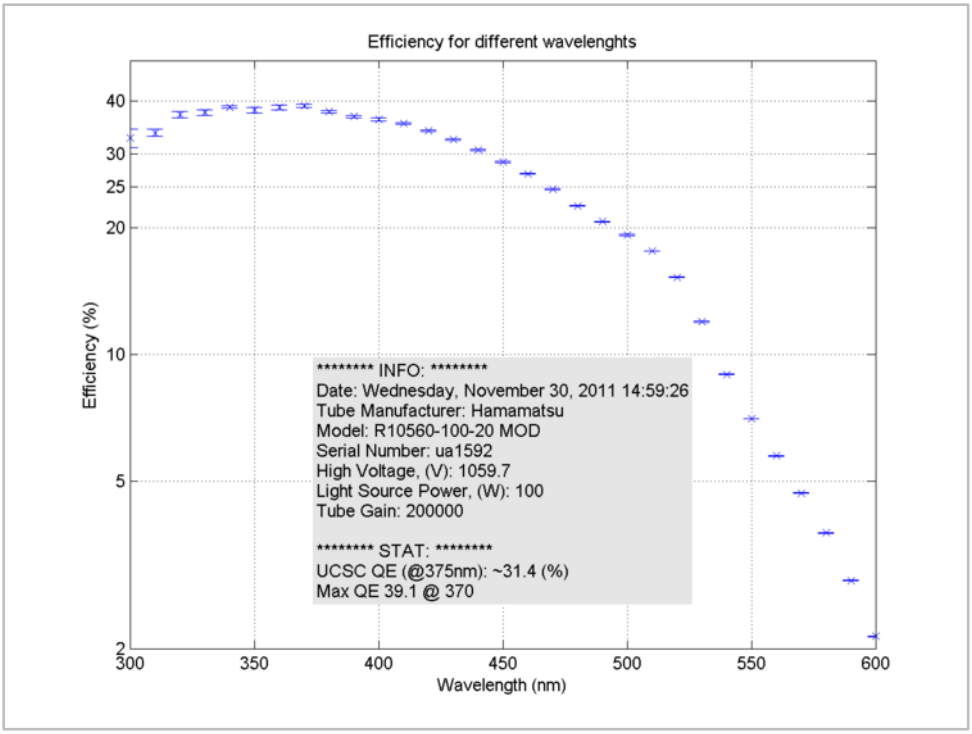

Figure 2-8: Plot of the total efficiency vs. wavelength for Hamamatsu PMT (credit: Purdue PMT testing [118]). Note: total efficiency is the product of the QE and the collection efficiency of the testbed, a coefficient that is very close to unity.

2.5 VERITAS Signal and Trigger Electronics

The signal from the PMT first passes through a preamplifier circuit housed within each pixel. This chip augments the signal amplitude on the way to the data acquisition (DAQ) electronics located in the trailers. Photons strike each PMT at a rate of several hundred MHz, so the signal rise-time of the PMTs must be fast enough (~2 nsec) to record the events.

The Flash Analog-to-Digital Converter (FADC) system then digitizes the incoming analog signal at a sample rate of 500 MHz. The system discretizes the signal into 8 bits (0 – 255 digital counts) and holds it in a 32 μsec ring buffer. For high energy showers the signal from the PMT will exceed the dynamic range of the FADC. When this

happens a high/low gain discriminator switch will attenuate the signal by a factor of 5.8 (6.0 prior to PMT upgrade). If an event is triggered, discussed next, then 24 samples are read out by the Versa Module Eurocard Data Acquisition (VME DAQ). The FADC cannot trigger again while it is reading out so there is a portion of each observing run called dead time that the analysis software accounts for. For a standard run with the upgraded PMTs the dead time averages ~14% with an array trigger rate of 430 Hz.

The hardware systems VERITAS uses to determine an event trigger are divided into three parts: **L1** the single-pixel constant fraction discriminator (CFD) level, **L2** the adjacent 3-pixel pattern, **L3** the multiple telescopes signal coincidence. These three levels not only remove noise coming from the night-sky background but also noise introduced by the electronics themselves. By using stringent criteria to trigger an event, the dead time from the DAQ is kept as low as possible.

The L1 trigger is built into each FADC channel and consists of a CFD coupled with a delay module. The signal from the PMT must rise above a set level to meet the trigger condition. A copy of the signal is also inverted and delayed for a sum comparison by a zero-crossing discriminator (ZCD). This is done to include the negative fluctuations of the PMT as well as improve the minimum detectable energy by reducing coincidence time across the pattern trigger. The noise the night-sky background imprints in the signal can rapidly vary by several hundred percent so the ZCD must account for these variations. The ZCD is constantly adjusted by a rate feedback loop (RFB) to keep up with the impulsive level settings. For dark sky operations the CFDs are set to 45 mV threshold and when the Moon is up the CFDs are increased to 60 mV, while the RFB operates at 60 mV/MHz [119]. Quoting these in more physical terms, the CFD will only admit a signal more than 5 photons/sample during dark sky and 7 photons during moonlight operations (the photon/mV conversion factor is 8.5) [120].

The L2 trigger or pattern trigger requires at least three adjacent pixels pass the L1 requirement within a short 5 nsec coincidence time. This further decreases the probability that single pixel fluctuations due to the night-sky background will trigger an event even if they exceed the CFD threshold. The L2 system was upgraded in the fall of 2011 with

field-programmable gate arrays (FPGAs) having an increased clockspeed, thereby shortening the coincidence window significantly. The FPGAs process two streams of input: the first coming from the emitter coupled logic (ECL) splitter containing the raw CFD data, and the second coming from the pattern selection triggers (PSTs). There are 19 PSTs per camera that determine if the correct configuration of pixels triggered within the coincidence window to qualify as an event [121].

The L3 trigger combines L2 triggers from all four telescopes to pinpoint temporally the same event seen from different vantage points. The electronics for this trigger are housed in the main control building and consist of pulse delay modules (PDMs) and a sub-array trigger board (SAT). The PDMs coordinate the arrival times of the signals traversing unequal lengths of fiber optic cables fed from each telescope's control trailer. The width of the individual pulses will also vary according to the shower's origin and orientation relative to the array. The SAT reads in the PDM-adjusted event times and only records an event if two or more telescopes trigger within the L3 coincidence time (optimized to 50 nsec). Too narrow a window and good γ-ray showers are lost, whereas too wide a window and the cosmic-ray rate shoots up [122]. While the Cherenkov light rings of muons from cosmic-rays make up the bulk of the single-telescope events, the size of their Cherenkov light pool at ground level is rarely large enough to trigger multiple telescopes. The L3 requirement prevents them from entering the data stream. Excluding the muon events allows the array to operate more efficiently with lower dead time and boosts sensitivity to lower-energy γ-rays.

When an event successfully passes all three trigger levels, the VME DAQ sends the FADC signals to an event builder subsystem. An event timestamp is generated by a high-speed GPS clock housed in an auxiliary timing crate. All four event builders funnel their respective telescope's events into a central DAQ machine called the Harvester. Figure 2-9 shows the paths data and triggers follow to the Harvester. This in turn produces array events that are stored in a file type called VERITAS bank format (VBF) for each run. When observers finish nightly operations the VBF files are sent to a dedicated archive at UCLA for storage.

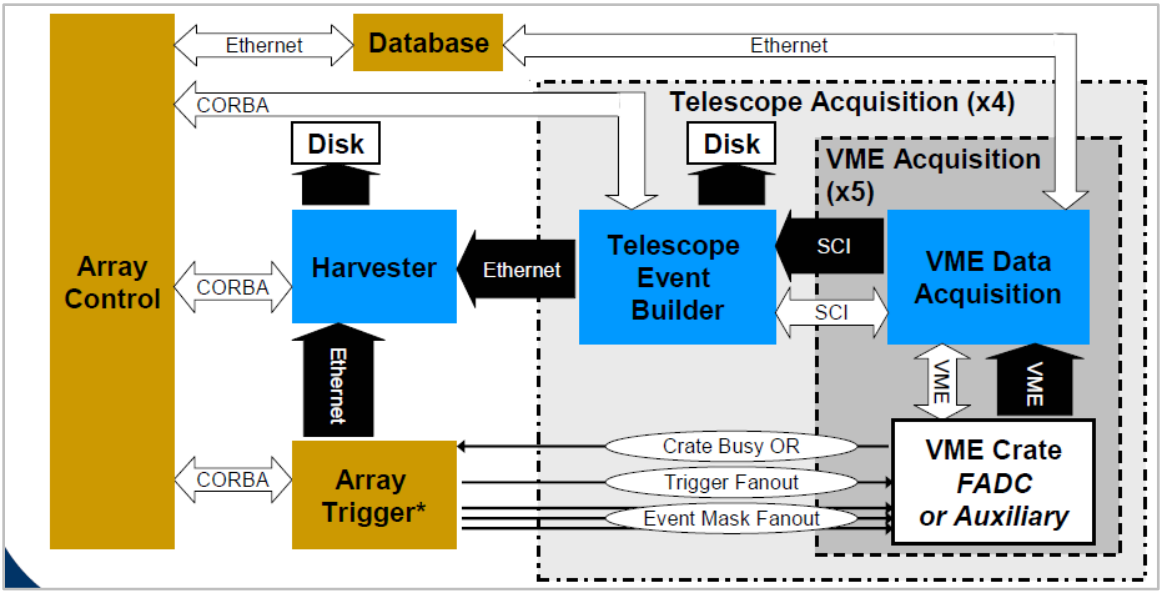

Figure 2-9: Schematic of VERITAS signal and trigger processing (credit: Liz Hays [123])

2.6 VERITAS Data Analysis

In order to extract meaningful results for a γ-ray source from the VBF file VERITAS programmers developed two complementary sets of analysis tools: EventDisplay and VERITAS Gamma-Ray Analysis Suite (VEGAS). This thesis will focus on the latter. The VEGAS architecture is written in C++ and makes use of ROOT dependencies. ROOT is an object-oriented programming language written in C++ developed by particle physicists at CERN starting in 1994 [124]. A normal VEGAS analysis entails processing the VBF file through five stages in succession. Stage 1 calibrates the individual telescope records to adjust for any inter-telescope disparities intrinsic to the hardware. An image cleaning procedure is implemented to exclude faulty pixel data and speed up processing in the later stages. Stage 2 performs Hillas parameterization (see Section 2.6.2) on the calibrated images. (Note: Stage 3 has been deprecated.) From those values Stage 4.2 reconstructs the event's direction and energy. Cuts on the parameters are imposed in Stage 5 to provide γ-hadron discrimination. Stage 6 uses the remaining events to output a variety of results and dataplots including

significance maps, upper limits, lightcurves, and spectra. Details are provided in the following subsections. Table 2-1 lists the relevant values that are used in different stages of VEGAS to produce soft cuts.

Table 2-1: The cuts applied to the data in the last three stages of VEGAS (credit: Glenn Sembroski [125]). Stage 4.2 quality cuts are covered in Section 2.6.3 . The details of the three array configurations are given in Section 2.4 . γ-hadron shower cuts in Stage 5 are described in Section 2.6.4 . The cuts used in Stage 6 (Section 2.6.5) are specific to each cluster.

VEGAS Stage	Cuts Values
4.2 – Old Array (pre-2009)	Distance < 1.43° Image size > 200 digital counts. Minimum # of pixels in image = 5 Exclude T1-T4 pairs
4.2 – New Array (2009-2012)	Distance < 1.43° Image size > 200 digital counts Minimum # of pixels in image = 5
4.2 – Upgrade Array (post-2012)	Distance < 1.43° Image size > 400 digital counts Minimum # of pixels in image = 5
5	0.05 < MSL < 1.3 0.05 < MSW < 1.1 Minimum height of the Shower maximum (SHM) = 7 km
6	Source region ring size = R_{500} Search window square cut = R_{500}^2

2.6.1 Calibration – Image Cleaning

The FADC adds a small level of bias voltage (pedestal) to the signal waveform before the CFD performs the L1 trigger check so negative fluctuations in the PMT signal due to the night-sky background can be recorded. The pedestal is unique to each pixel, so to determine the mean pedestal and pedestal variance (pedvar) a distribution of pedestal values is constructed at every 90 seconds throughout a run. The statistics of those distributions yield the average light level and noise of the night-sky background. Stage 1 subtracts the pedestal from the FADC trace before integrating over the sample window to determine the total charge deposited in the pixel by the Cherenkov radiation.

Even though the gains of the PMTs were triple-checked before installation, the PMTs experience a downward gain drift of ~10% per year due to aging effects on the photocathode and the dynodes near the terminus of the electron cascade. The seasonal flat-fielding procedure includes a voltage boost to correct for this. Nevertheless, there are small differences in the relative gains between pixels that affect the total amount of charge they collect. A novel flasher system was devised at McGill University to normalize their integrated charges. It consists of seven LEDs housed in a Maglite flashlight case pointed at the camera face [126]. The LEDs, peaked in the UV (375 nm), cycle through eight increasing light levels in short bursts of ~10 nsec through a diffuser made of a thin slice of opal. See Figure 2-10 for a look inside one of the flashers. During nightly observing the telescopes are pointed at an area of blank sky and the flasher fires at 300 Hz for two minutes. Stage 1 requires every data run have an associated flasher run to compute the required correction.

The camera images of the events then pass through an image cleaning routine. Malfunctioning or noisy pixels are easily identified as outliers within the gain, pedestal, or pedvar distributions and are excluded. To form a clean image the total charge of a pixel is compared to its pedvar. If the charge exceeds the pedvar by a factor of five or more it is labeled a picture pixel and is included in the image. Likewise if the charge falls

in the range of 2.5 – 5 times the pedvar and borders a picture pixel it is added as a boundary pixel in the image. Any pixels with less charge than that are not included in the image and have their charge zeroed out.

Figure 2-10: View inside the flasher with the diffuser removed
(credit: Dave Hanna [126])

2.6.2 Hillas Parameterization

The cleaned images of showers resemble 2-D elliptical Gaussians in the plane of the camera, as mentioned in Section 2.3. Stage 2 computes the 1st, 2nd, and 3rd moments of these ellipses and then parameterizes them by fit and type. Figure 2-11 details the important Hillas parameters as they relate to the ellipse. γ-hadron separation using this technique was pioneered in the historic discovery of TeV γ-rays from the Crab Nebula in 1989. Trevor Weekes and his collaborators took 60 hours of on-source data with the 10 meter Whipple Observatory IACT. By comparing their data to Monte Carlo simulations

of γ-ray and hadronic showers, they detected the first VHE γ-ray source at 9 σ above background [127].

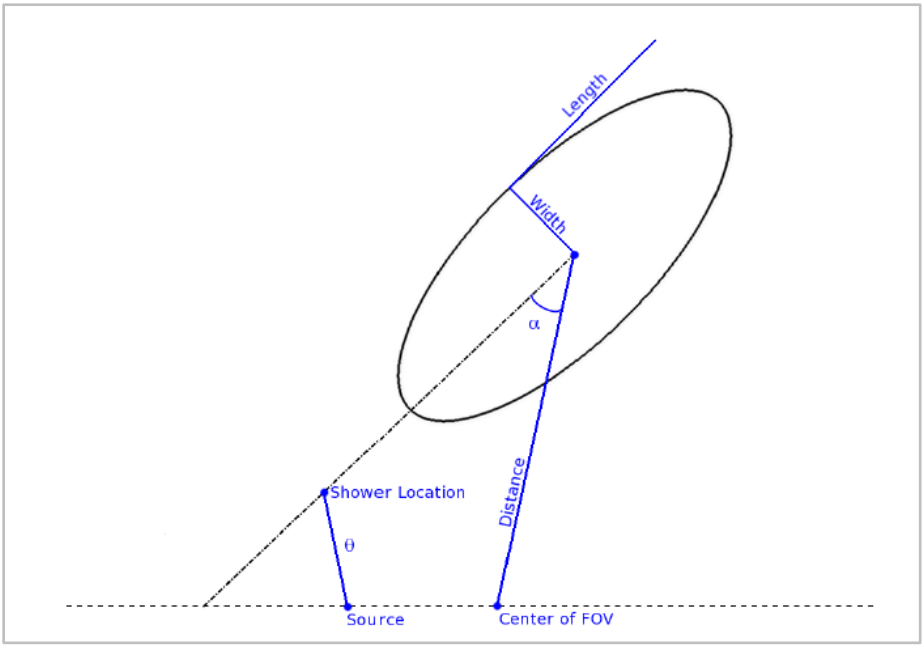

Figure 2-11: Diagram representing an image's Hillas parameters
(credit: Daniel Gall [128])

2.6.3 Stereoscopic Direction – Energy Reconstruction

Retracing the major axis of an image backwards gives the line along which the shower must have originated. A single image cannot accurately gauge depth, however, so multiple telescopes' views of the same shower are necessary to localize the source on the sky. To achieve this all four images are plotted on a common plane. The major axes are extended until a crossing or region of overlap appears. The lengths of the perpendicular lines extending from each major axis are minimized with a weighted root-mean-squares (RMS) procedure. Their intersection is taken to be the image centroid [129]. Figure 2-12 depicts this concept.

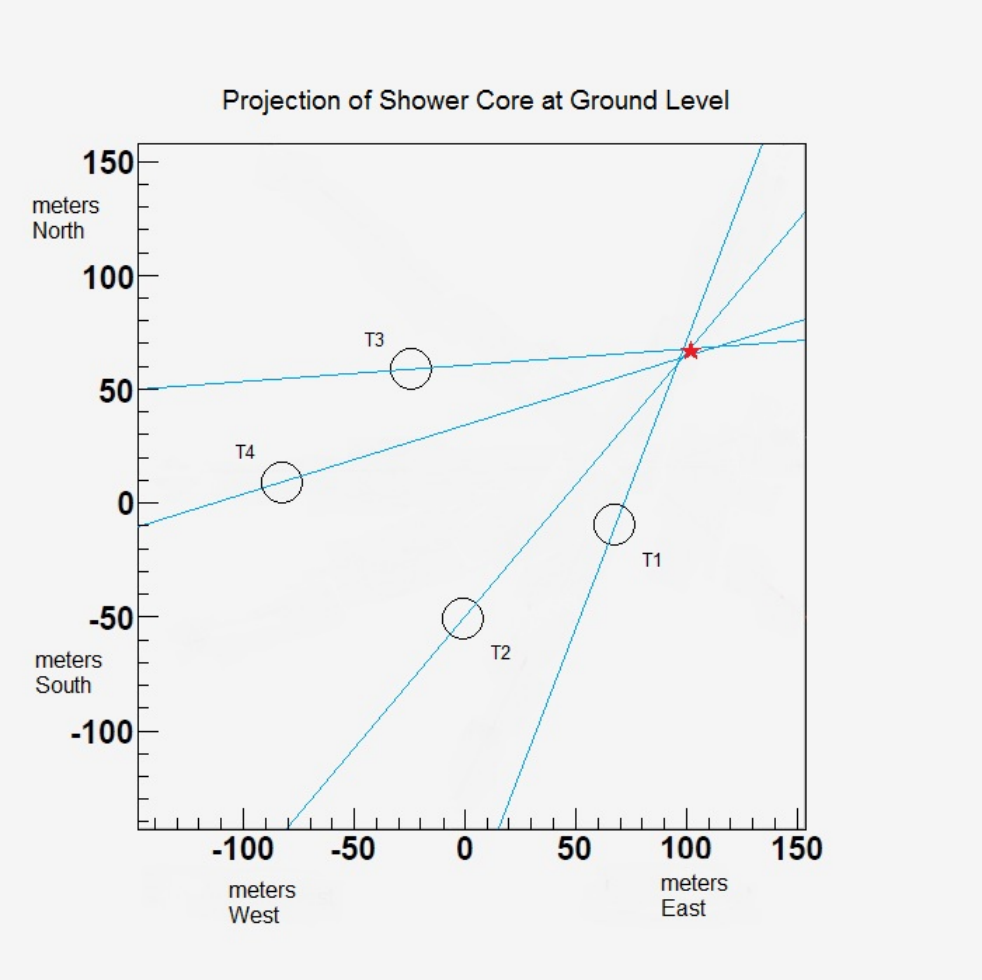

Figure 2-12: Source localization by overlapping axes (adapted from John Millis [130]). The four circles represent the locations of the four telescopes from the center of the array (the origin). The impact distance of each telescope is found by extending (blue) lines along the major elliptic axis of each camera image until they overlap. The ground projection of the shower core (red star) is placed at the location that minimizes the perpendicular distance from each of the blue lines.

This stereoscopic reconstruction method works best for bright showers originating near the center of the array. Lower energy events with a small number of pixels tend to create more circular than elliptical images, thereby introducing greater error on the major axis direction. Additionally, images on the edge of the FOV may not be fully contained by the pixel boundary. A set of quality cuts implemented in Stage 4.2 ensure high

reconstruction efficiency by eliminating those images with the largest errors. For soft cuts (most sensitive to DM annihilation) an image must contain at least 200 or 400 digital counts pre-/post-PMT upgrade respectively. The size cut not only leaves out dimmer showers but also those with a low degree of ellipticity. An image must also contain at least five pixels for the parameterization to give sensible information. To prevent truncation at the edge, an image distance cut of $d < 1.43°$ is imposed. The stereoscopic technique needs at least two telescopes to function, and T1-T4 image pairs prior to T1's move in 2009 are discarded because the baseline was too small (35 meters).

Knowing a photon's energy is essential to produce a spectrum and further characterize a source by the hardness of its photon index p. The energy of the incident γ-ray however cannot be worked out purely by the size of the image or its Hillas parameters. For that an extensive catalog of simulated γ-ray showers called a lookup table is referenced. The table is organized by seven parameters: zenith angle, azimuth angle, telescope ID, signal noise level, telescope offset, image size, and impact parameter. Impact parameter is a measure of the shower's propagation axis projected onto the plane of the ground from the center of the array. Showers with a large impact parameter will focus their Cherenkov light cone far from the telescopes, corresponding to lower PMT currents. The density of the atmosphere as a function of altitude and the local aerosol content are important factors in determining the extinction coefficient for the Cherenkov radiation. The Earth's magnetic field also imparts small differences to the shower propagation depending on its azimuth and elevation angles. The Monte Carlo simulations create millions of γ-ray showers per lookup table across the whole range of the parameter-space out to a maximum impact distance of 750 meters. The length, width, and energy (from 20 GeV to >50 TeV) of the simulated γ-ray shower are stored with each entry [131]. The camera images of real data are then cross-referenced against the lookup table to reconstruct the shower and its energy. Once constructed, the lookup table is static and cannot account for slight variations in atmospheric propagation intrinsic to each shower. Therefore the discrepancy between the shower's true energy and reconstructed energy manifests itself as a systematic error called the energy bias that varies as a function of energy. Energies with too great an energy bias, typically at the low and high

extremes, are not fit with spectral points. Further discussion of KASCADE lookup tables is covered in Section 3.5 .

2.6.4 γ-Hadron Separation

The process of discerning γ-rays from the cosmic-ray background by their respective Hillas parameters is completed in Stage 5. Making cuts on the image length and width is the most powerful way to remove cosmic-rays. Hadronic showers tend to have greater lengths and widths than γ-ray showers. Two values called mean scaled length (MSL) and mean scaled width (MSW) are derived from the data and simulations' Hillas parameters. They are defined as:

$$MSL = \frac{1}{N_{tel}} \sum_{i}^{N_{tel}} \frac{L_i}{L_{sim}(zen, size, d)} \quad (2.7)$$

$$MSW = \frac{1}{N_{tel}} \sum_{i}^{N_{tel}} \frac{w_i}{w_{sim}(zen, size, d)} \quad (2.8)$$

where N_{tel} is the number of telescopes present in the event, L_{sim} and w_{sim} are the average lengths and widths of the entries in the lookup table closest to the real event in zenith angle, size, and impact distance. Both MSL and MSW would return a value of 1.0 for a pure γ-ray signal since the lookup table is populated only with γ-rays. The real data distributions, obtained from nightly observations containing a mixture of γ-ray and hadronic showers, peaks at 1.6 in MSL and at 1.3 in MSW, with both having long high-side tails. The soft cuts used here place an upper bound on the MSL at 1.3 and the MSW at 1.1 to remove the most cosmic-rays. Additionally a cut on the lower bound of the shower height maximum (SHM) at 7 kilometers prevents deeper-interacting low energy cosmic-rays from masquerading as γ-rays. These Stage 5 cuts are effective at removing the vast majority of hadrons from the signal and lower the VERITAS threshold

reconstructed energy to 100 GeV. Below 100 GeV, cosmic-ray image ellipses cannot be differentiated from γ-ray ones due to their small size, and because the energy bias becomes too large. Figure 2-13 compares the MSW distributions for γ-ray simulations, cosmic-ray simulations, and real data.

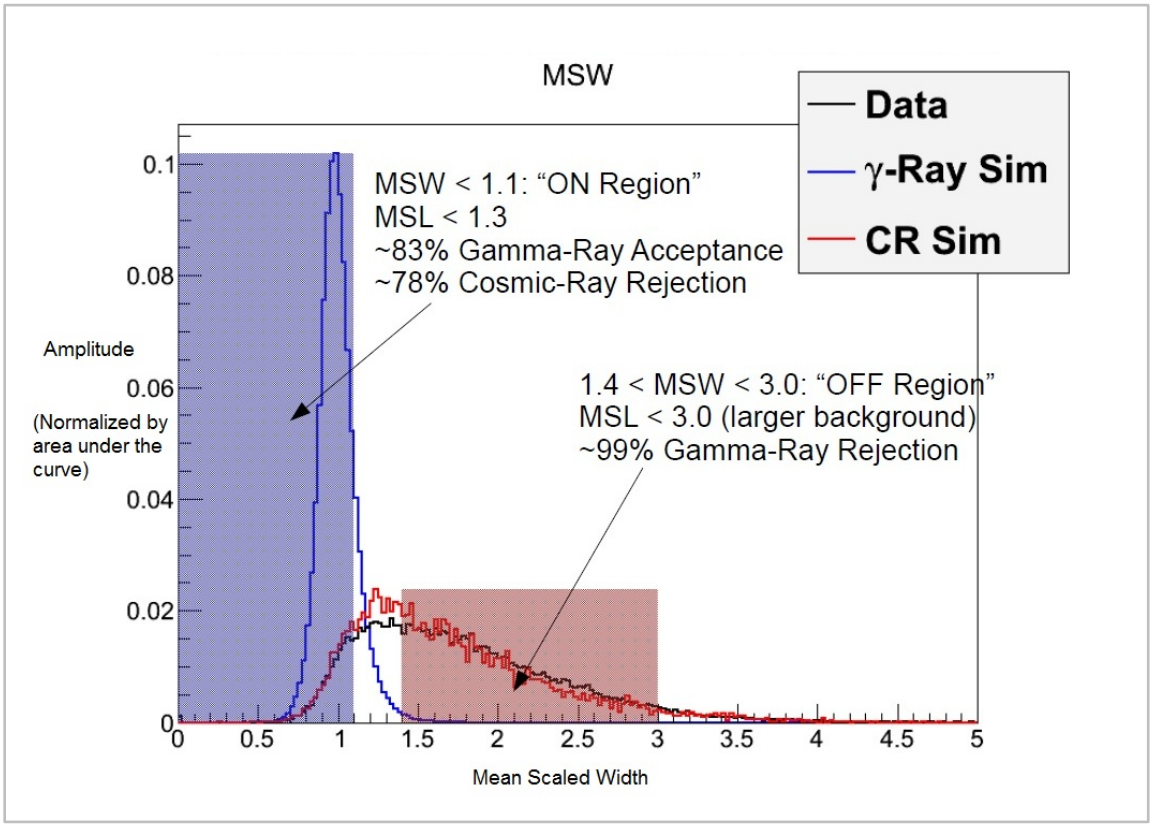

Figure 2-13: The MSW distributions for γ-ray simulations, cosmic-ray simulations, and real data (credit: Ben Zitzer [132]). The left shaded region covers the parameter space preserved by the soft cuts. The right shaded region is used as the cosmic-ray background region in Ben Zitzer's template method (see Section 2.6.6). The real data MSW distribution is an admixture of the γ-ray and cosmic-ray curves.

2.6.5 Background Estimation – Results

After this round of shape cuts the signal should be comprised almost entirely of γ-rays in the presence of a source. For accurate source localization on the 2D skymap plot (RAxDec) a ring of angular radius corresponding to R_{500} is placed at the coordinates of the galaxy cluster. It is worth noting that this may not necessarily be the telescope pointing direction for every cluster. This defines what is known as the on-source region. A θ^2 cut on the arrival direction of γ-rays from this ring further constrains the signal to define the source counts. Stage 6 of VEGAS allows three standard options for defining the background or off-source region: ring background model (RBM), reflected rings model (RF), and crescent background model (CBG). Figure 2-14 lays out the differences between each model [133]. RBM was chosen as the preferred background model for the following reasons: 1) RF fails for clusters of large angular size because background regions of identical size to the on-source region would extend past the edge of the camera. 2) CBG fails for clusters with a large angular displacement from the tracking center because the annulus of the background region would also extend past the edge of the camera.

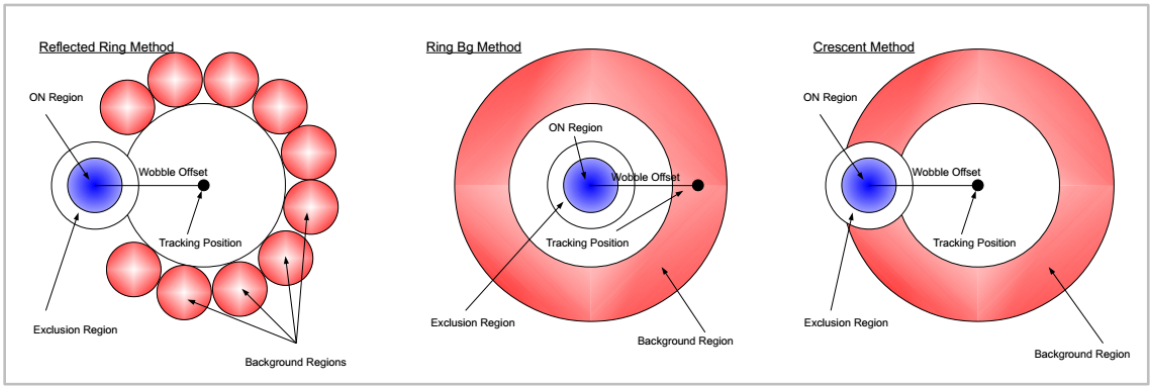

Figure 2-14: Comparison of the three background estimation models
(credit: Ben Zitzer [133])

With a single telescope instrument (i.e., Whipple Observatory) on-source and off-source runs had to be completed separately. With current instruments simultaneous source and background estimation are possible by wobbling the telescope tracking position around the source location. This involves taking separate runs at a 0.5° offset north, south, east, and west of the source. This scheme reduces the systematic uncertainties in filling the background ring and provides a more uniform radial acceptance profile to large angles [134].

The signal from the source rising above the background is computed by taking the difference:

$$N_{Excess} = N_{ON} - \alpha N_{OFF} \quad (2.9)$$

where N_{Excess} is excess counts, N_{ON} is counts from the source region, N_{OFF} is counts from the background ring, and α is a scale factor equivalent to the integral acceptance of the source region divided by the integral acceptance of the background ring. It is important to note that the size of the ring and the α parameter are adjusted to exclude known bright stars that might be present in the skymap that would contaminate the calculations.

A rudimentary significance calculation based on Poisson statistics (small numbers) can be found by dividing the excess counts by the standard deviation of the excess:

$$Sig. = \frac{N_{ON} - \alpha N_{OFF}}{\sqrt{N_{ON} + \alpha^2 N_{OFF}}} \quad (2.10)$$

A stronger significance calculation based on the likelihood ratio method is more appropriate for larger N_{ON} and N_{OFF}. It finds the probability that no signal comes from the source and all comes from the background, meaning that the null hypothesis is true. If it is true then the probability fits a χ^2 distribution with one degree of freedom (d.o.f.). The square root of the distribution is called the normal variable which in this case corresponds to the Gaussian significance:

$$Sig. = \sqrt{-2\ln\lambda} = \sqrt{2}\left\{N_{ON}\ln\left[\frac{1+\alpha}{\alpha}\left(\frac{N_{ON}}{N_{ON}+N_{OFF}}\right)\right] + N_{OFF}\ln\left[(1+\alpha)\left(\frac{N_{OFF}}{N_{ON}+N_{OFF}}\right)\right]\right\}^{\frac{1}{2}} \quad (2.11)$$

In γ-ray astronomy the standard to claim a source detection is 5 σ, or a one in 1,744,278 chance that the signal is just a random background fluctuation [135]. A differential energy spectrum is deemed valid if a source is detected at this level. The Li & Ma method for calculating significance is only valid when N_{ON} and N_{OFF} are not too small, taken to be greater than 10 counts each.

If the 5 σ level is not reached for a source, upper limits on excess counts and flux can be found by following the Rolke method [136]. The Rolke method is discussed in Appendix C. A 95% confidence level upper limit is calculated for each source using the on-source and off-source counts. A stacking procedure to combine the limits will show an even more stringent limit than any individual limits. The next chapter on methodology will investigate relevant sources and techniques used along the way to the final goal: a combined limit from galaxy clusters.

2.6.6 Special Analysis Techniques

There are a number of prototype statistical analysis methods still being vetted before being implemented into the VEGAS source-code that should be mentioned as well. They are improvements on the Hillas method designed to yield greater statistics and better fits for extended sources, sources at large zenith angle, or sources near the edge of the camera. A brief description of each is below:

- Several variants of the Maximum Likelihood Method (MLM): Boosted decision trees are a type of neural network that trains the Hillas parameters through a sequence of trials. The method suppresses the background events (cosmic-ray showers) versus the γ-rays of the astrophysical objects. The advantage MLM has over RBM, RF, or CBG is that it does not require a background region. MLM

disentangles the intrinsic source morphology from the instrument response function by incorporating the γ-ray PSF and effective area into the source model [137].

- A fully Bayesian DM analysis: Unlike the Hillas parameterization that requires each value be optimized *a priori* on simulations before being applied to real data, the Bayesian method invokes conditional probabilities to examine the full multi-dimensional parameter space before drawing conclusions. This method was used on dSph data to produce modest sensitivity increases through greater effective areas. The Bayesian method is also being used on a VERITAS paper by Jim Buckley and Nathan Kelly-Hoskins (in prep.) looking for DM annihilation in the GC [138].
- 3-Dimensional parameterization of the shower model: Instead of solving for an image's Hillas parameters, the 3-D model parameterizes the shower as a prolate spheroid (e.g., football) of particles in the atmosphere and solves for the Gaussian width of each of the three principle axes. This method can discriminate low energy γ-rays from cosmic-rays more effectively by the height of their shower maxima than the standard cuts on the width and length parameters [139].
- Several template image methods (i.e., Ben Zitzer's template, FROGS: Fancy Reconstruction by Optimization over Gamma-Ray Simulations, HFit): Template analyses compare the camera images received to a catalogue of images generated by Monte-Carlo simulations. If a camera image is missing pixels due to a bright star suppressing them or if part of the image extends past the edge of the camera, template methods would be able to reconstruct that γ-ray whereas the Hillas method would not. Instead of defining on- and off-source regions on the skymap, Ben Zitzer's template assumes the γ-rays are coming from the source and the cosmic-rays are emitted isotropically. The cuts on width and length divide the distribution into a γ-ray and cosmic-ray region. Those regions are then subtracted to yield the source morphology which can be more extended than the Hillas method can be optimized for [132]

CHAPTER 3. METHODOLOGY

3.1 Crab Nebula

The first source any young researcher in the VERITAS collaboration will analyze is the Crab Nebula. It is referred to as the 'standard candle' of γ-ray astronomy and all other sources' fluxes are quoted in terms of it (i.e., a percentage of the Crab flux). All IACT arrays are able to observe it at some point during an observing season (83.63°x22.01° in RAxDec) and dozens of papers have been written about it. Within VERITAS it is with great pride to the enduring memory of Trevor Weekes that the Crab Nebula continues to be studied.

A VERITAS study led by Kevin Meagher and A. Nepomuk Otte (in prep.) seeks to characterize the steady-state emission of the nebula and the pulsed emission by the pulsar located in its center over several years. Some of the results of the secondary analysis of the nebula's flux carried out at Purdue are presented in Figures 3-1 and 3-2.

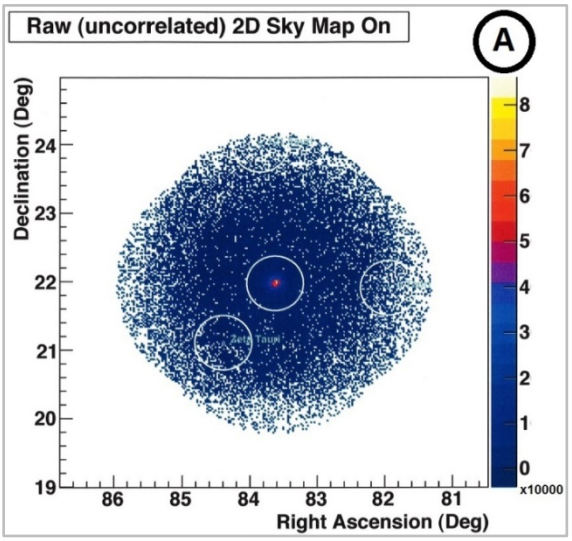

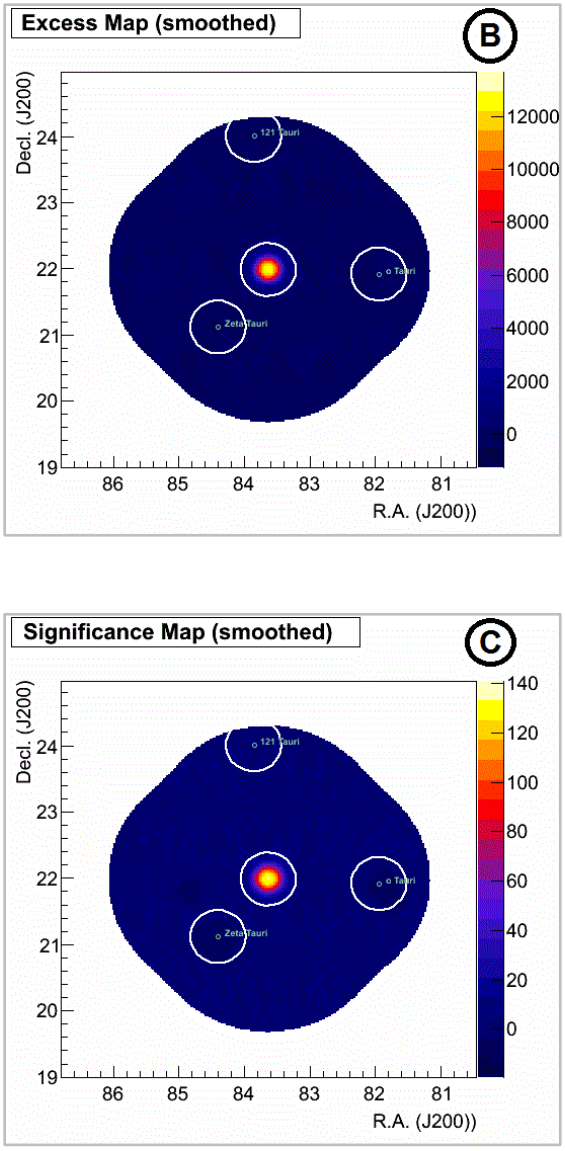

Figure 3-1 (panels labeled A, B, C): Three skymaps for the Crab Nebula. Panel A shows all the γ-ray counts VERITAS detected during the exposure. The Crab Nebula is the hotspot in the center. Panel B shows the excess signal counts that remain after background subtraction and acceptance correction. Panel C computes the 2-D spatial distribution of the significance from the signal counts by the Li & Ma method [135].

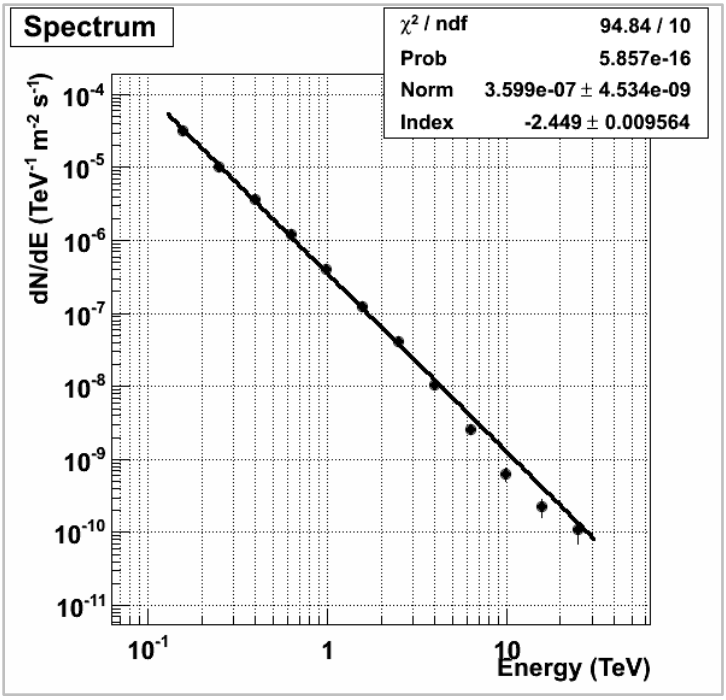

Figure 3-2: Spectrum for the Crab Nebula fit with a power law. It should be noted that the spectrum deviates from the fit at high energies suggesting that other emission mechanisms are at work. Others have proposed broken-power law or log-parabolic fits to the data, however at the current time no consensus theoretical explanation satisfies the data.

Significance skymaps and spectra are among the output files produced once Stage 6 completes. The placement of the spectral points within the equal width $\log_{10} E$ bins follows the procedure of Lafferty and Wyatt [140] [141]. The Crab Nebula was observed for 18 hours of quality-selected live time in wobble mode during the 2011 – 2012 observing season. To give a sense of how much more sensitive the VERITAS array is than its single-telescope predecessor Whipple, the significance for the Crab Nebula with RBM analysis and soft cuts is 164 σ. This dramatic sensitivity increase over the original Whipple detection came in only 1/3 the exposure time [127].

Since the detection is well above 5 σ, a differential energy spectrum is produced based on the effective area of the array in the applicable array configuration and observing season. The aim of the upcoming paper is to confirm that the normalization

and photon index of the nebula does not vary drastically between array configurations or observing seasons. Once the standard candle is well-constrained, then the systematic errors of the hardware and analysis software can be better understood.

3.2 Dwarf Spheroidal Galaxies

As discussed in Sections 1.3 and 1.5, dwarf spheroidal galaxies are promising nearby targets for indirect DM detection because their mass-to-light ratio is large and there is little appreciable γ-ray background from other astrophysical sources. VERITAS has taken deep exposures on five dSphs and will continue to observe them as long as operations continue for the Dark Matter, Astroparticle, and Extragalactic Science Working Group (DM-AsPEN SWG).

A VERITAS paper spearheaded by Ben Zitzer and Alex Geringer-Sameth (in prep.) combines the results from these five dSphs with a stacking analysis to reach a more stringent limit on the WIMP velocity-weighted cross-section $<\sigma v>$ than each dSph alone. Some of the results of the secondary analysis carried out at Purdue are presented in Figures 3-3 and 3-4 and Table 3-1 [142].

The data were processed through Stage 6 with CBG analysis (see Figure 2-14) and soft cuts [133]. Camera images were fit with a 2D Elliptical Gaussian to improve shower reconstruction efficiency. Despite their respective long exposures, none of the dSphs appears to be approaching the 5 σ level needed for detection. Instead the Rolke method was employed to find upper limits on counts and flux with an assumed spectral index p of 2.4 [136]. The choice of DM spectral index matches the shower cuts which were optimized to maximize significance of the detection for a soft source with 3% of the Crab Nebula flux and a power-law spectrum [9]. These limits will become the basis for the dSphs' exclusion plots very similar in form to Figure 3-4, taken from an earlier VERITAS paper on the Segue 1 dSph [78]. The particle physics term in equation 1.8 is

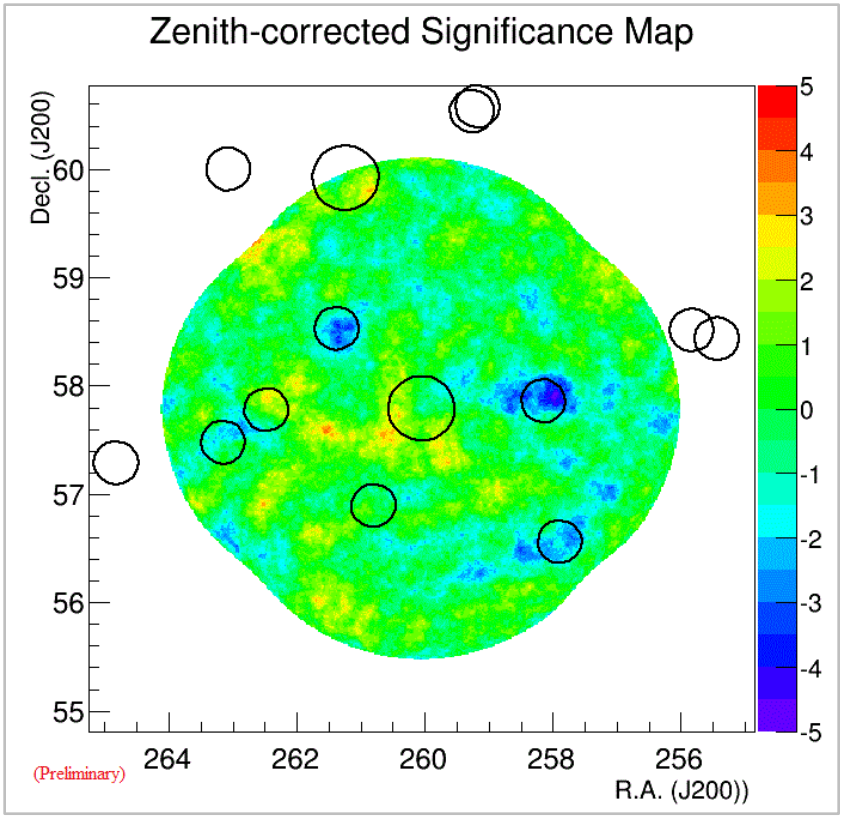

Figure 3-3: Significance map for Draco dSph (target located in the ring in the center). Stars with B-magnitude < 8.0 are identified with the Hipparcos star catalogue and excluded from the background estimation. The radii of the black rings are inversely proportional to the stars' B-magnitudes. Stars are excluded for two reasons: 1) starlight falling on the PMTs produces too many photoelectrons that the high voltage software suppresses those pixels to prevent damage and 2) the Hillas parameterization code in Stage 2 of VEGAS has difficulty reconstructing events that overlap a star. This then becomes interpreted by Stage 6 as a region of large negative significance (a hole). For deep exposures like that of Draco dSph a zenith correction was implemented to rectify the anisotropic event rate that relates to the zenith angle by $\frac{dN}{dt} \propto \frac{1}{\cos z}$.

Table 3-1: Preliminary results for the five VERITAS dSphs. The columns are dSph name, distance in kpc, exposure time in hours, Li & Ma method Gaussian significance in σ, Rolke counts upper limit, threshold energy in GeV for the upper limit calculation, Rolke integral flux upper limit in photons/cm^{2}s above 300 GeV

dSph	Distance (kpc)	Exp. (hr)	Std. Dev.	UL (cts)	E_{Th} (GeV)	Int. Flux UL ($cm^{-2}s^{-1}$ above 300 GeV)
Boötes I	62	14.0	-1.04	40.3	170	4.97e-13
Willman I	38	13.7	-0.63	70.5	180	1.18e-12
Draco	80	49.9	-1.04	84.1	220	3.41e-13
Ursa Minor	66	59.7	-0.01	79.1	290	3.41e-13
Segue I	23	91.9	0.72	289.9	150	4.16e-13

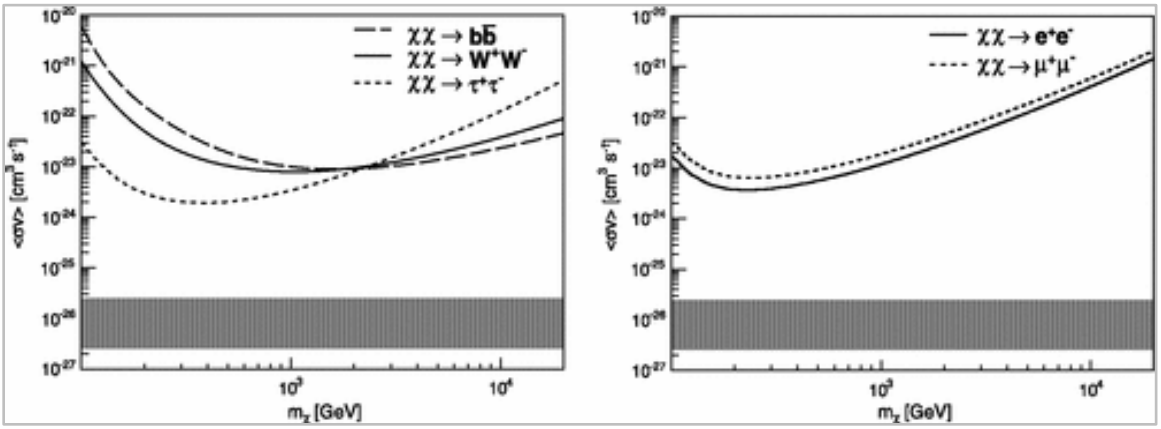

Figure 3-4: Two exclusion plots showing cross-section versus WIMP mass for annihilation to several final states for Segue 1 dSph (credit: [78]). The thermal relic cross-section with ± 1σ error bars is the shaded black band.

calculated using a particle physics event generator called PYTHIA [143]. Much work was required to compute the dwarves' J-factors because of the inherently low numbers of stars present in dSphs with which to create an orbital velocity profile [144].

3.3 Galaxy Clusters and Stacking Procedure

The following selection criteria were implemented within the VERITAS Runlist Builder (VListBuilder) and the VERITAS Run Log Generator (loggen) to ensure the best data quality for the analysis [94] [145]:

- Date 09/2007 to present
- Weather ≥ C
- $N_{tels} = 4$
- Zenith angle < 40°
- Acceptance cut > 50% → fiducial volume < 1.225° from tracking center
- Labeled good run, data category science
- Stage 5 timecuts based on L3 rates, weather, DQM comments
- Duration > 5 min

VERITAS has been fully operational since September 2007 so data taken prior to that date was excluded. The Vaisala CL51 laser light detection and ranging (LIDAR) system on-site assists the observing team in their A through F grading of the weather by displaying cloud heights and the amount of atmospheric backscatter [146]. To maximize the array's effective area and reduce the energy threshold to possible DM annihilations, only 4-telescope data was used. The intensity of the Cherenkov radiation is attenuated by the length of the atmosphere it must traverse, hence smaller zenith angles improve data quality. The radial acceptance of the array peaks at the tracking center and drops off as a function of angular separation. By sampling a number of low-flux (not detected)

extragalactic γ-ray targets it was determined that the acceptance of the array fell to half its nominal value a distance of 1.225° ($\sqrt{1.5}$) from the tracking center. The same behavior is observed in the dark field runs that are used for calibration. Using VListBuilder, only data taken in a wobble position where the angular separation was less than this value were included.

The observers keep a detailed log file of the status of the array as nightly operations progress. Only science data (i.e., not calibration or troubleshooting data) free of equipment problems passes the cut. Additionally a data quality management (DQM) team reviews the diagnostics of the array the day after observations are taken. They often find smaller problems in the data that do not become apparent until further post-processing is performed. The trigger rate that passes L3 will fluctuate dramatically due to passing clouds or the sun-/moon-rise. These have nothing to do with γ-ray showers so the DQM team will make a note of it and that section of a run can be cut within the configuration options of Stage 5. A secondary effect of the selection criteria is that all useable runs have duration greater than 5 minutes. Any runs shorter than that were most likely plagued by equipment problems and aborted or have such variable L3 rates that the DQM team flagged it wholly.

What began as 21 prospective clusters from the two parent surveys totaling ~250 hours of VERITAS data was systematically pared down by the selection criteria to 12 clusters totaling 150 hours. Those results are displayed below in Table 3-2. A joint VERITAS and Fermi paper derived DM annihilation upper limits on the Coma cluster, and this analysis will seek to replicate those results with an updated version of VEGAS [147]. The new version of VEGAS (v2.5.2) includes multiple bug fixes, including a ~1.3% correction to the plate-scale and fixed the handling of dead-time when making DQM timecuts [125]. The Perseus cluster poses additional challenges because it contains two γ-ray detected galaxies, NGC 1275 and IC 310, whose contributions to the γ-ray signal must be excluded. A large number of Perseus data runs were taken with custom pointings that will require special processing. A separate analysis method may be required for these clusters due to the intrinsic limitations of RBM with very extended

sources. A secondary analysis is being undertaken by a collaborator at University of Delaware with EventDisplay to check these results.

Table 3-2: Table of results for the 12 galaxy clusters. The columns are cluster name, spectroscopic redshift, exposure time in hours, Li & Ma method Gaussian significance in σ, counts upper limit by the Rolke method, threshold energy in GeV for the upper limit calculation, integral flux upper limit in photons/cm^{2}s by the Rolke method.

Cluster Name	Redshift (z)	Exp. (hr)	Sig. (σ)	UL (cts)	E_{Th} (GeV)	Int. Flux UL ($cm^{-2}s^{-1}$ above E_{Th})
NGC 507	0.0169	2.3	-0.04	95	151	1.87e-11
NGC 1550	0.0131	23.9	2.02	522	200	8.16e-12
3C 129	0.0220	11.5	1.21	861	166	3.27e-11
UGC 9534	0.0520	14.0	-1.11	83	166	2.84e-12
A2199	0.0299	12.5	2.33	733	151	3.70e-11
A400	0.0238	3.5	0.03	97	219	6.27e-12
A1213	0.0468	0.5	0.37	68	151	7.58e-11
SDSS-C4-DR3 1079	0.0490	0.6	0.32	43	182	1.98e-11
[YSS 2008] 265	0.0846	0.4	0.52	16	138	2.10e-11
A279	0.0790	6.9	0.19	44	200	2.20e-12
Coma	0.0231	16.7	2.55	1721	166	5.02e-11
Perseus	0.0179	56.3	-0.04	4119	182	3.72e-11

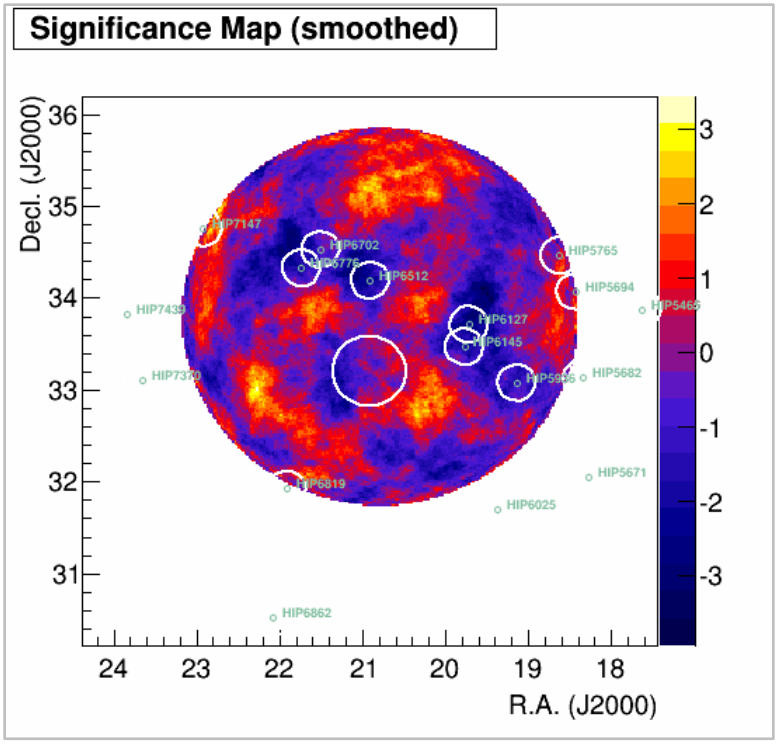

Figure 3-5: Target: 1ES 0120+340, Cluster: NGC 507 (same as Figure 3-1)

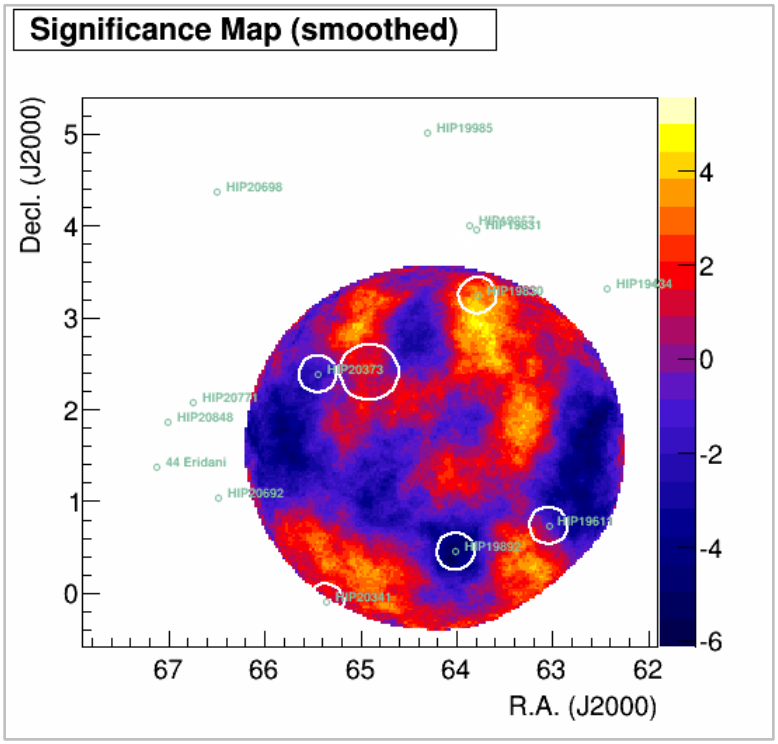

Figure 3-6: Target: 1ES 0414+009, Cluster: NGC 1550 (same as Figure 3-1)

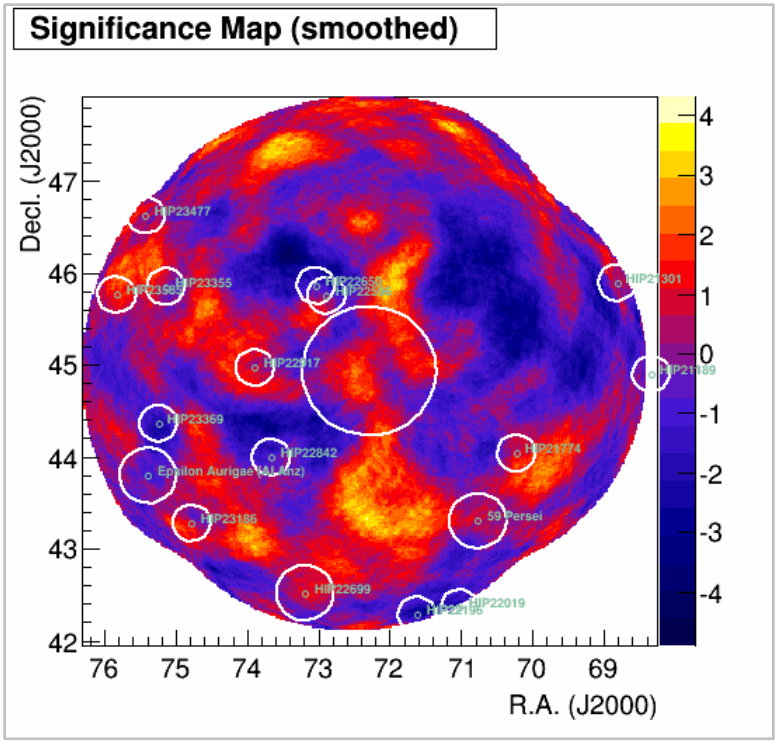

Figure 3-7: Target: 1ES 0446+449, Cluster: 3C 129 (same as Figure 3-1)

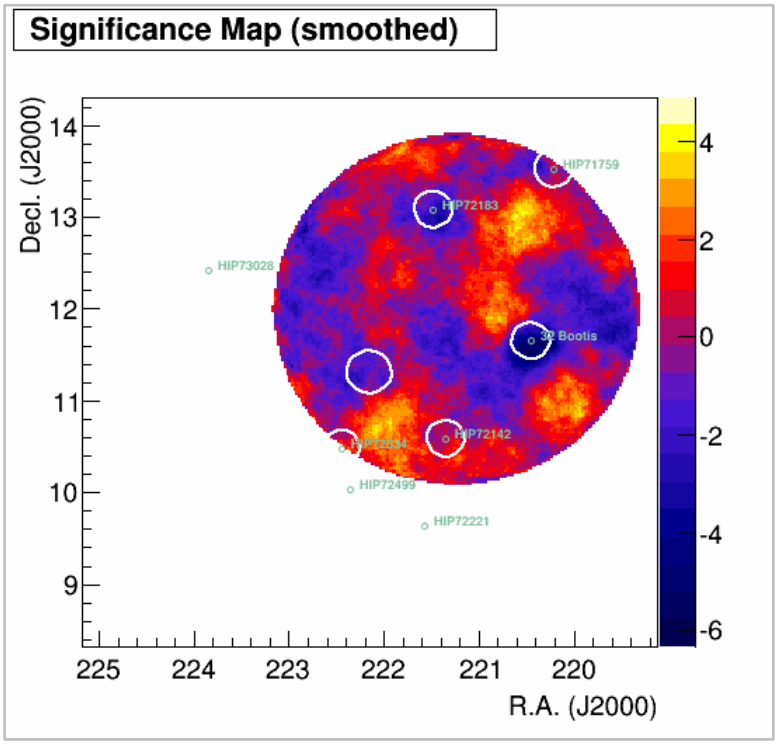

Figure 3-8: Target: 1ES 1440+122, Cluster: UGC 9534 (same as Figure 3-1)

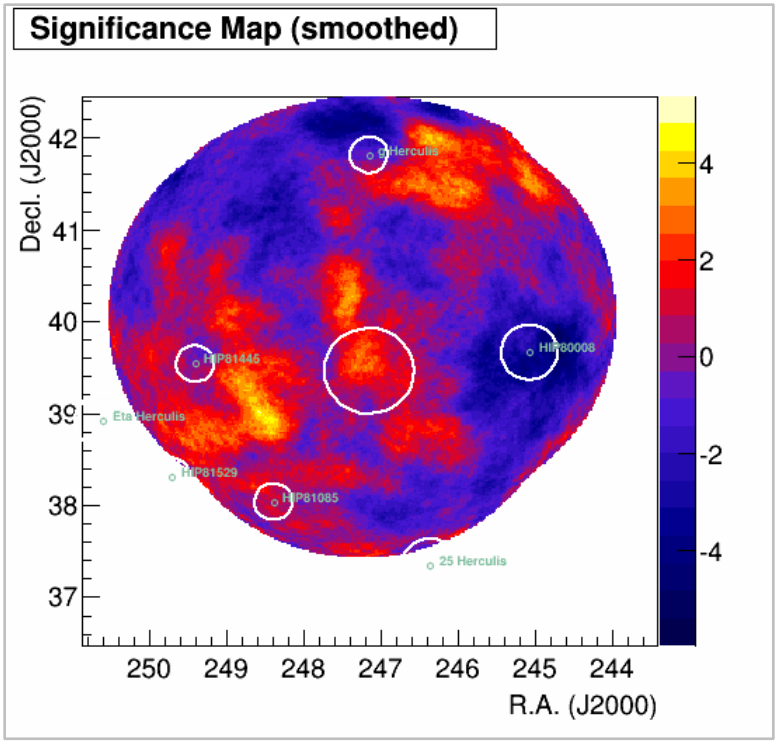

Figure 3-9: Target: 1ES 1627+402, Cluster: A2199 (same as Figure 3-1)

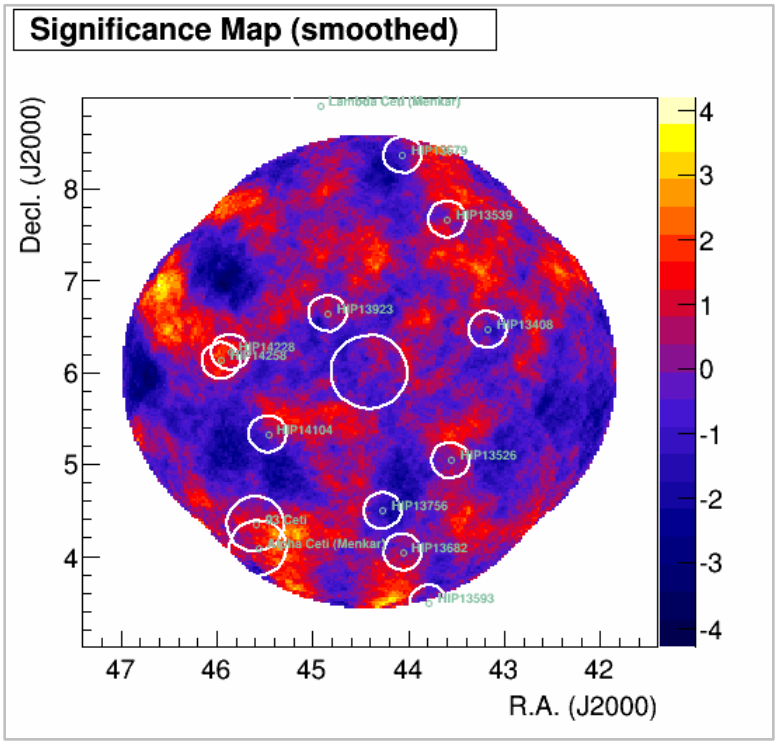

Figure 3-10: Target and Cluster: A400 (same as Figure 3-1)

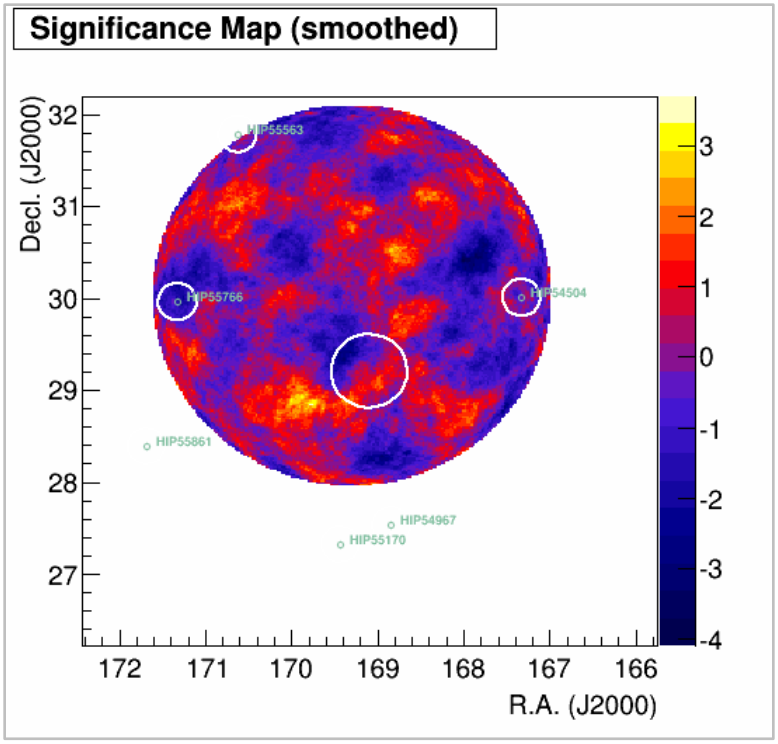

Figure 3-11: Target: GRB 080330, Cluster: A1213 (same as Figure 3-1)

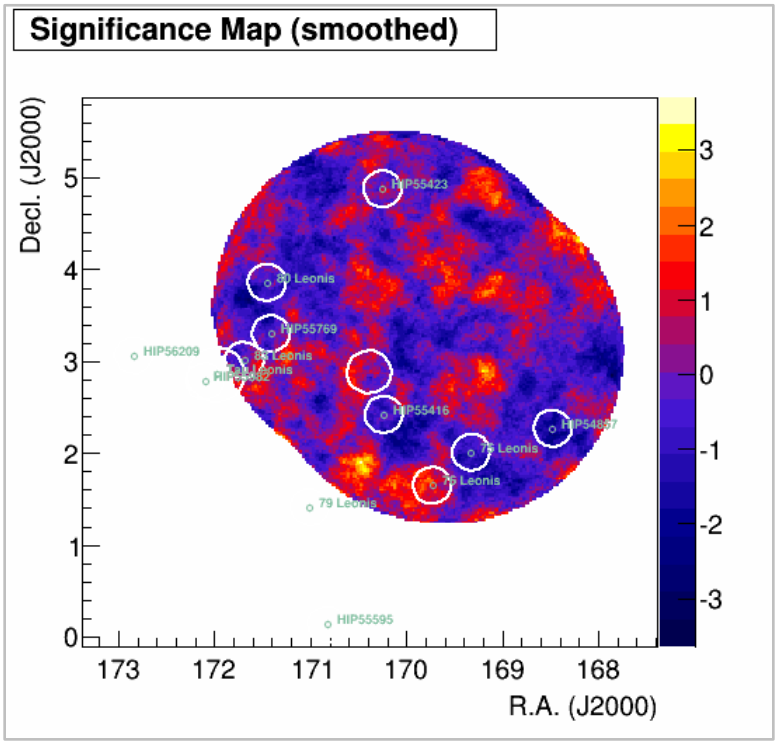

Figure 3-12: Target: GRB 100513A, Cluster: SDSS-C4-DR3 1079 (same as Figure 3-1)

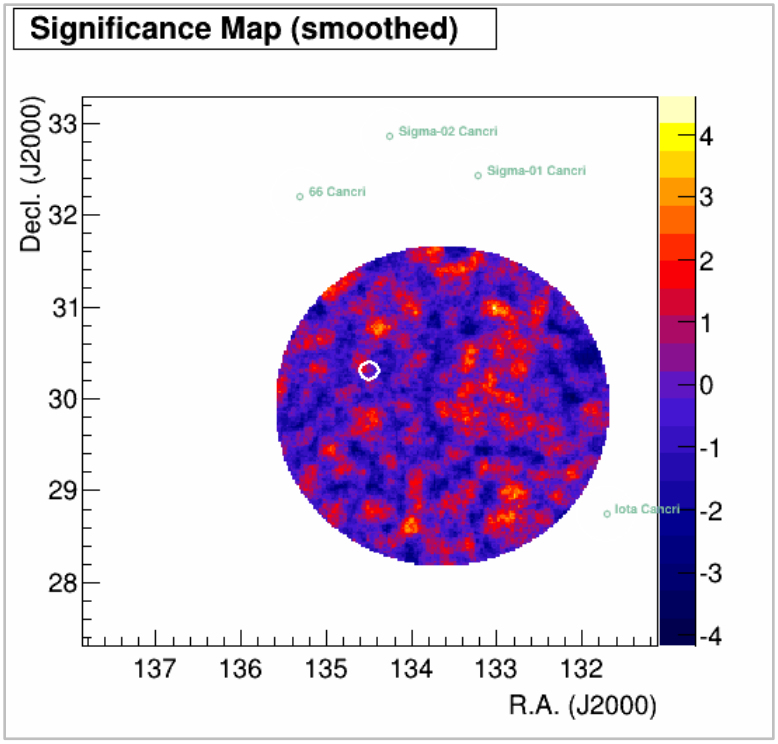

Figure 3-13: Target: LAT HIGHE 20130117, Cluster: [YSS 2008] 265 (same as Figure 3-1)

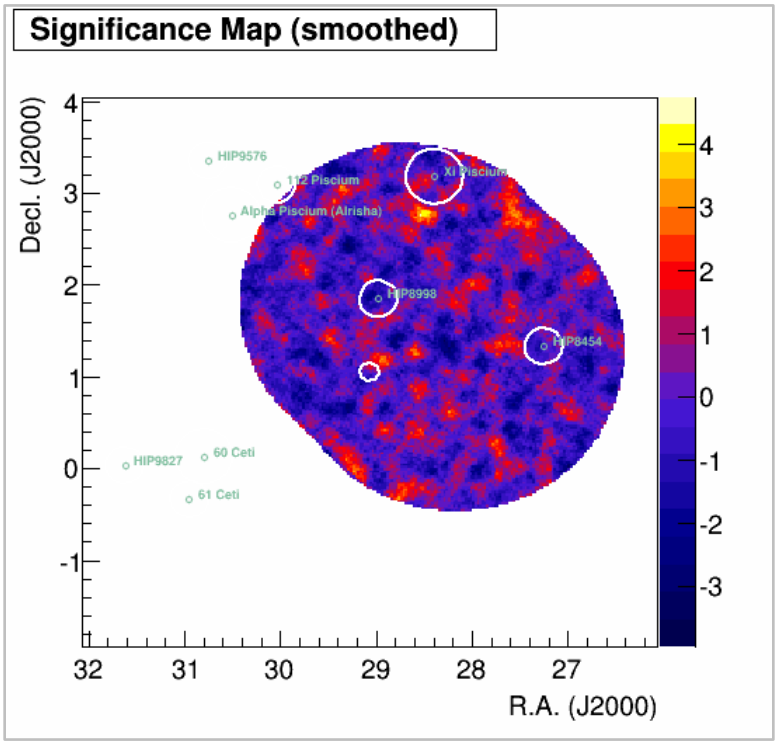

Figure 3-14: Target: RGB J0152+017, Cluster: A279 (same as Figure 3-1)

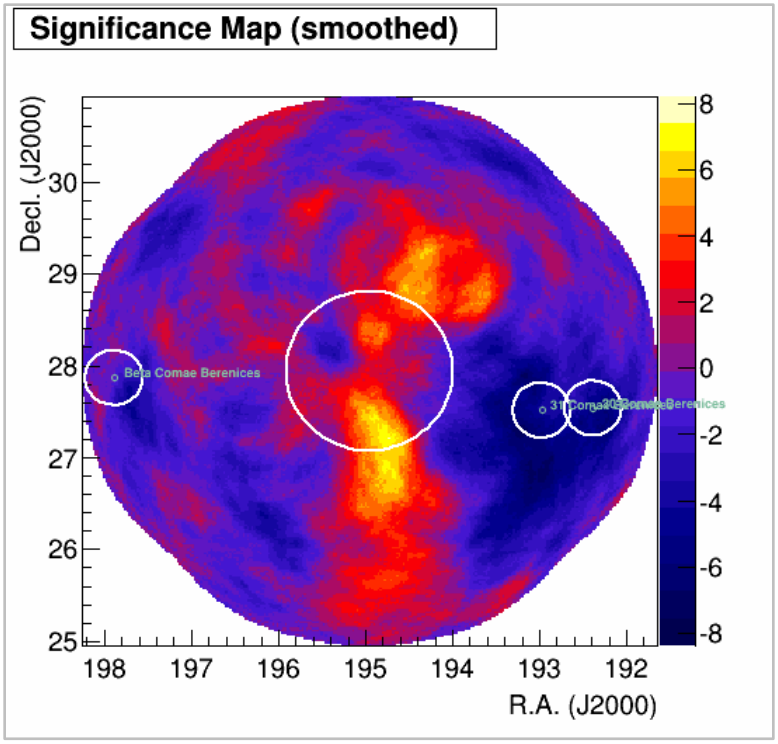

Figure 3-15: Target and Cluster: Coma cluster (same as Figure 3-1)

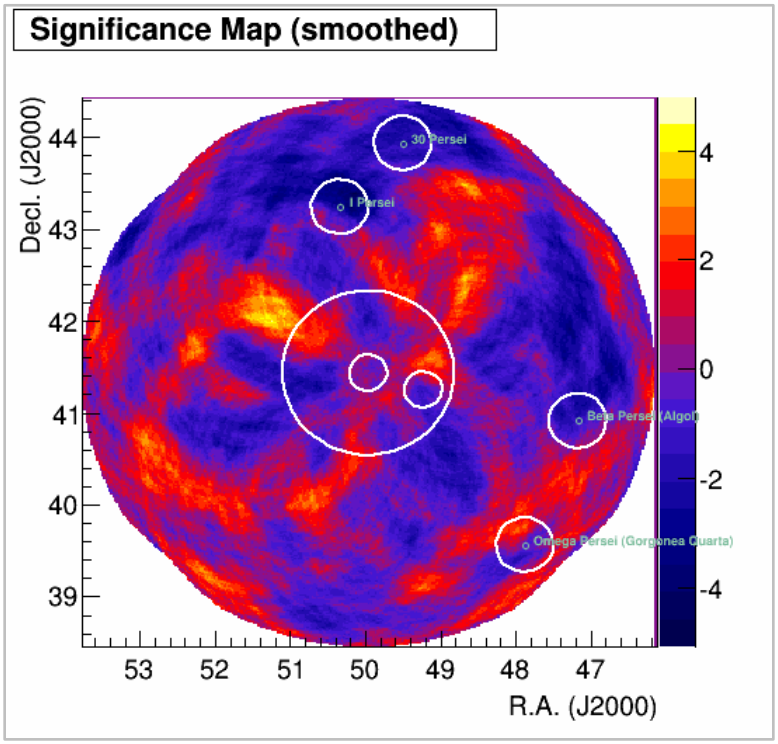

Figure 3-16: Target and Cluster: Perseus cluster (same as Figure 3-1)

Table 3-3: Average effective areas in cm^2 for the 12 galaxy clusters

Cluster Name	200 GeV	300 GeV	500 GeV	1000 GeV	2000 GeV	5000 GeV
NGC 507	3.42e8	5.37e8	8.01e8	1.13e9	1.33e9	1.42e9
NGC 1550	2.14e8	4.54e8	7.07e8	1.02e9	1.21e9	1.36e9
3C 129	2.59e8	5.11e8	6.68e8	8.62e8	1.09e9	1.32e9
UGC 9534	3.70e8	4.49e8	6.70e8	8.47e8	1.02e9	1.24e9
A2199	2.42e8	3.99e8	4.37e8	6.88e8	9.36e8	1.06e9
A400	3.98e8	9.19e8	1.25e9	1.73e9	1.99e9	2.27e9
A1213	2.72e8	4.12e8	5.63e8	7.82e8	8.50e8	1.09e9
SDSS-C4-DR3 1079	4.15e8	7.24e8	9.30e8	1.29e9	1.62e9	1.85e9
[YSS 2008] 265	3.25e8	4.35e8	5.80e8	8.40e8	9.36e8	9.36e8
A279	3.95e8	6.07e8	8.55e8	1.19e9	1.28e9	1.40e9
Coma	2.83e8	5.31e8	7.10e8	9.12e8	1.14e9	1.34e9
Perseus	3.06e8	4.08e8	5.99e8	8.45e8	1.01e9	1.27e9

Compared to the dSphs, the VERITAS data on the clusters is more widely varied. Only wobble positions passing the acceptance cut for angular distance to the cluster center were considered, so many of the skymaps do not have the characteristic 4-leaf clover FOV pattern. The clusters have a wide range of R_{500}, an effect of both cluster mass and distance. In some clusters whose centers have a large angular offset from the tracking center, the inner and outer radii of the background ring in RBM were adjusted to not exceed the edge of the camera image.

Anytime VERITAS receives word of a γ-ray burst (GRB) above the horizon, the observing crew will interrupt the run in progress and slew to the coordinates given by the burst monitor software. The error circle on the burst position from Fermi or the SWIFT satellite is usually quite large, on the order of 10 degrees, so it is rare that the burst ends up falling within the VERITAS FOV. The standard protocol for GRB observations dictates taking a limited number of runs at that position and checking the QuickLook software for any sign of activity. Three of the clusters fell within the FOV by chance during GRB alerts that did not warrant follow-up observations. Consequently the exposure time on those clusters is unusually brief.

The final step in this analysis will seek to combine the limits of the clusters in much the same way that the dSph paper is stacking its limits. The excess counts for each cluster from equation 2.9 are related to $\langle\sigma v\rangle$ and the J-factor by the following:

$$N_{excess,i} = J_i(\Delta\Omega)\frac{\langle\sigma v\rangle}{8\pi M_\chi^2} t_{obs} \int_{E_1}^{E_2} \frac{dN_\gamma}{dE} A_i(E) dE \qquad (3.1)$$

where t_{obs} is the exposure time and A_i is the effective area as a function of energy for cluster i. The excess counts are then converted to a 95% confidence level counts upper limit by the Rolke method [136]. By inverting the equation above and solving for $\langle\sigma v\rangle$ the exclusion plot for each cluster can be plotted for values of $M\chi$. Since the true DM cross-section and mass should not vary between clusters, a combined limit can be found by stacking the clusters' Rolke 95% confidence level counts upper limits:

$$\langle\sigma v\rangle^{95\%\,CL} = \frac{8\pi M_\chi^2}{\sum_i t_{obs,i} J_i(\Delta\Omega)} \frac{\sum_i N_\gamma^{95\%\,CL}}{\int_0^{M_\chi} \frac{dN_\gamma}{dE} A_i(E) dE} \qquad (3.2)$$

3.4 CLUMPY and PPPC4DMID

Half of the clusters used in the analysis have published J-factors [89]. Those values are given in Table 3-4. The other half are calculated with the parameters found in the two galaxy cluster surveys.

Table 3-4: Cluster J-factors within 0.1° and 0.5° integration radii (credit: E. Nezri [89])

Cluster Name	$\log_{10}[J/(\mathrm{GeV}^2\mathrm{cm}^{-5})]$ (0.1°)	$\log_{10}[J/(\mathrm{GeV}^2\mathrm{cm}^{-5})]$ (0.5°)
Perseus	17.4	18.1
Coma	17.2	17.9
3C 129	17.0	17.7
NGC 1550	17.0	17.7
A2199	17.0	17.6
A400	16.7	17.4

Nezri et al. used CLUMPY, a DM simulations software package, to calculate the above J-factors [148]. This analysis uses CLUMPY with the same input parameters given in the paper to reproduce the six J-factors above as well as for the other six clusters not listed. CLUMPY requires the following for each cluster: Galactic coordinates (l, b in degrees), distance scale (kpc and redshift z), R_{200}, scale radius, scale density, and choice of profile (Einasto or NFW). The scale radius R_s is related to the R_{200} according to $R_{200} = cR_s$ where c is the concentration parameter mentioned in Section 1.5 . The concentration–mass relationship Nezri et al. used for low-z is:

$$c_{200} = 3.93\left(\frac{M_{200}}{10^{14}h^{-1}M_{\odot}}\right)^{-0.097} \quad (best\ fit) \text{ (3.3) [149]}$$

The M_{200} mass terms they used were found in the Meta-Catalogue of X-ray detected Clusters of galaxies (MCXC) [150]. The MCXC is based off of ROSAT observations as

well. In this work, the additional M_{200} mass terms come from the two galaxy cluster surveys (HIFLUGCS and [YSS 2008]) described in Section 1.7 . Notice that the concentration parameter and, by extension, the scale density is inversely proportional to mass. The physical reasoning for this trend is that smaller haloes collapsed earlier in time when the universe was more dense. Since the J-factor is proportional to the DM density squared, the clumpy distribution of subhalos inside larger, smooth halos should increase the DM annihilation flux significantly [151]. Other necessary parameters to make CLUMPY match the Nezri et al. results are 10% of the cluster mass exists in subhaloes, subhaloes exist in the range of 10^{-6} $M_{\odot}$ to 10^{-2} of the total cluster mass, the number distribution of subhaloes follows a power law in mass with index of 1.9, and the spatial distribution of the subhaloes matches the smooth, whole-cluster profile. CLUMPY corrects for the relative velocities of the Solar System's Galactic orbit, the motion of the DM within the cluster, and the Hubble expansion of Space itself in the J-factor calculation enabling the $<\sigma v>$ limits to be combined in the stacking method later. Figure 3-17 shows the input file used by CLUMPY to calculate the J-factors.

```
#*************************************************************************************************************#
#                  [OBJECT LOCATION AND SIZE]                |            DM DISTRIBUTION (RHO_TOT)          #
# Name           Type    long.   lat.    d      z     Rvir   |     rhos       rs     prof.   #1   #2   #3   #
#  -              -      [deg]   [deg]  [kpc]   -    [kpc]   |  [Msol/kpc3]  [kpc]  [enum]    -    -    -   #
#*************************************************************************************************************#

Perseus_MCXC      CLUSTER  150.6  -13.3  75000   0.0179 2040       398000     578    kZHAO   1.0  3.0  1.0
Coma_MCXC         CLUSTER  57.2   88.0   96200   0.0231 1790       434300     495    kZHAO   1.0  3.0  1.0
3C129_MCXC        CLUSTER  160.5  0.3    91700   0.0220 1370       509300     352    kZHAO   1.0  3.0  1.0
A2199_MCXC        CLUSTER  62.9   43.7   124000  0.0299 1580       461100     426    kZHAO   1.0  3.0  1.0
NGC1550_MCXC      CLUSTER  191.0  -31.8  55200   0.0131 980        624600     233    kZHAO   1.0  3.0  1.0
A400_MCXC         CLUSTER  170.3  -45.0  99000   0.0238 1030       614000     245    kZHAO   1.0  3.0  1.0
NGC507            CLUSTER  130.6  -29.1  70900   0.0169 1040       447700     212    kZHAO   1.0  3.0  1.0
UGC9534           CLUSTER  8.8    58.3   209000  0.0520 1220       1544000    285    kZHAO   1.0  3.0  1.0
A1213             CLUSTER  201.5  69.0   189300  0.0468 2150       422600     605    kZHAO   1.0  3.0  1.0
SDSS-C4-DR3_1079  CLUSTER  257.5  57.6   197700  0.0490 1360       613400     327    kZHAO   1.0  3.0  1.0
[YSS2008]_265     CLUSTER  194.6  39.3   327200  0.0846 910        868100     195    kZHAO   1.0  3.0  1.0
A279              CLUSTER  154.5  -57.8  307600  0.0790 950        838500     205    kZHAO   1.0  3.0  1.0
```

Figure 3-17: CLUMPY input file for the 12 clusters. The columns are: name, type, Galactic coordinates, distance in kpc and redshift, virial radius, scale density and radius, and Zhao's profile parameters (see equation 3.4)

CLUMPY returns an output ROOT graphic of the $J(\Delta\Omega)$ as a function of the integration angle. Figure 3-18 shows an example of the output. In addition it creates a text file that lists the J-factor in units of $M_{\odot}^{2}\text{kpc}^{-5}$ by integration radius.

The same six clusters in Table 3-4 were checked independently with CLUMPY for consistency. Those results are given in Table 3-5 below:

Table 3-5: Calculated cluster J-factors within 0.1° and 0.5° integration radii

Cluster Name	$\log_{10}[J/(\text{GeV}^2\text{cm}^{-5})]$ (0.1°)	$\log_{10}[J/(\text{GeV}^2\text{cm}^{-5})]$ (0.5°)
Perseus	17.28	18.04
Coma	17.12	17.82
3C 129	16.98	17.62
NGC 1550	16.94	17.57
A2199	16.98	17.65
A400	16.76	17.32

As the J-factor results in Tables 3-4 and 3-5 match closely, CLUMPY was then used to calculate the J-factors for all 12 clusters in the sample within their respective R_{500} radii. Those values are presented in Table 3-6.

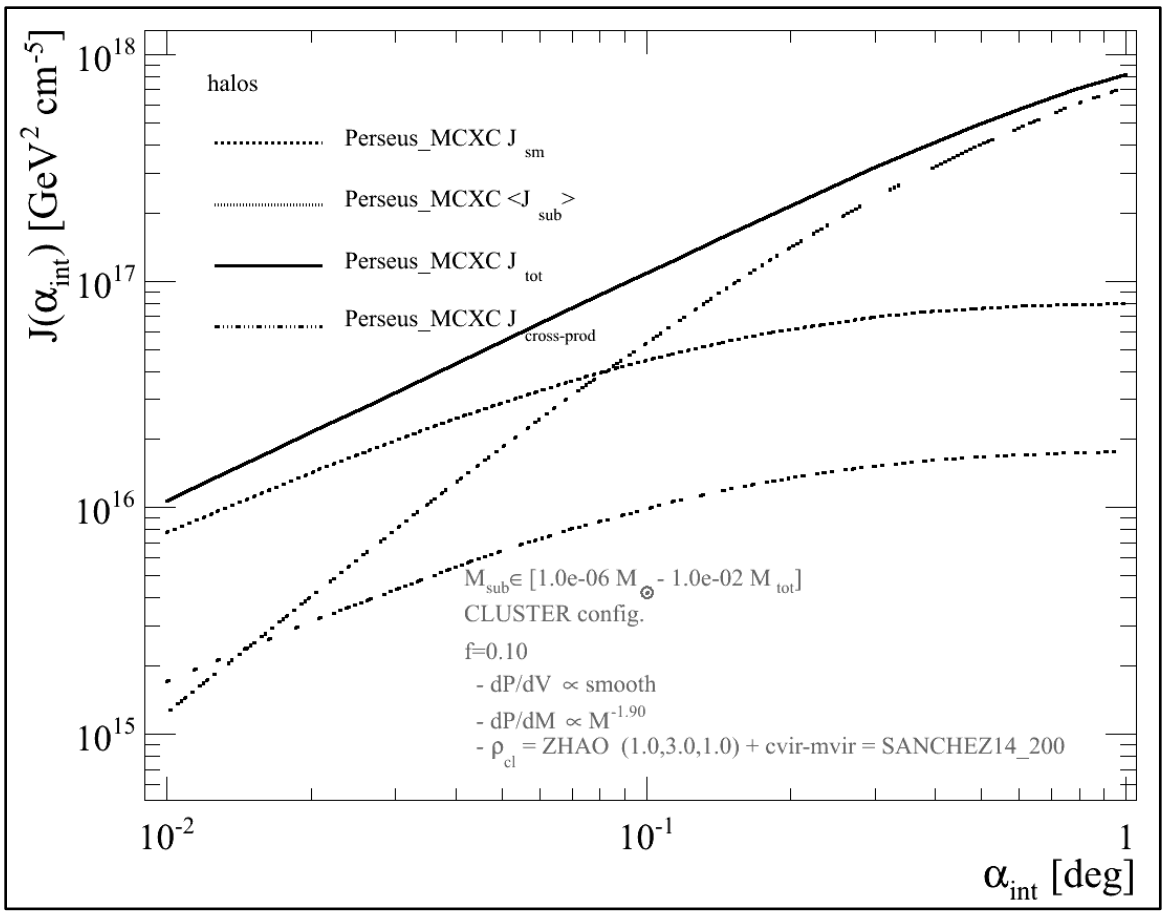

Figure 3-18: A plot of $J(\Delta\Omega)$ for the Perseus cluster produced by CLUMPY. The four lines in the plot above represent the contributions from different components to the J-factor. J_{sm} is the smooth halo model, in this case Zhao's profile [152]:

$$\rho^{ZHAO}(r) = \frac{\rho_s}{\left(\frac{r}{R_s}\right)^{\gamma} \cdot \left[1 + \left(\frac{r}{R_s}\right)^{\alpha}\right]^{\frac{(\beta-\gamma)}{\alpha}}} \quad (3.4)$$

For the choice of $(\alpha, \beta, \gamma) = (1,3,1)$, Zhao's profile becomes the NFW profile. $<J_{sub}>$ represents the J-factor stemming from the simulated subhaloes that are also modeled with an NFW profile. $J_{cross\text{-}prod}$ is a second-order term that appears when convolving the smooth halo with the subhaloes. Those three terms combined give the total J-factor J_{tot}.

Table 3-6: Calculated J-factors within R_{500} from a progression of CLUMPY versions. The notation 'v1.4' in the table refers to CLUMPY Version_2011.09_corr4, the version used to cross-check the Nezri et al. paper results in Table 3-4. A new version, CLUMPY Version_2015.06 or 'v2.0', was released mid-2015 that included updated cosmological parameters (from WMAP to Planck values), galactic DM profile parameters, and concentration–mass relationship as default [153]. To ensure consistency between v1.4 and v2.0, the v2.0 configuration file was modified to reflect the v1.4 parameter choices and labeled 'v2.0 old.' The same calculations were performed with the default (updated) v2.0 configuration file labeled 'v2.0 new.' The values in parentheses are the relative change in dex of the corresponding cluster J-factor between the two v2.0 columns.

Cluster Name	$\log_{10}[J/(\mathrm{GeV}^2\mathrm{cm}^{-5})]$ (R_{500}) **v1.4**	$\log_{10}[J/(\mathrm{GeV}^2\mathrm{cm}^{-5})]$ (R_{500}) **v2.0 old**	$\log_{10}[J/(\mathrm{GeV}^2\mathrm{cm}^{-5})]$ (R_{500}) **v2.0 new**
Perseus	18.26	18.26	17.89 (–0.37)
Coma	17.98	17.99	17.61 (–0.38)
NGC 507	17.20	17.21	16.82 (–0.39)
NGC 1550	17.48	17.50	17.12 (–0.38)
3C 129	17.71	17.72	17.34 (–0.38)
A2199	17.55	17.56	17.18 (–0.38)
UGC 9534	17.19	17.20	16.89 (–0.31)
A400	17.27	17.27	16.89 (–0.38)
A1213	17.52	17.52	17.17 (–0.35)
SDSS-C4-DR3 1079	16.95	16.96	16.60 (–0.36)
[YSS 2008] 265	16.07	16.06	15.73 (–0.33)
A279	16.15	16.16	15.82 (–0.34)

Table 3-7 compares the two configuration file parameters used.

Table 3-7: The configuration file parameters for the two versions of CLUMPY. The difference in cosmological parameters corresponds to the WMAP values being updated by the recent Planck results. The difference in galactic DM profile parameters and the local DM density corresponds to newer precision measurements of nearby stars' orbital velocities. The change to the number of subhaloes and concentration-mass relationship reflects recent improvements to the N-body simulations that predict the clusters' DM content.

Value	**v1.4/v2.0 old**	**v2.0 new**
Hubble constant	70 $kms^{-1}Mpc^{-1}$	68 $kms^{-1}Mpc^{-1}$
ρ_c (z = 0)	144 $M_\odot kpc^{-3}$	128 $M_\odot kpc^{-3}$
Ω_{matter} (visible + DM)	0.26	0.308
$\Omega_{dark\ energy}$	0.74	0.692
Galactic DM profile	NFW	Einasto
Galactic R_s	21.7 kpc	15.14 kpc
Galactic R_{200}	280 kpc	260 kpc
DM density at Earth	0.3 $GeVcm^{-3}$	0.4 $GeVcm^{-3}$
# of subhaloes	100	150
Concentration-mass relationship	Bullock et al. 2001 [151]	Sánchez-Conde & Prada 2014 [154]

The change to the updated configuration had the overall effect of reducing the J-factors. Several trials were performed modifying the cosmological parameters, galactic DM profile parameters, and concentration–mass relationship from the v1.4 to the v2.0 defaults independently. On average, the cosmological parameters and galactic DM profile parameters lowered the J-factor by ~0.1 dex each. The largest shift occurred when switching between the concentration–mass relationships, a difference of 0.1 – 0.2 dex.

A Poor Particle Physicist's Cookbook for Dark Matter Indirect Detection (PPPC4DMID) is a website maintained by Marco Cirelli and whose 'Fluxes at Production' tables are used by CLUMPY to estimate the γ-ray flux from annihilating DM through various decay channels [155] [156] [157]. There are separate tables for each type of long-lived Standard Model particle ($e^+, \bar{p}, \gamma, \nu_l$, etc.) that can be detected by current experiments. The final-state γ-rays table is appropriate for VERITAS DM searches. The table provides the spectrum $dN_\gamma/d(log_{10}\, x)$ of γ-rays, normalized per one annihilation. The variable *x* represents the energy fraction given by:

$$x = \frac{KE}{M_\chi} \quad (3.5)$$

where *KE* is the kinetic energy of the final-state particles in the rest frame. The columns in the table are $M\chi$, $\log_{10} x$, and $dN_\gamma/d(log_{10}\, x)$ for 28 primary channels. The DM masses modeled in the table range from 5 GeV to 100 TeV and the range for $\log_{10} x$ runs from -9 to 0. For example, the table gives the expected γ-ray flux for the choice of $\chi + \chi \rightarrow b + \bar{b}$, $\chi + \chi \rightarrow W^+ + W^-$, or $\chi + \chi \rightarrow \tau^+ + \tau^-$channels. The units on *x* are dimensionless so converting from $dN_\gamma(x)/d(log_{10}\, x)$ to $dN_\gamma(E)/d(log_{10}\, E)$ is a straight substitution for the integral term in equation 1.8 . The PPPC4DMID paper claims good agreement between the table values and those generated by the DM annihilation software packages PYTHIA and HERWIG [143] [158].

The latest version of the tables incorporates electroweak corrections for left- and right-handed leptons as well as transverse- and longitudinal-wave vector gauge bosons. Inclusion of these states significantly impacts the spectra of particles when the WIMP mass is above 246 GeV (the electroweak scale). In this regime soft electroweak gauge bosons are abundantly produced, thereby adding additional channels to the final states which would otherwise have been inaccessible had the corrections not been taken into account.

In addition to the quark, heavy lepton, and vector gauge boson final states the tables include the $\chi + \chi \rightarrow \gamma + \gamma$ final state. This is a non-standard annihilation channel

for most models of DM. There is no way to construct a tree-level Feynman diagram of this since DM is electrically neutral. A secondary loop of charged particles, whether Standard Model or Supersymmetric, can account for the coupling to two γ-rays (i.e., a box diagram). Here Cirelli et al. adopt an agnostic or model-independent point of view. They argue from a theoretical perspective any model of DM is as valid as any other, so all channels should be considered equally. They add that these calculations concern γ-rays only from the annihilation event, not from secondary pion decays or other radiative processes like synchrotron radiation or IC scattering. Computing a more complex, 3-body final state would require a choice of DM model that the authors refrain from.

Table 3-8: Relevant values from the "Fluxes at Production" table (credit: [157]). Each entry assumes $x = 0$ in keeping with other VERITAS DM annihilation searches.

Channel	200 GeV	300 GeV	500 GeV	1000 GeV	2000 GeV	5000 GeV
γ-rays	139.54	139.54	139.55	139.56	139.55	139.55
Tau Leptons	0.0516	0.0558	0.061	0.0688	0.0759	0.085
B Quarks	0.00204	0.00219	0.00247	0.00295	0.00327	0.00351
W Bosons	0.00133	0.00171	0.00192	0.00204	0.00206	0.00206

The new version of CLUMPY displays a great deal of functionality once the configuration file parameters are loaded. It allows the user to solve for the integrated γ-ray flux for a galaxy cluster (of calculated J-factor) from DM annihilation going into a choice of primary channel over the energy range $[E_{min}, M_\chi]$. The software also lets one choose the effective velocity-weighted cross-section $\langle\sigma v\rangle$ or boost factor B_0 (i.e., $\langle \sigma v \rangle_{eff} = B_0(3 \times 10^{-26}) \frac{cm^3}{sec}$) for the simulations. This method can also be used in reverse: if an integrated γ-ray flux of a cluster is known then work backwards with choices of M_χ and $\langle\sigma v\rangle$ till the fluxes agree.

3.5 KASCADE Lookup Tables and Effective Areas

The Kertzman and Sembroski Cherenkov Airshower and Detector Emulation (KASCADE) is the simulations code used to produce the lookup table and effective area files used in this analysis [159]. Mary Kertzman of DePauw and Glenn Sembroski of Purdue began the project in 1989 to model the EASs of γ-rays and cosmic-rays along with the response of the mirrors, PMTs, and back-end electronics of the Haleakala Gamma Ray Observatory located on Maui, Hawaii [160]. KASCADE has since then been upgraded to work with VERITAS and is a viable alternative to the CORSIKA/GrISUDet software package for VEGAS and EventDisplay analyses [161]. The secondary analysis by the collaborator at the University of Delaware uses the CORSIKA/GrISUDet lookup tables and effective areas to compare the results. Figures 3-19 and 3-20 below exhibit the performance of KASCADE versus CORSIKA/GrISUDet across Hillas parameters as well as effective area.

As mentioned in Section 2.6.3, KASCADE simulates showers over a wide parameter space from 20 GeV to >50 TeV in equal width $\log_{10} E$ bins. The number of showers per bin follows a power law with index $p \sim 2$ to simulate the measured γ-ray/cosmic-ray combined spectrum as well as save on computing time. To generate the EAS of a 50 TeV primary takes much more processing power than that of a 20 GeV primary due to the larger number of secondary particles and electromagnetic subshowers generating the Cherenkov photons. The lookup tables used for the galaxy clusters were generated by the script ‘VAAuto.scr’ with the appropriate choice of:

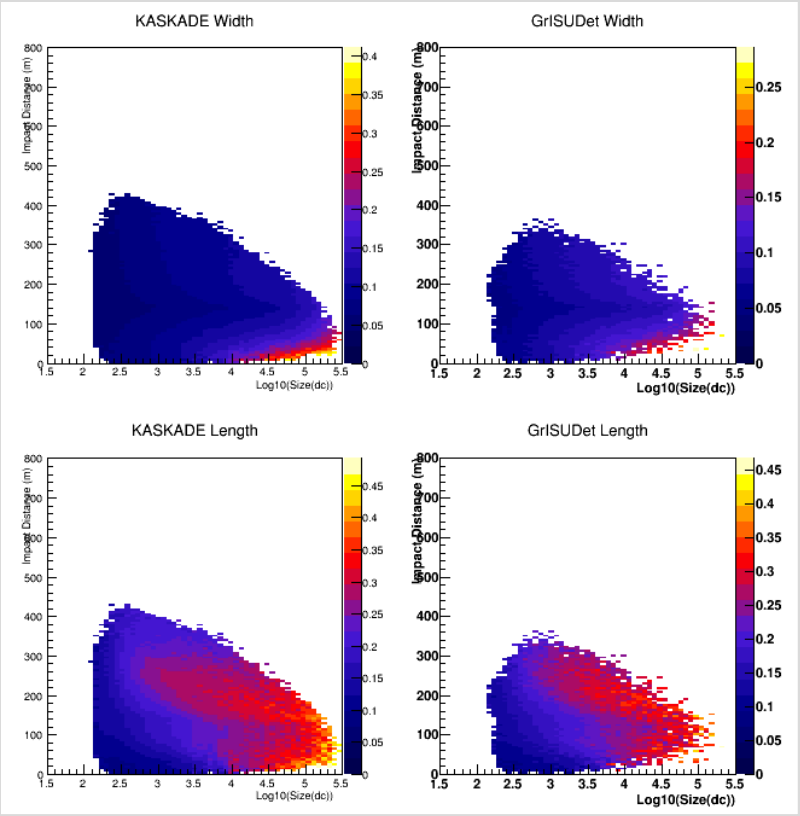

Figure 3-19: Comparison of the width and length parameters between KASCADE and CORSIKA/GrISUDet (credit: Glenn Sembroski [125]). The x-axis is the logarithm (base 10) of the image size in digital counts (proportional to the number of photoelectrons) and the y-axis is impact parameter in meters.

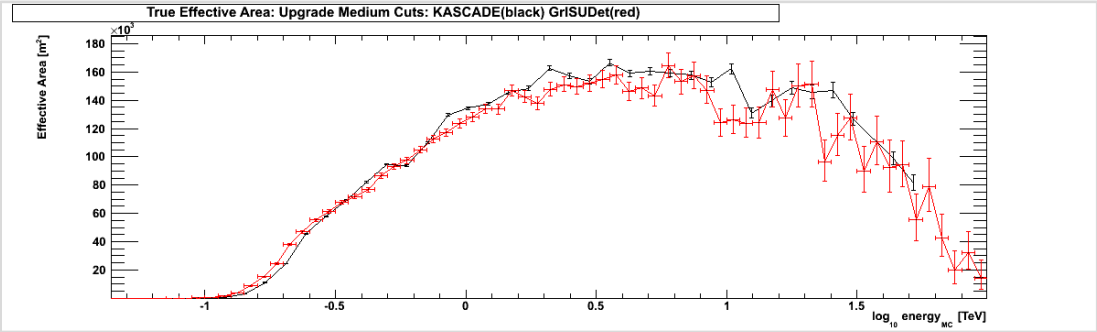

Figure 3-20: Comparison of the true effective area of VERITAS with KASCADE and CORSIKA/GrISUDet (credit: Glenn Sembroski [125]). The x-axis is the logarithm (base 10) of the simulated energy in TeV and the y-axis is the effective area of the array in square meters. The KASCADE curve is in black and the CORSIKA/GrISUDet curve is in red.

- Season: Winter or Summer
- Array type: Old, New, or Upgrade
- Particle type: γ-ray, Proton, ^{4}He nucleus, Cosmic-ray nucleus (up to Fe), or Electron
- 8 zenith angles: 1, 10, 20, 30, 40, 50, 60, and 70°
- 8 azimuth angles: 0, 45, 90, 135, 180, 225, 270, and 315°
- 9 wobble offsets: 0, 0.25, 0.5, 0.75, 1.0, 1.25, 1.5, 1.75, and 2.0°
- CFD trigger threshold setting: 45 mV or 50 mV
- 9 pedvar values: 4.73, 5.55, 6.51, 7.64, 8.97, 10.52, 12.35, 14.49, and 17.00
- Quality (size) cuts level: Loose, Soft, Medium, or Hard
- Telescope participation: Any combination of T1, T2, T3, and T4

For each shower that KASCADE produces, the temporal and spatial components of the Chernekov light distribution at ground level are logged as well. KASCADE then projects copies of the telescope array's dimensions onto a virtual grid of the ground plane to model the various views of the shower that each of the four cameras would see at a range of impact distances and sky coordinates. KASCADE uses a model of the single-photoelectron PMT response function coupled with the L1 CFD trigger threshold setting as predictors for whether a camera will register the shower. Regarding the OSS, KASCADE takes into account the time dispersion the shape of the mirrors adds to the Cherenkov wavefront as well as the hysteresis curve of the PSF due to the flex of the mirrors. KASCADE simulates the pedvar levels by adding random, isotropic photons as night-sky background on top of the Cherenkov photon signal.

The effective area files are then generated from the lookup tables with the addition of the shower cuts mentioned in Section 2.6.4 . We participated in the production and testing of the current version of the post-2012 PMT Upgrade array lookup tables and effective areas.

CHAPTER 4. RESULTS AND DISCUSSION

4.1 Results

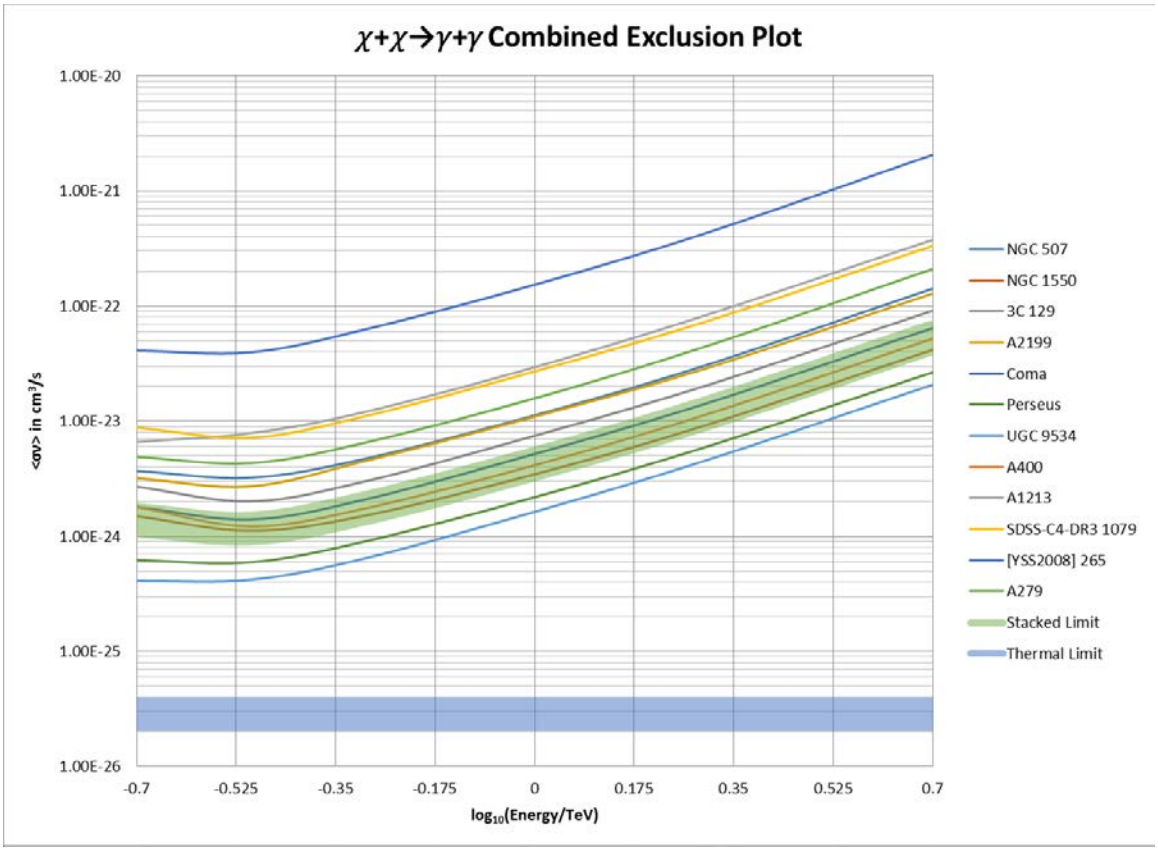

Figure 4-1: $\chi + \chi \rightarrow \gamma + \gamma$ combined exclusion plot. The stacked method and thermal limits are shown shaded with ± 1σ error bars. The energy range for $M\chi$ is 200 GeV to 5 TeV.

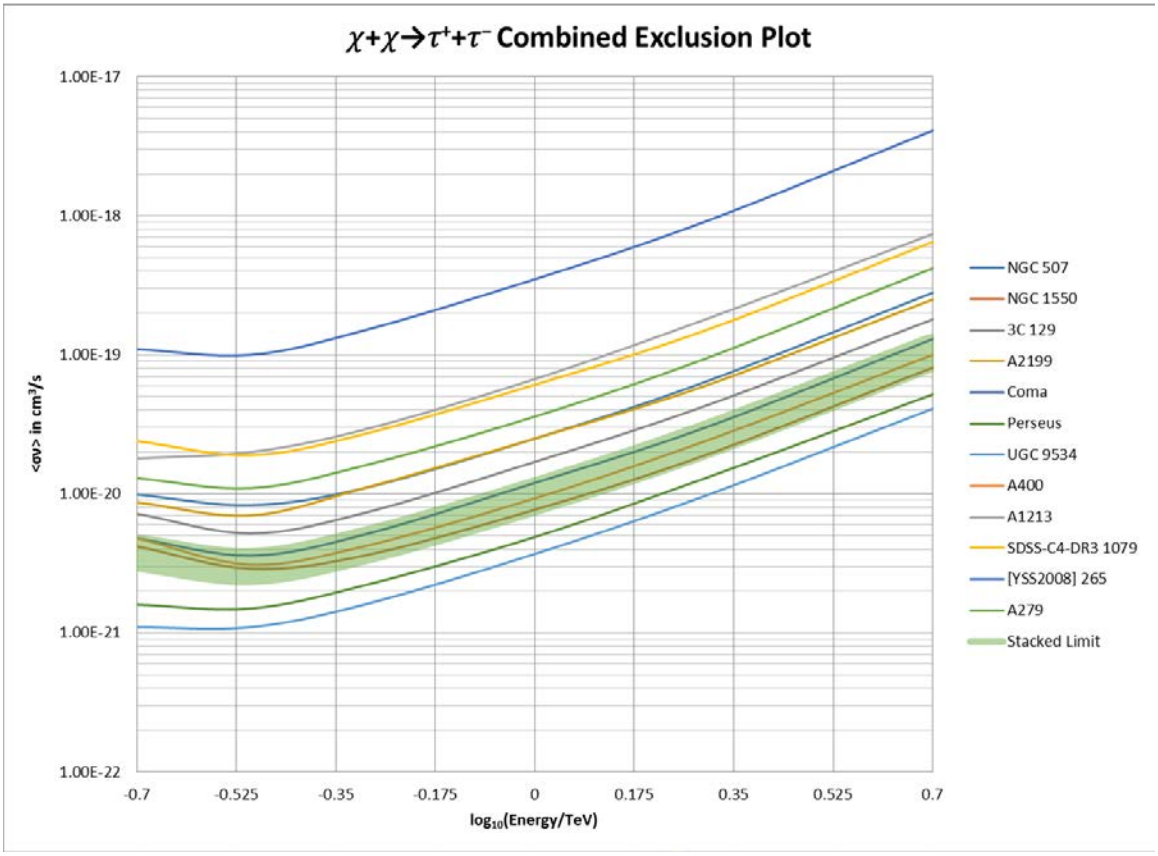

Figure 4-2: $\chi + \chi \rightarrow \tau^{+} + \tau^{-}$combined exclusion plot

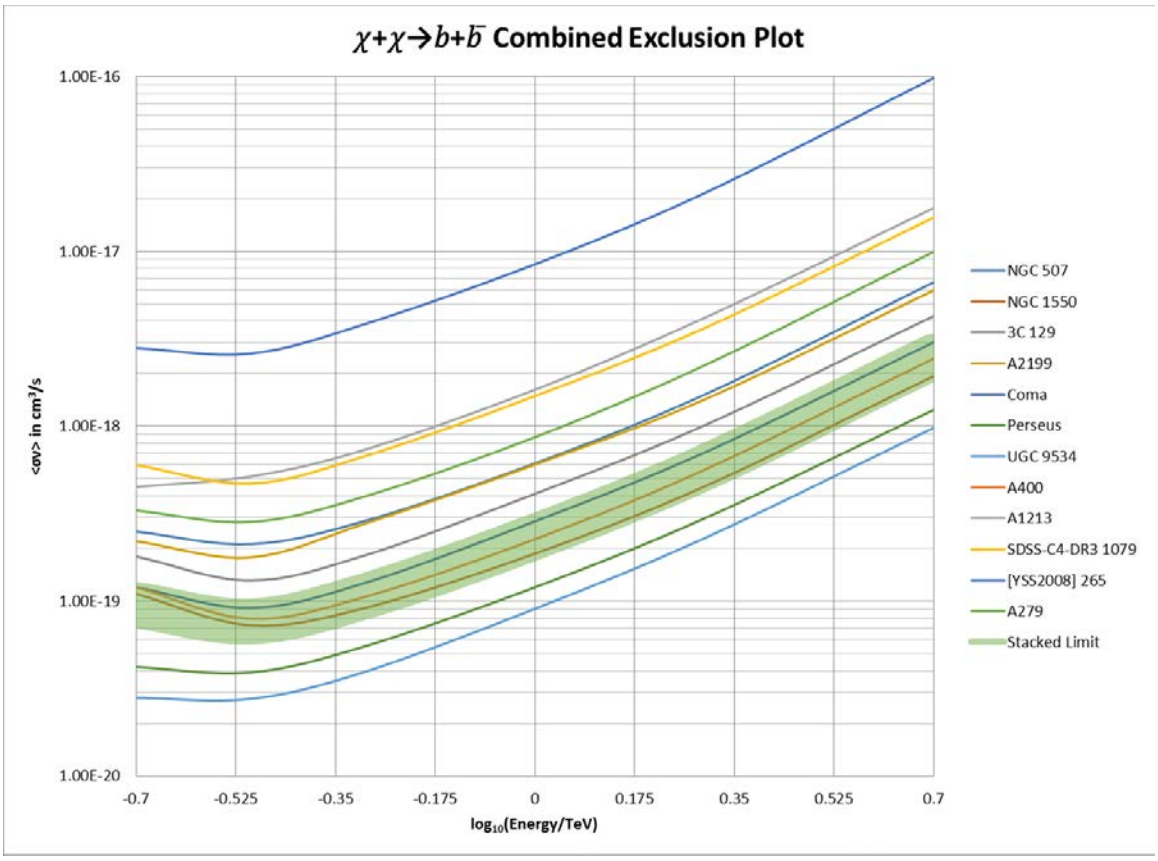

Figure 4-3: $\chi + \chi \rightarrow b + \bar{b}$ combined exclusion plot

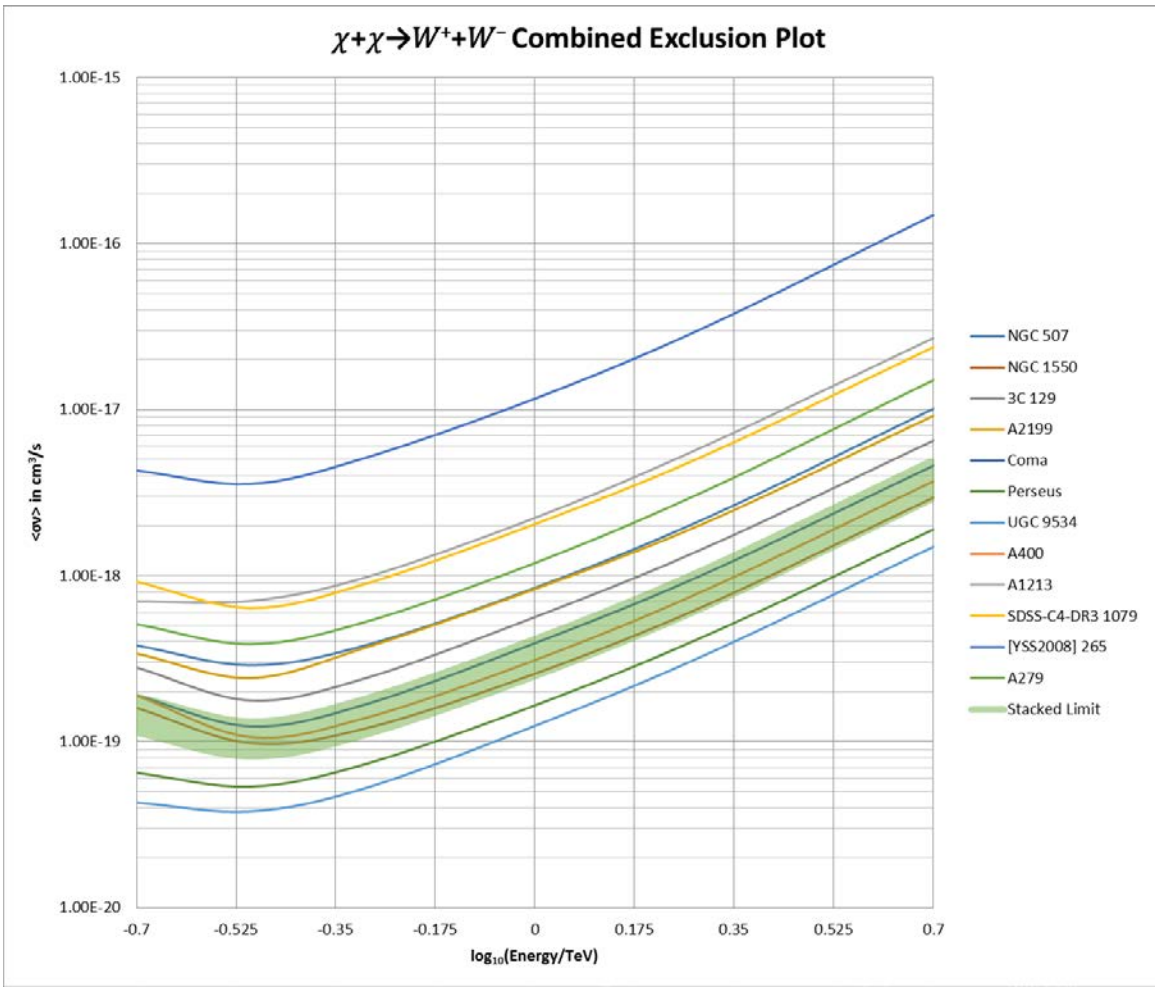

Figure 4-4: $\chi + \chi \rightarrow W^+ + W^-$ combined exclusion plot

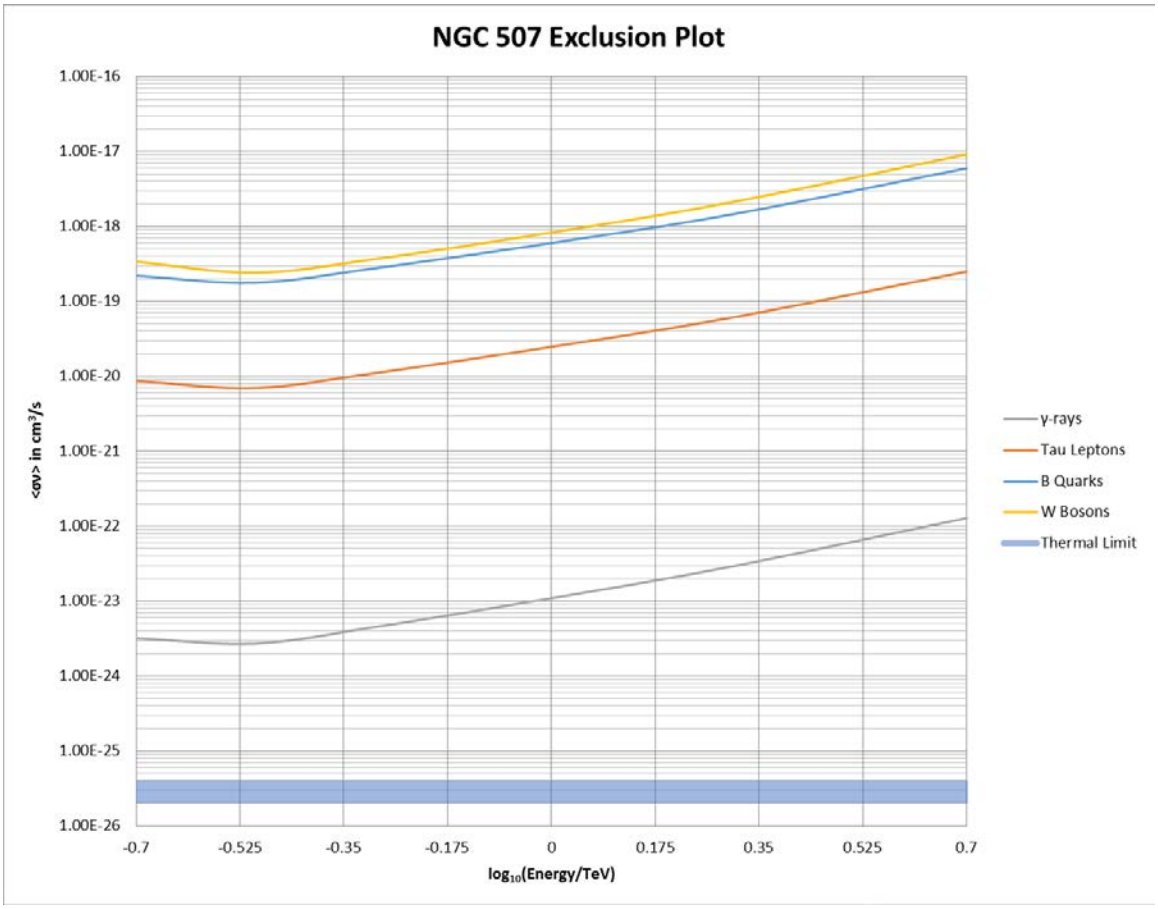

Figure 4-5: NGC 507 exclusion plot

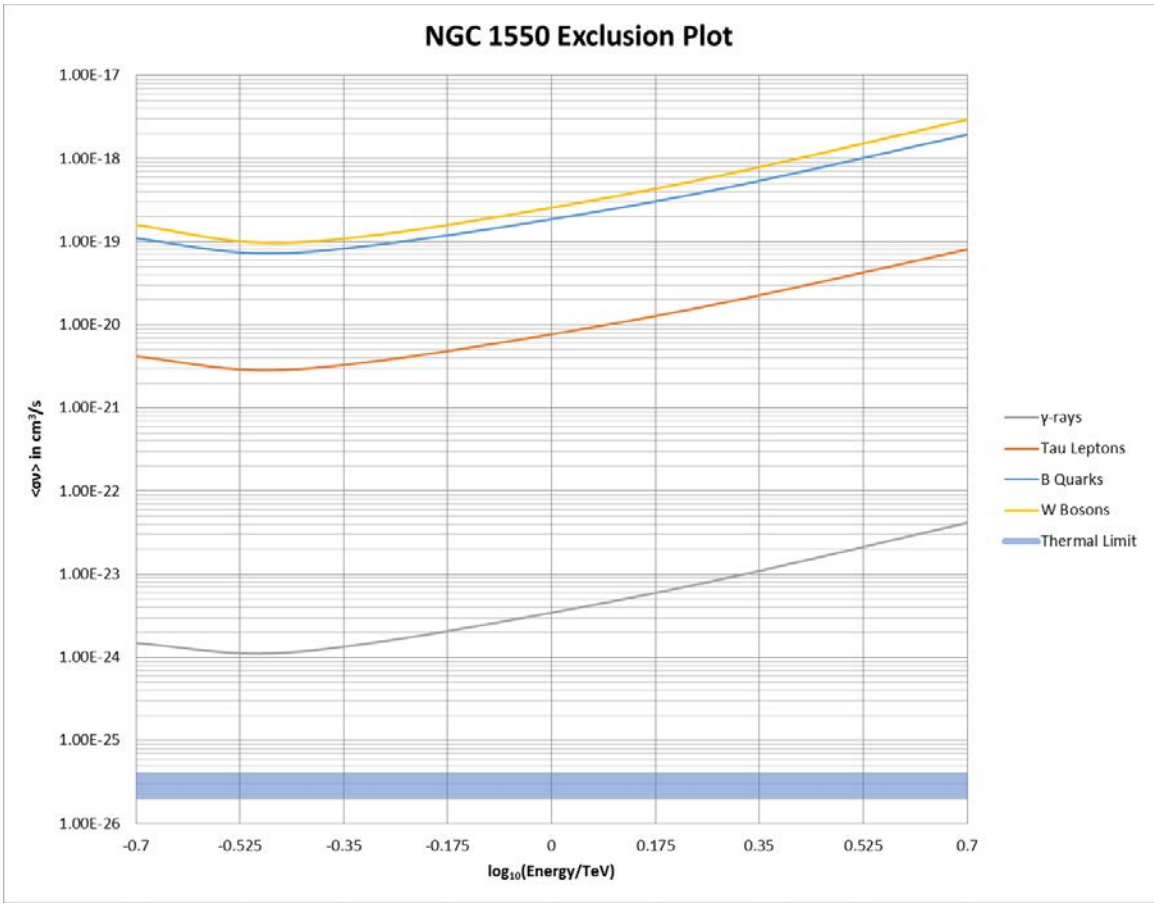

Figure 4-6: NGC 1550 exclusion plot

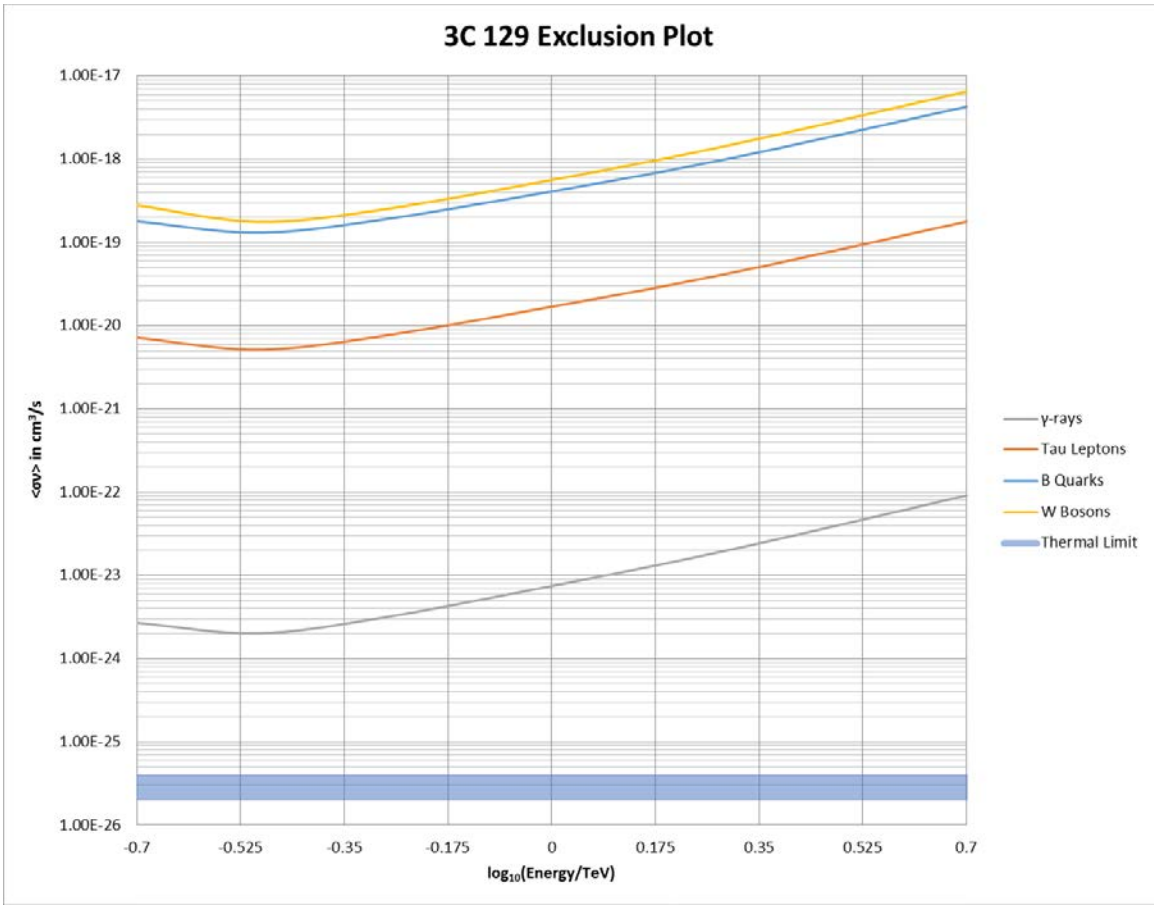

Figure 4-7: 3C 129 exclusion plot

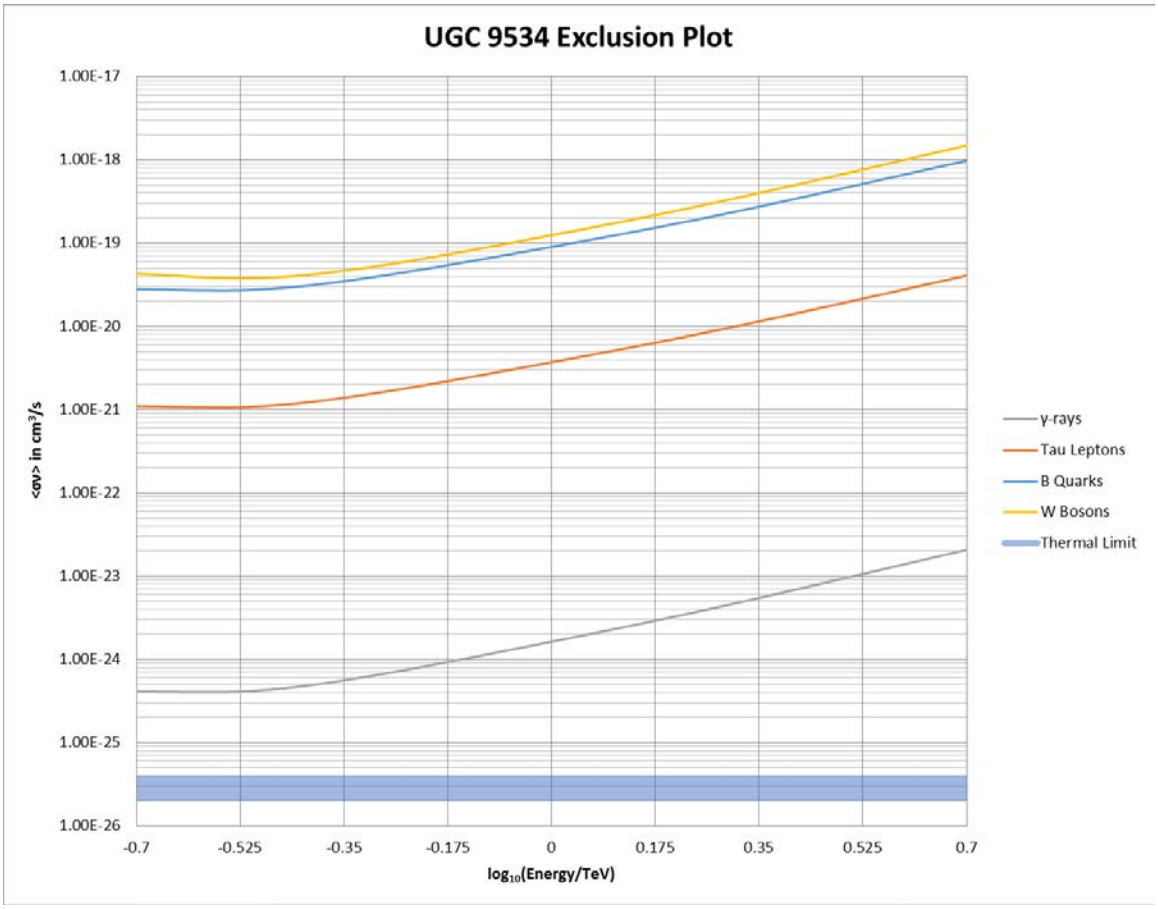

Figure 4-8: UGC 9534 exclusion plot

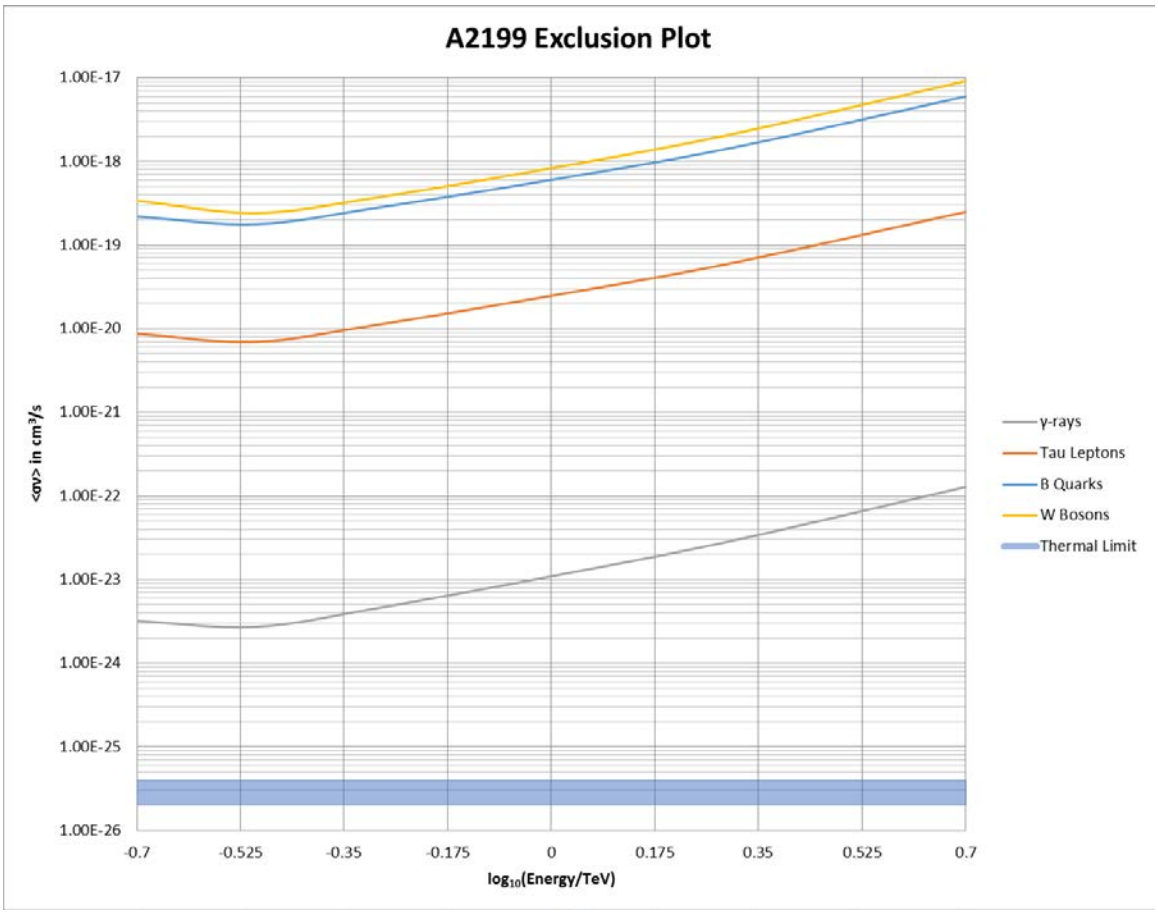

Figure 4-9: A2199 exclusion plot

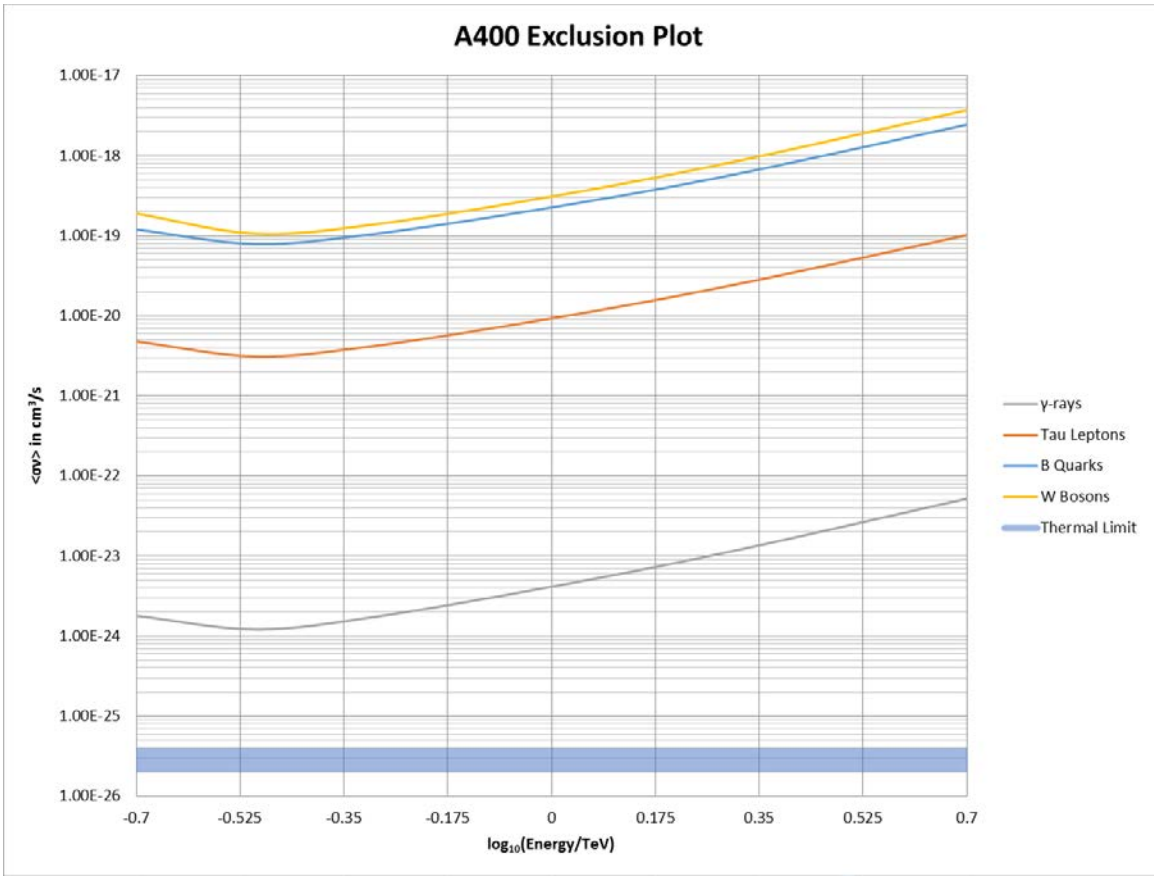

Figure 4-10: A400 exclusion plot

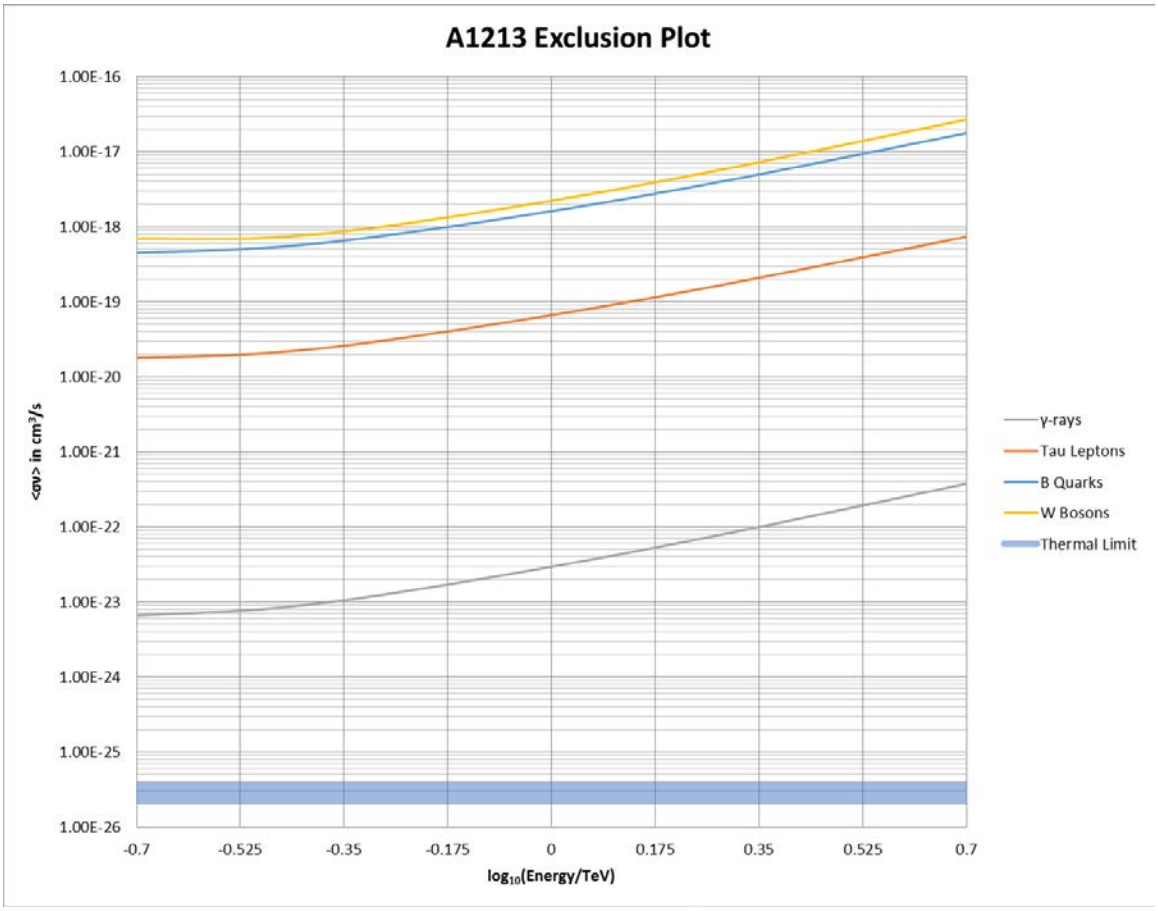

Figure 4-11: A1213 exclusion plot

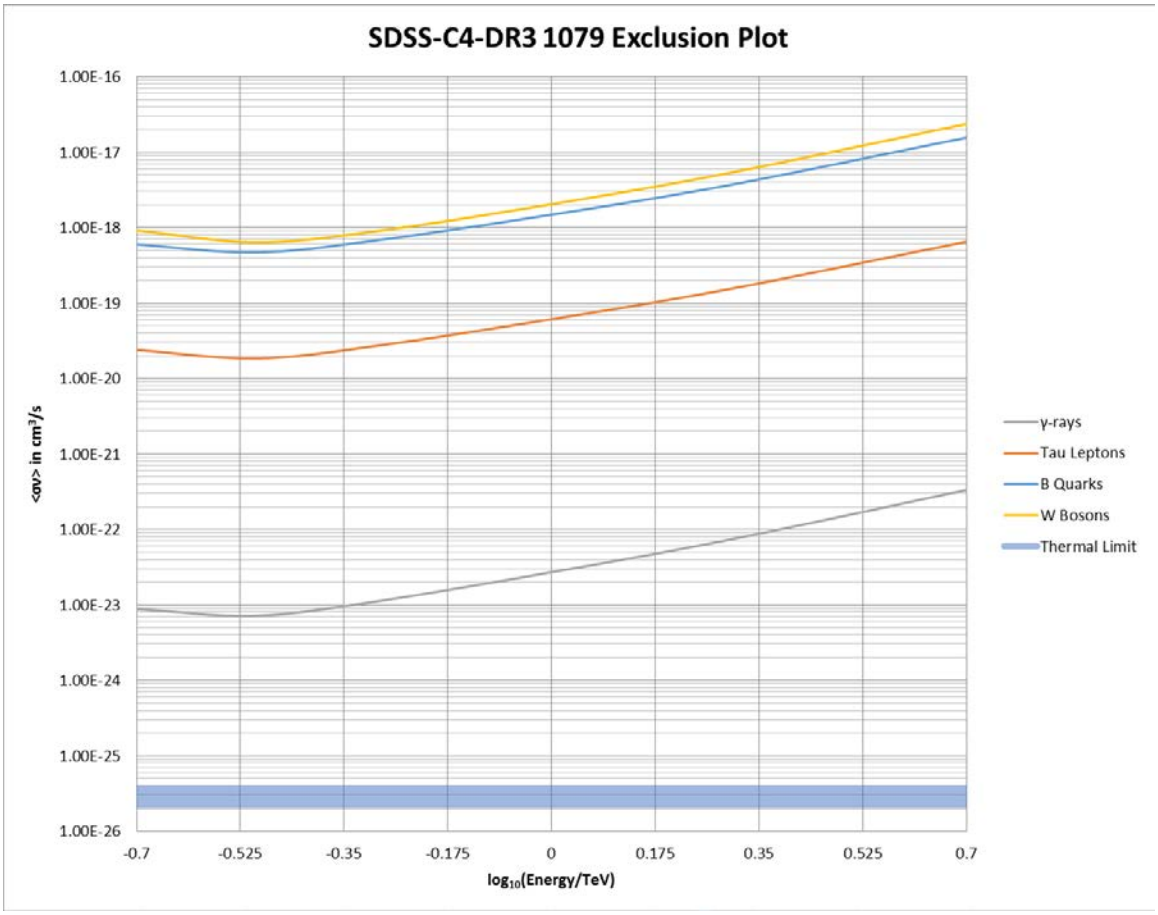

Figure 4-12: SDSS-C4-DR3 1079 exclusion plot

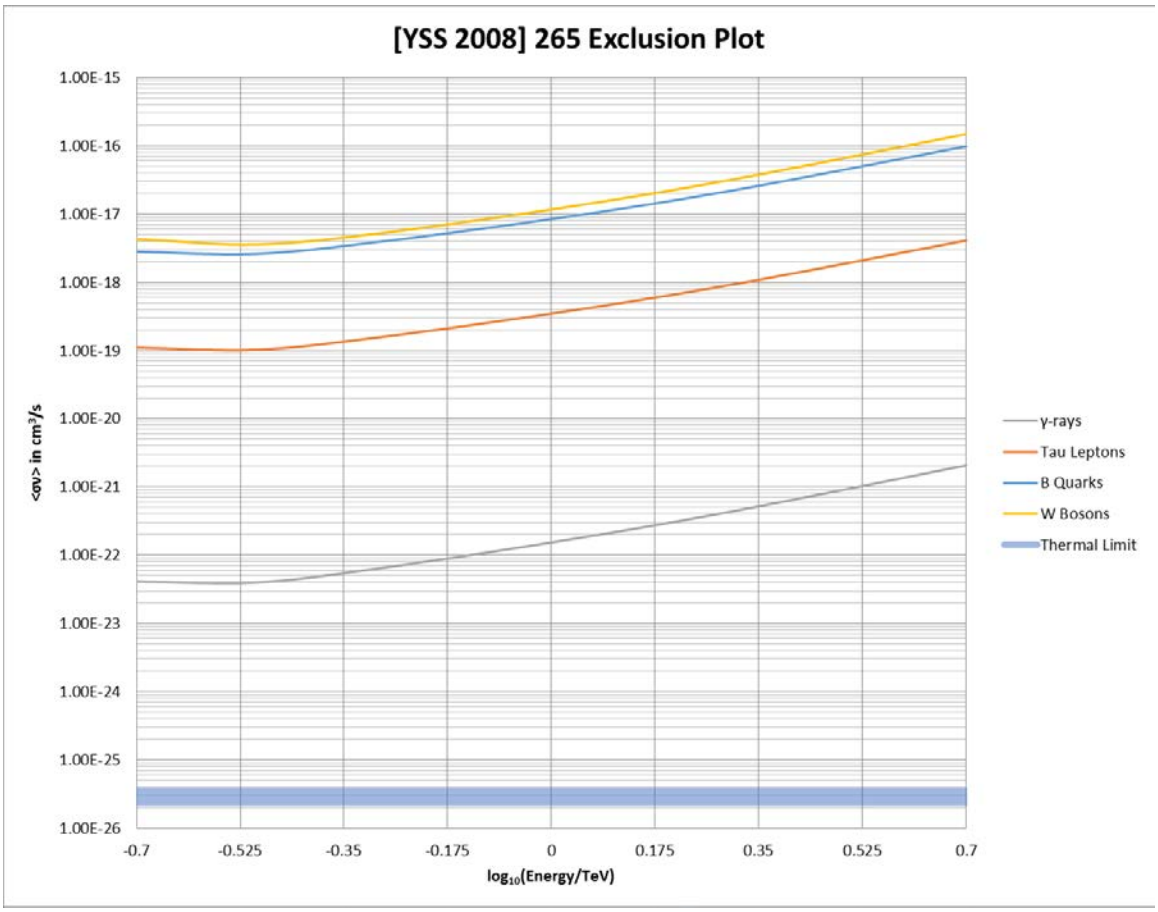

Figure 4-13: [YSS 2008] 265 exclusion plot

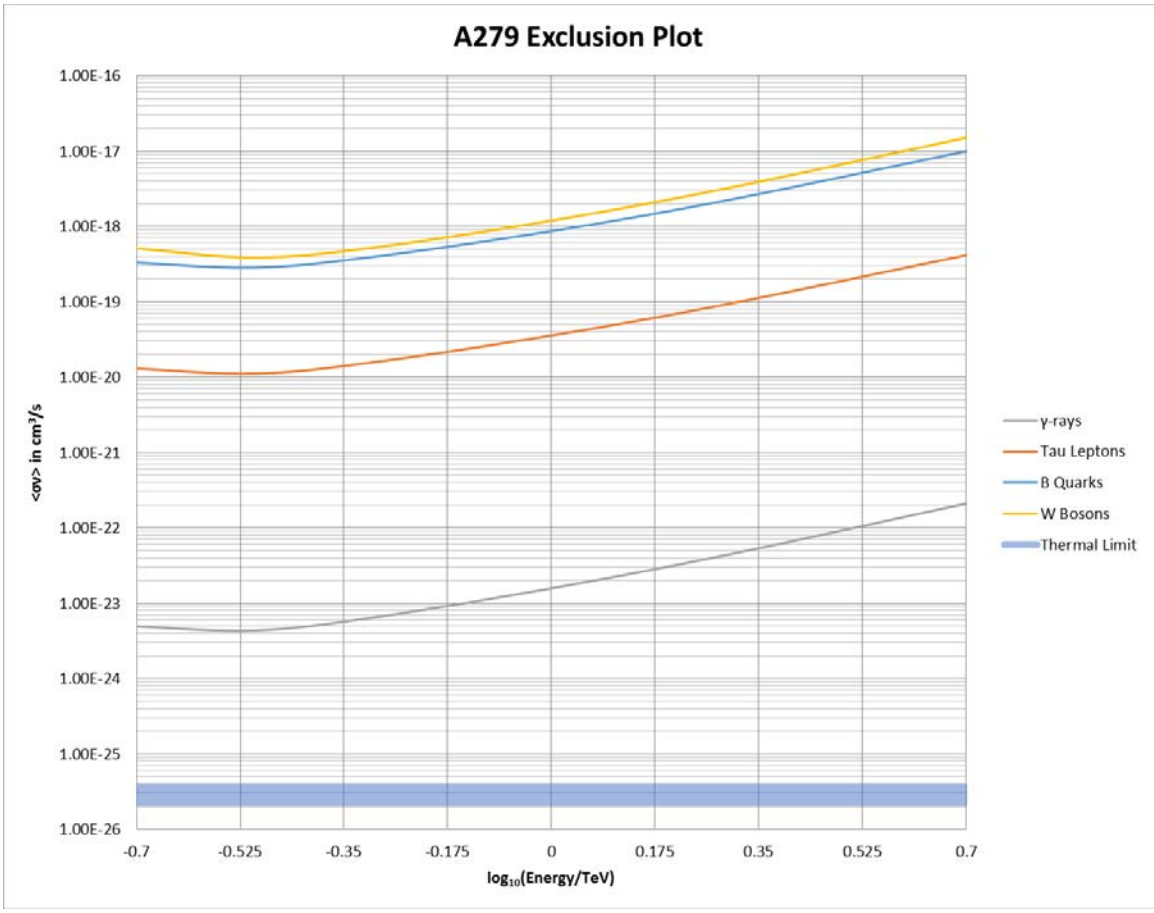

Figure 4-14: A279 exclusion plot

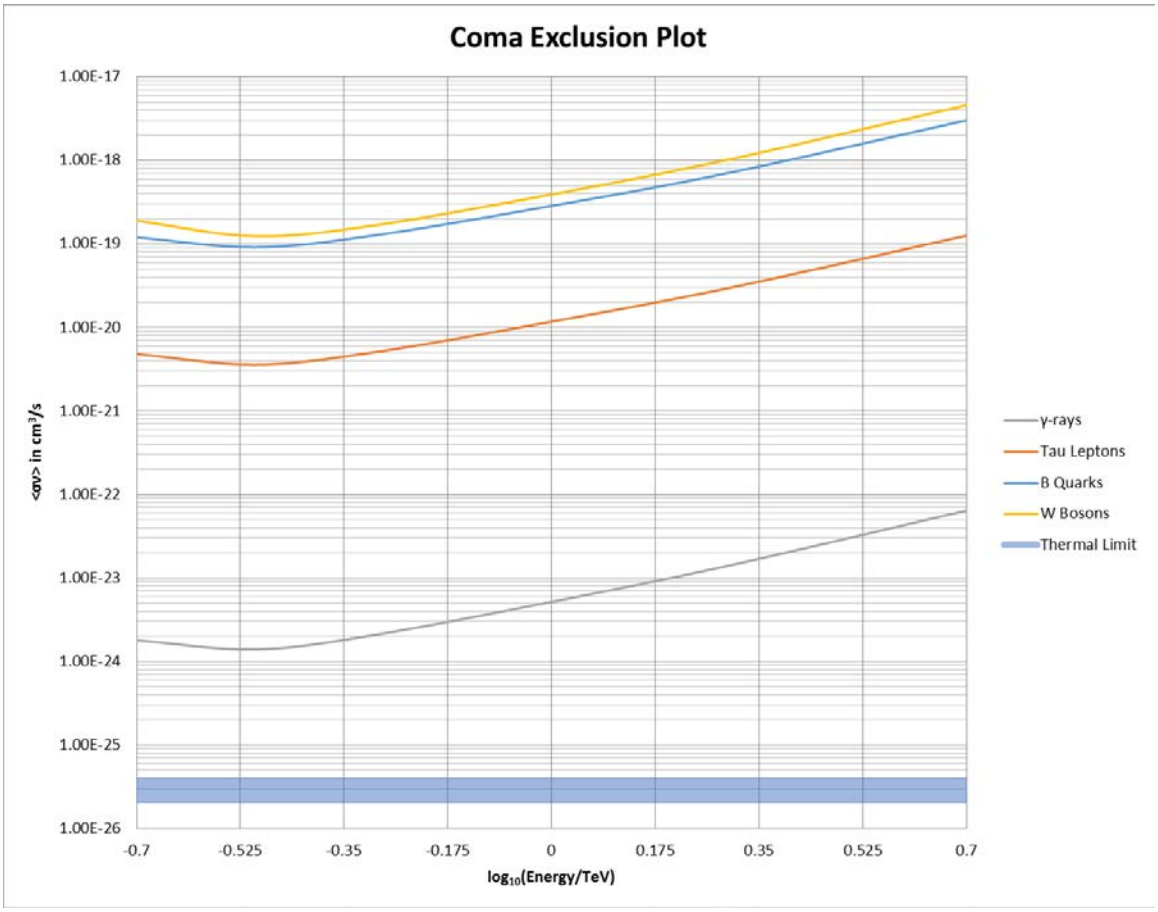

Figure 4-15: Coma cluster exclusion plot

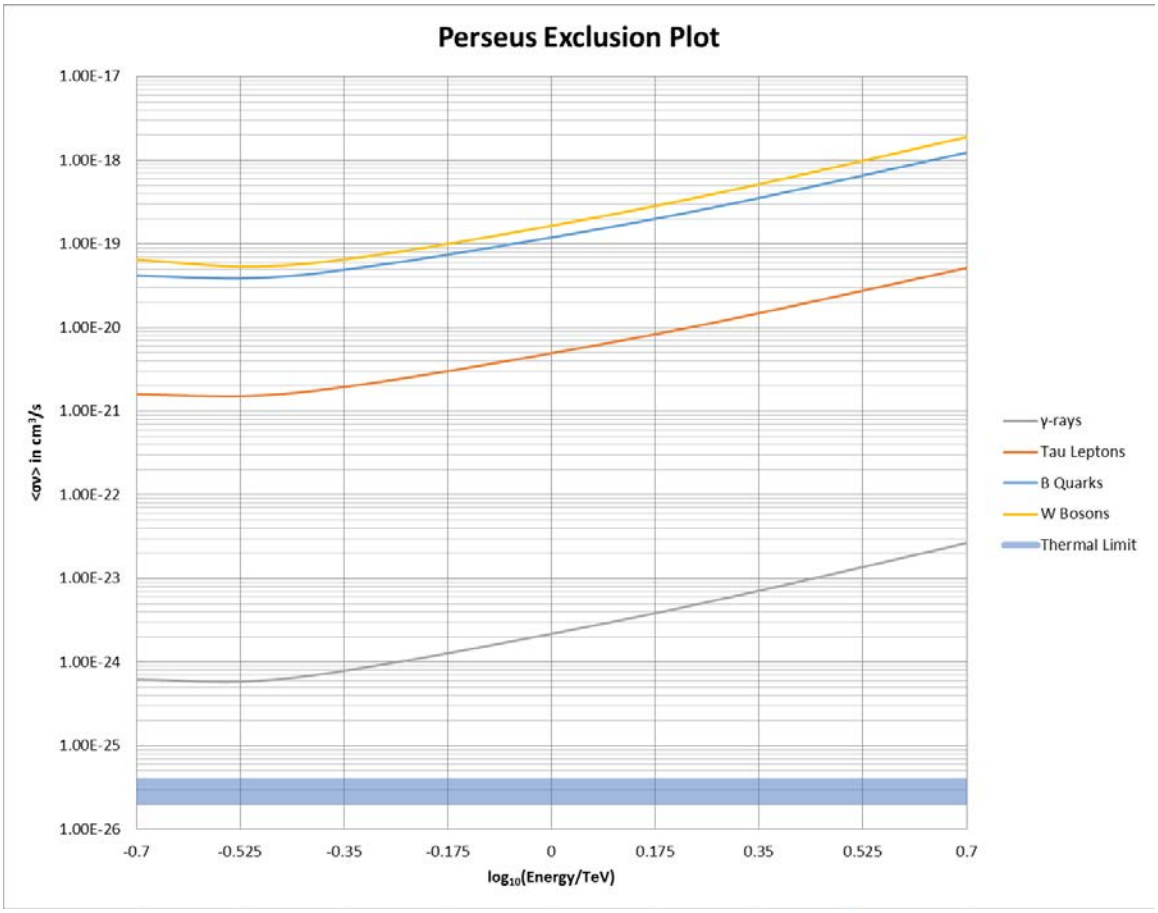

Figure 4-16: Perseus cluster exclusion plot

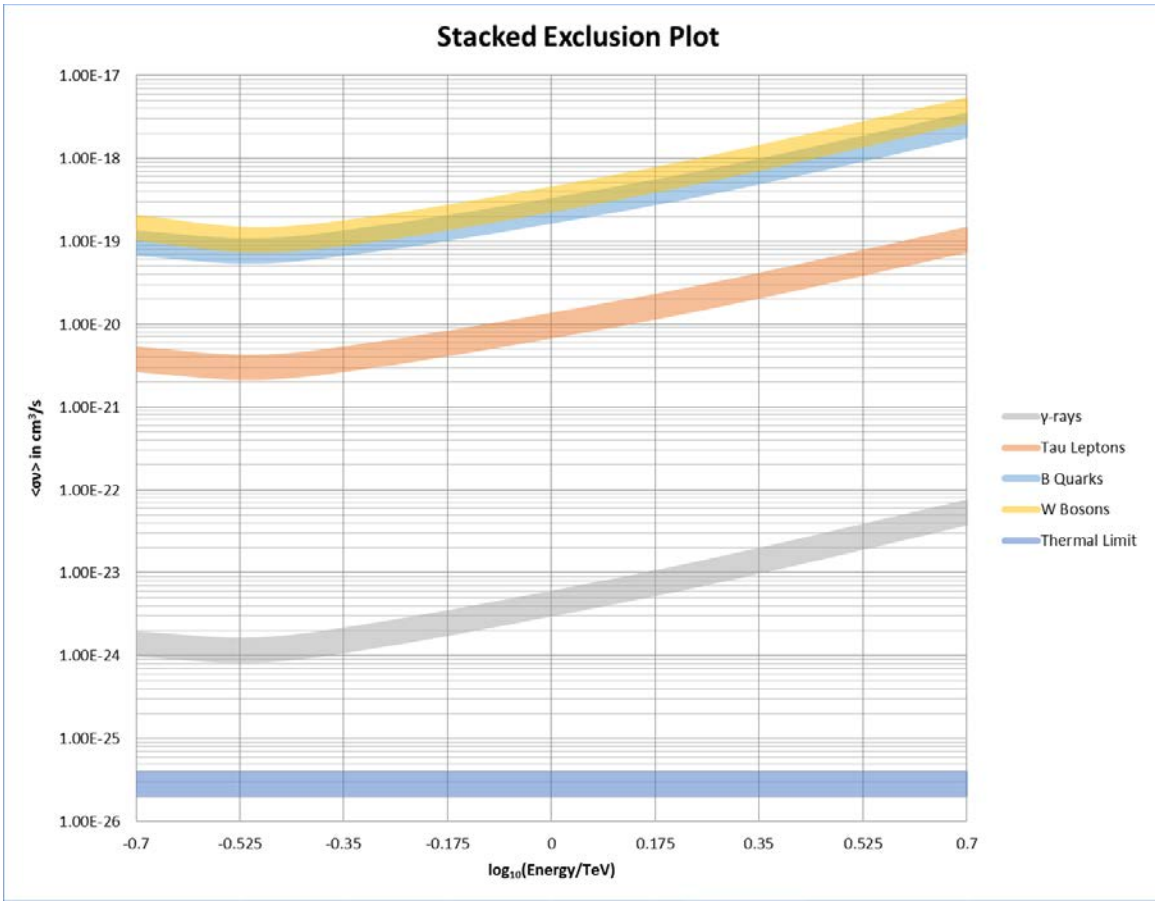

Figure 4-17: Stacked exclusion plot. All limits are shown with shaded ± 1σ error bars.

4.2 Discussion

First, a note on the results from Ben Zitzer (via private communication): "The $\chi + \chi \rightarrow \gamma + \gamma$ spectrum is simply a delta function (or technically speaking a very narrow Gaussian) at the mass of the DM particle. So the weighting function with energy in that case is a Gaussian centered at the mass, with a width approximately of the energy resolution. They are the most constraining because the background is much lower. All the other spectra have backgrounds that include the events at the particle mass and everything below it."

The shape of each of the final state spectra is dependent primarily on the ratio of the DM mass squared to the integral of the effective area. Notice how the curves all have their minima near 300 – 500 GeV. $N^{95\%\ CL}$, t_{obs}, and $J(\Delta\Omega)$ are fixed for each cluster based on output from VEGAS and CLUMPY. The values from the PPPC4DMID tables certainly differ between final states, but may only double across the DM mass range probed. The DM mass squared increases by a factor of 625 going from 200 GeV to 5 TeV. Likewise, the effective area of the array grows with γ-ray energy since both the showers' Cherenkov photon density and lightpool radius grow (see Figure 2-2).

In all the combined plots, the limits from the [YSS 2008] 265 cluster stand out. They are noticeably three to five times higher (less constraining) than the rest of the clusters. This is not an error, rather it is an artifact of the $\langle\sigma v\rangle^{95\%\ CL}$ calculation. It is the most distant of the 12 clusters in the analysis at a redshift of 0.0846 (0.35 Gpc). While it does not have the smallest physical size of the set (R_{500} = 580 kpc [93]), its extreme distance gives it the smallest apparent angular diameter of any of the clusters, 0.2°. On top of that this source was only observed as a result of a GRB alert for a very short duration. Both factors combine to give a low counts upper limit, though a small $N^{95\%\ CL}$ and small t_{obs} will offset in the $\langle\sigma v\rangle^{95\%\ CL}$ calculation. The terms going into the integral expression are not drastically lower than for other clusters. The last deciding piece is the J-factor from CLUMPY. Only A279 and [YSS 2008] 265 have J-factors less than 16 in $\log_{10}[J/(\mathrm{GeV}^2\mathrm{cm}^{-5})]$ space. By contrast, A279 has over 15 times the exposure length as [YSS 2008] 265 in the VERITAS dataset. These various reasons come together to make the [YSS 2008] 265 limits higher.

The stacking method limits are most strongly influenced by each sum in the denominator and numerator. The Perseus cluster contributes the majority of counts and the majority of $t_{obs}J(\Delta\Omega)$ to the calculation. The stacked limits with ± 1σ error bars encompass three clusters' limits and skirt a fourth but stay well above those of Perseus and UGC 9534 for all final state spectra. In the preliminary document, we predicted that this stacking method would yield a more constraining limit than any one cluster by

combining all the datasets. That thinking has since proved to be flawed, but for reasons that were not obvious until all the results became available.

The broad range of the 12 limits presented on each combined plot (over an order of magnitude wide) causes the stacked limit to smear out into essentially a weighted average. Consider instead a scenario where VERITAS observed 12 Perseus-sized clusters with equal J-factors for the same duration without making a detection. Their limits would all overlap on an exclusion plot. Inputting those values of $N^{95\%\ CL}$ and $t_{obs}J(\Delta\Omega)$ into the stacking method would yield a limit that was equal or lower than each of the individual ones. That unfortunately is not the case with the 12 real clusters in the sample. The wide range of sizes, exposures, acceptances (a function of the angular distance from the cluster to the tracking center), and array configurations decreased the effectiveness of the stacking method by breaking uniformity. It turns out even the stacked limits of the four combined dSphs observed by VERITAS are not as constraining as Segue 1's alone is.

The dSph paper will present DM annihilation limits with $<\sigma v>_{min}$ in the 10^{-23} cm^3/s range for $\chi + \chi \rightarrow \tau^+ + \tau^-$ final state, roughly two or three orders of magnitude better than these galaxy cluster limits. Follow-up studies of nearby Fermi-identified targets of opportunity (ToO) with high mass-to-light ratio are producing comparable limits. Why go to all the trouble to analyze these challenging clusters? The answer to that question is one of distinction. No one else in the collaboration has undertaken a galaxy clusters survey due to the difficulties posed in the analysis. Of the clusters only Coma has been analyzed by VERITAS in detail, and the DM limits presented there agree with those of this analysis, "in the 10^{-20} to 10^{-21} cm^3/s range [147]" for tau leptons. The Perseus cluster limits from the MAGIC collaboration are comparable as well, when corrected for the relative size of the signal region [53]. That the dSph limits are more competitive than the galaxy clusters should come as no surprise. The dSphs all have uniform, small radii and were observed directly (targets in the wobble offset) for durations comparable to Perseus cluster's coverage on average. The dSph paper will also utilize CBG and the event weighting method developed by Alex Geringer-Sameth to determine the likelihood of an event coming from the source or background [133] [144]. The event weighting

method is an improvement over the standard VEGAS event source/background estimation method, but has not been committed to the VEGAS source code at the present time. Barring those two exceptions, every effort was made to match the Stage 6 configuration file options used in the dSph analysis for the sake of consistency.

The dSphs and galaxy clusters have not given up their DM secrets yet. Despite deeper exposures no detections have been made, just more constraining upper limits. It has been a topic of much debate within the DM-AsPEN SWG whether to continue observations due to a worsening systematic error. A slight mismatch in the VERITAS α parameter can cause the significance distribution to depart from a Gaussian. This effect compounds the longer the exposure becomes. As it stands, the limits from the current generation of IACTs and satellites are still a few orders of magnitude above the thermal relic limit. That task of closing the parameter space will fall to CTA or the successor of Fermi. Either a detection will be made at a $<\sigma v>$ currently inaccessible or broad WIMP mass ranges will be excluded if they reach the thermal limit. The next generation of direct DM detection experiments are trying to do the same in the lower WIMP mass range. The 13 and 14 TeV results of the LHC might succeed in producing DM. Until then DM exists beyond the realm of our understanding.

APPENDICES

Appendix A: Acronyms

DM – Dark Matter

WIMP – Weakly Interacting Massive Particle

Myr – Megayear

kpc/Mpc/Gpc – Kiloparsec/Megaparsec/Gigaparsec

ALP – Axion-Like Particle

MOND – Modified Newtonian Dynamics

TeVeS – Tensor-Vector-Scalar (Gravity)

ΛCDM – Lambda Cold Dark Matter (Cosmology)

M/L – Mass to Light Ratio

ICM – IntraCluster Medium

CRESST – Cryogenic Rare Event Search with Superconducting Thermometers

CDMS – Cryogenic Dark Matter Search

EDELWEISS – Expérience pour DEtecter Les Wimps En Site Souterrain

ArDM – Argon Dark Matter

LUX – Large Underground Xenon (Experiment)

Fermi-LAT – Fermi Large Area Telescope

Sr – Steradian

HESS – High Energy Stereoscopic System

VERITAS – Very Energetic Radiation Imaging Telescope Array System

MAGIC – Major Atmospheric Gamma Imaging Cherenkov Telescopes

HAWC – High Altitude Water Cherenkov Observatory

CTA – Cherenkov Telescope Array

LHC – Large Hadron Collider

CERN – Conseil Européen pour la Recherche Nucléaire

IC – Inverse Compton

dSph – Dwarf Spheroidal Galaxy

GC – Galactic Center

NFW profile – Navarro-Frenk-White profile

PWN – Pulsar Wind Nebula

SNR – SuperNova Remnant

AGN – Active Galactic Nucleus

FOV – Field of View

SMBH – SuperMassive Black Hole

HIFLUGCS – HIghest X-ray FLUx Galaxy Cluster Sample

ROSAT – Röntgensatellit

SDSS – Sloan Digital Sky Survey

DSS2 – Digital Sky Survey 2

SAO – Smithsonian Astrophysical Observatory

FITS – Flexible Image Transport System

NAOJ – National Astronomical Observatory of Japan

JEM-EUSO – Japanese Experiment Modu – Extreme Universe Space Observatory

UHECR – UltraHigh Energy Cosmic-Ray

VHE – Very High Energy

EAS – Extensive Air Shower

IACT – Imaging Atmospheric Cherenkov Telescope

PMT – PhotoMultiplier Tube

OSS – Optical Support Structure

CCD – Charge-Coupled Device

PSF – Point Spread Function

QE – Quantum Efficiency

FADC – Flash Analog-to-Digital Converter

VME DAQ – Versa Module Eurocard Data Acquisition

CFD – Constant Fraction Discriminator

ZCD – Zero-Crossing Discriminator

RFB – Rate FeedBack Loop

FPGA – Field-Programmable Gate Array

ECL – Emitter Coupled Logic

PST – Pattern Selection Trigger

PDM – Pulse Delay Module

SAT – Sub-Array Trigger Board

GPS – Global Positioning System

VBF – VERITAS Bank Format

VEGAS – VERITAS Gamma-Ray Analysis Suite

LED – Light Emitting Diode

RMS – Root Mean Squares

MSL – Mean Scaled Length

MSW – Mean Scaled Width

SHM – Shower Height Maximum

RBM – Ring Background Method

RF – ReFlected Rings Method

CBG – Crescent Background Method

MLM – Maximum Likelihood Method

d.o.f. – Degree of Freedom

DM-AsPEN SWG - Dark Matter, Astroparticle, and Extragalactic Science Working Group

CL – Confidence Level

UL – Upper Limit

LIDAR – Light Detection and Ranging

DQM – Data Quality Management

GRB – Gamma-Ray Burst

ToO – Target of Opportunity

MCXC – a Meta-Catalogue of X-ray Detected Clusters of Galaxies

PPPC4DMID – A Poor Particle Physicist's Cookbook for Dark Matter Indirect Detection

KASCADE – The Kertzman and Sembroski Cherenkov Airshower and Detector Emulation

---

Cluster Designations:

NGC – New General Catalogue of Nebulae and Clusters of Stars Designation

3C – Third Cambridge Catalogue of Radio Sources Designation

A/ACO – Abell Cluster Object Catalog Designation

UGC – Uppsala General Catalogue of Galaxies Designation

[YSS 2008] – Yoon-Schawinski-Sheen 2008 SDSS Paper Cluster Designation

---

List of References:

Phys. Lett. B – Physics Letters B

Astrophys. J. – The Astrophysical Journal

Phys. Rev. D – Physical Review D

Mon. Not. Royal Astron. Soc. – Monthly Notices of the Royal Astronomical Society

Astrophys. J. Lett. – The Astrophysical Journal Letters

J. Phys.: Conf. Ser. – Journal of Physics: Conference Series

Nucl. Instrum. Meth. Phys. Res. A – Nuclear Instruments and Methods in Physics Research Section A

AIP Conf. Proc. – AIP Conference Proceedings

Proc. ICRC – Proceedings of the International Cosmic Ray Conference

Astropart. Phys. – Astroparticle Physics

Exp. Astron. – Experimental Astronomy

J. High Energy Phys. – Journal of High Energy Physics

Trudy Astrofiz. Inst. Alma-Ata – Trudy Astrofizicheskogo Instituta Alma-Ata (Proceedings of the Astrophysical Institute Alma-Ata)

Astron. J. – The Astronomical Journal

J. Cosmol. Astropart. Phys. – Journal of Cosmology and Astroparticle Physics

Astron. Astrophys. – Astronomy and Astrophysics

Astrophys. J. Supp. – The Astrophysical Journal Supplemental Series

Doklady Akad. Nauk SSSR – Doklady Akademii Nauk SSSR (Proceedings of the USSR Academy of Sciences)

Sci. Am. – Scientific American

Nucl. Phys. B (Proc. Suppl.) – Nuclear Physics B: Proceedings Supplements

Sci. and Eng. – Science and Engineering

Czech. J. Phys. – Czechoslovak Journal of Physics

J. Solar Energy Sci. and Eng. – Journal of Solar Energy Science and Engineering

IEEE-NPSS – Institute of Electrical and Electronics Engineers–Nuclear and Plasma Sciences Society

Space Sci. Rev. – Space Science Review

Comp. Phys. Comm. – Computer Physics Communications

Appendix B: VERITAS Runlists

Target: 1ES 0120+340, Cluster: NGC 507

Date	Data	Flasher	Usable Duration (sec) & Weather		DQM Comments
20071011	37031	37034	1200,	A	Cut sec 0 – 60
20071020	37426	37433	1200,	A	
20071106	37659	37668	780,	C	Cut sec 780 – 1500
20071110	37798	37813	300,	C	Cut sec 0 – 480 and 780 – 1200
20071129	38145	38154	420,	C	Cut sec 0 – 420 and 840 – 1200
20080102	38584	38594	1020,	C	Cut sec 300 – 480
20090117	44026	44027	1200,	C	
20100105	49255	49254	1140,	C	Cut sec 420 – 480
20101001	52300	52288	1200,	A	

Target: 1ES 0414+009, Cluster: NGC 1550

Date	Data	Flasher	Usable Duration (sec) & Weather		DQM Comments
20071207	38312	38309	300,	C	Cut sec 0 – 600 and 900 – 1200
20080110	38682	38685	1200,	A	
20080111	38714	38731	1200,	A	
20080112	38755	38786	1200,	A	
20080113	38794	38817	1200,	B	
20080114	38826	38817	1140,	A	Cut sec 1140 – 1200

20080126	38926	38925	600,	C	Cut sec 0 – 300 and 900 – 1200
20080129	38936	38950	1080,	C	Cut sec 0 – 120
20080131	38988	38950	1080,	B	Cut sec 1080 – 1200
20080201	39010	39029	840,	B	Cut sec 360 – 720
20080206	39107	39132	1200,	A	
20080208	39172	39195	1200,	A	
20090103	43926	43948	1200,	A	
20090227	44714	44721	360,	B	Cut sec 360 – 960
20090302	44805	44821	1080,	A	Cut sec 180 – 300
20090928	47242	47143	1200,	A	
20090930	47265	47143	1140,	A	Cut sec 0 – 60
20090930	47269	47143	1200,	A	
20091001	47281	47143	840,	B	
20091014	47414	47407	1200,	A	
20091015	47454	47451	1200,	A	
20091022	47676	47667	1200,	A	
20091025	47782	47772	480,	C	Cut sec 0 – 720
20091112	48234	48224	1200,	C	
20091119	48426	48437	1200,	A	
20091120	48467	48473	1200,	A	
20091125	48636	48641	720,	A	Cut sec 0 – 480
20091210	48813	48818	1140,	A	Cut sec 0 – 60
20091211	48853	48863	1080,	A	Cut sec 120 – 240
20091216	48961	48967	720,	B	Cut sec 0 – 480

20091219	49058	49054	1200,	A	
20091219	49062	49054	1200,	A	
20100108	49320	49336	1200,	B	
20100108	49324	49336	1200,	A	
20100108	49326	49336	1200,	A	
20100112	49469	49480	480,	A	
20100112	49470	49480	900,	A	Cut sec 900 – 1200
20100113	49504	49516	420,	C	Cut sec 420 – 1200
20100114	49535	49544	1200,	A	
20100115	49567	49587	1200,	B	
20100115	49572	49587	1200,	B	
20100117	49632	49649	1140,	A	Cut sec 780 – 840
20100117	49636	49649	1200,	C	
20100121	49698	49798	1020,	B	Cut sec 0 – 180
20100212	49935	49943	1200,	A	
20100213	49967	49980	840,	A	Cut sec 240 – 360 and 960 – 1200
20100215	50026	50035	1200,	A	
20100216	50058	50064	1200,	A	
20100218	50112	50119	1140,	A	Cut sec 720 – 780
20100219	50140	50149	1200,	A	
20101008	52416	52401	1140,	A	Cut sec 840 – 900
20101102	52905	52904	1200,	A	
20101105	53013	52993	1080,	C	Cut sec 1080 – 1200
20101110	53165	53160	1200,	A	

20101114	53287	53296	1200,	A	
20101201	53451	53453	1200,	A	
20101210	53765	53777	1200,	C	
20101226	53951	53948	1200,	A	
20110101	54053	54047	600,	C	Cut sec 600 – 1200
20110104	54182	54177	1200,	A	
20110105	54217	54224	720,	C	Cut sec 0 – 480
20110110	54346	54362	1200,	A	
20110125	54533	54544	1080,	C	Cut sec 1080 – 1200
20110126	54546	54562	1200,	C	
20110206	54881	54892	1200,	A	
20111023	58155	58150	1080,	A	Cut sec 0 – 120
20111104	58471	58474	780,	A	Cut sec 780 – 1200
20111128	58991	58986	1200,	A	
20111222	59283	59282	1200,	B	
20111225	59378	59387	1200,	A	
20120125	60009	60022	900,	B	Cut sec 540 – 660 and 840 – 1020
20120213	60340	60347	1200,	A	
20120224	60577	60598	540,	A	Cut sec 540 – 600
20121012	64043	64045	900,	A	Cut sec 900 – 1200
20121013	64077	64079	1200,	A	
20121021	64292	64281	1200,	A	
20121112	64729	64731	1200,	A	
20121206	65254	65253	1200,	A	

20130103	65743	65745	2400,	A	
20130112	65977	65985	1200,	A	
20130115	66072	66088	1200,	A	
20130131	66528	66526	1320,	A	Cut sec 1320 – 1800
20130205	66554	66590	1200,	A	
20130303	67087	67097	1200,	B	
20131031	70377	70370	1800,	A	
20131107	70552	70544	1800,	A	
20131111	70667	70671	900,	A	Cut sec 0 – 900
20131230	71342	71344	1800,	A	

Target: 1ES 0446+449, Cluster: 3C 129

Date	Data	Flasher	Usable Duration (sec) & Weather		DQM Comments
20080925	41616	41593	1200,	A	
20081003	41951	41858	1200,	C	
20081003	41957	41858	960,	C	Cut sec 0 – 240
20081003	41958	41858	1080,	C	Cut sec 1080 – 1200
20081022	42318	42215	600,	A	Cut sec 600 – 1200
20081022	42319	42215	1200,	A	
20081022	42320	42215	1200,	A	
20081022	42321	42215	1200,	A	
20081023	42366	42346	1200,	A	
20081023	42367	42346	1200,	A	

20081023	42368	42346	1200,	A	
20081024	42407	42388	1200,	A	
20081024	42408	42388	1200,	A	
20081024	42409	42388	1200,	A	
20081024	42410	42388	1200,	A	
20081025	42442	42433*	1200,	A	
20081025	42443	42433*	1200,	A	
20081025	42444	42433*	1200,	A	
20081025	42445	42433*	660,	A	
20081026	42480	42460*	1200,	A	
20081026	42481	42460*	1200,	A	
20081026	42482	42460*	1200,	A	
20081123	43232	43231	600,	C	Cut sec 600 – 1200
20091217	48996	48967	1200,	C	
20100107	49298	49292	1200,	C	
20100107	49299	49292	1200,	C	
20100107	49300	49292	1200,	C	
20100111	49433	49438	360,	C	Cut sec 240 – 720
20100111	49434	49438	720,	C	Cut sec 720 – 1200
20100111	49435	49438	600,	C	Cut sec 600 – 1200
20100113	49506	49516	480,	C	Cut sec 480 – 1200
20100113	49507	49516	1200,	C	
20100113	49508	49516	1080,	C	Cut sec 0 – 120
20100117	49640	49649	1200,	B	

20100118	49676	49671	300,	C	Cut sec 0 – 480 and 780 – 1200
20100206	49808	49798	600,	C	Cut sec 600 – 1200
20100206	49811	49798	840,	C	Cut sec 0 – 360
20100207	49829	49798	1200,	C	
20100207	49830	49798	960,	C	Cut sec 960 – 1200
20100207	49831	49798	1200,	C	
20100207	49832	49798	720,	C	Cut sec 720 – 1200
20100207	49833	49798	1140,	C	
20100208	49843	49850	1140,	C	Cut sec 0 – 60
20100208	49844	49850	1200,	C	

*Note: Runs with an asterisk were taken at 0.7° wobble offset

Target: 1ES 1440+122, Cluster: UGC 9534

Date	Data	Flasher	Usable Duration (sec) & Weather		DQM Comments
20080601	41043	41049	1200,	A	
20080603	41090	41098	1200,	B	
20080604	41110	41131	1200,	A	
20080607	41186	41195	900,	A	
20090318	44946	44940	1200,	B	
20090320	45001	44981	900,	C	Cut sec 900 – 1200
20090416	45516	45511	1200,	A	
20090417	45537	45539	1200,	A	
20090417	45543	45539	1200,	A	

20090419	45597	45591	1200,	A	
20090420	45618	45619	1200,	A	
20090421	45646	45657	1200,	A	
20090424	45730	45732	780,	A	Cut sec 780 – 1200
20090424	45735	45732	1200,	C	
20090425	45754	45762	480,	C	Cut sec 0 – 720
20090425	45758	45762	1080,	C	Cut sec 420 – 540
20090426	45779	45778	600,	B	Cut sec 0 – 600
20090426	45783	45778	480,	A	Cut sec 480 – 1200
20090426	45787	45778	960,	B	Cut sec 0 – 240
20090427	45806	45812	1080,	A	Cut sec 960 – 1080
20090427	45808	45812	1200,	A	
20090428	45831	45830	960,	B	Cut sec 420 – 660
20090428	45835	45830	1200,	A	
20100214	50020	50006	1200,	A	
20100215	50048	50035	1200,	A	
20100215	50052	50035	1200,	A	
20100216	50084	50064	1200,	A	
20100218	50135	50119	1200,	A	
20100310	50273	50315	1200,	A	
20100310	50278	50315	1200,	A	
20100312	50334	50318	1200,	A	
20100312	50338	50318	1200,	A	
20100313	50367	50365	1200,	A	

20100314	50398	50396	1200,	A	
20100316	50473	50472	1200,	A	
20100316	50478	50472	1200,	A	
20100317	50504	50502	1200,	B	
20100317	50508	50502	1200,	B	
20100317	50513	50502	600,	B	
20100318	50548	50533	1200,	A	
20100318	50552	50533	1200,	A	
20100319	50581	50575	1200,	A	
20100320	50612	50606	600,	A	
20100407	50796	50782	1200,	A	
20100415	51014	51007	1200,	A	
20100420	51114	51104	1200,	A	
20100607	51574	51583	600,	B	Cut sec 600 – 1200
20100611	51642	51647	1200,	B	
20100614	51698	51707	1200,	A	
20100617	51760	51769	1200,	A	
20130504	68304	68308	900,	C	Cut sec 900 – 1800

Target: 1ES 1627+402, Cluster: A2199

Date	Data	Flasher	Usable Duration (sec) & Weather		DQM Comments
20080312	39880	39874	1200,	A	
20080312	39881	39874	1200,	A	

20080313	39900	39874	1200,	A	
20080313	39901	39874	1200,	A	
20080313	39902	39874	600	A	
20080314	39927	39924	960,	A	Cut sec 720 – 960
20080315	39957	39953	1080,	A	
20080401	40150	40133	1200,	A	
20080401	40154	40133	1200,	A	
20080401	40155	40133	1200,	A	
20080403	40199	40192	1200,	A	
20080403	40200	40192	1200,	A	
20080403	40201	40192	1200,	A	
20080403	40202	40192	1200,	A	
20080403	40203	40192	1080,	A	Cut sec 480 – 600
20080404	40229	40208	1200,	A	
20080404	40230	40208	1200,	A	
20080404	40231	40208	1200,	A	
20080405	40254	40265	1200,	A	
20080405	40258	40265	1200,	A	
20080406	40288	40265	1200,	A	
20080406	40289	40265	1200,	A	
20080406	40290	40265	1200,	A	
20080407	40318	40265	1200,	A	
20080407	40319	40265	1200,	A	
20080408	40340	40265	1200,	A	

20080408	40341	40265	1200,	A	
20080408	40342	40265	1200,	A	
20080408	40343	40265	1200,	A	
20080409	40367	40355	1200,	A	
20080413	40464	40355	1200,	A	
20080413	40468	40355	1200,	A	
20080413	40469	40355	1200,	A	
20080413	40472	40355	1200,	A	
20080427	40523	40355	1200,	A	
20080427	40524	40355	1200,	A	
20080504	40717	40355	1200,	C	
20080509	40826	40355	1200,	C	
20080511	40862	40355	960,	C	Cut sec 0 – 240
20080511	40863	40355	960,	C	Cut sec 600 – 840
20080511	40864	40355	1200,	C	
20090503	45940	45950	1140,	B	Cut sec 1140 – 1200

Target and Cluster: A400

Date	Data	Flasher	Usable Duration (sec) & Weather		DQM Comments
20130928	69767	69755	1800,	A	
20130928	69768	69755	1800,	A	
20130928	69769	69755	1800,	A	
20130928	69770	69755	1740,	A	Cut sec 1740 – 1800

20130929	69792	69781	1800,	A	
20130929	69793	69781	1740,	A	Cut sec 360 – 420
20130929	69794	69781	480,	A	
20131013	70091	70098	1200,	A	Cut sec 0 – 600 and 1800 – 2400
20131015	70120	70088	600,	A	Cut sec 0 – 1200
20131015	70121	70088	900,	A	Cut sec 0 – 900

Target: GRB 080330, Cluster: A1213

Date	Data	Flasher	Usable Duration (sec) & Weather		DQM Comments
20080330	40090	40078	780,	A	Cut sec 300 – 720
20080330	40094	40078	1140,	A	Cut sec 0 – 60

Target: GRB 100513A, Cluster: SDSS-C4-DR3 1079

Date	Data	Flasher	Usable Duration (sec) & Weather		DQM Comments
20100513	51323	51332	1200,	A	
20100513	51324	51332	1200,	A	

Target: LAT HIGHE 20130117, Cluster: [YSS 2008] 265

Date	Data	Flasher	Usable Duration (sec) & Weather	DQM Comments
20130117	66151	66158	1800, A	

Target: RGB J0152+017, Cluster: A279

Date	Data	Flasher	Usable Duration (sec) & Weather	DQM Comments
20071117	38023	38046	1200, A	
20071117	38024	38046	1200, A	
20071118	38058	38076	1200, A	
20071204	38187	38186	1200, A	
20071206	38261	38267	1200, A	
20071229	38499	38495	1200, C	
20080113	38787	38817	1020, A	Cut sec 840 – 1020
20080113	38788	38817	1200, A	
20101207	53653	53678	1200, B	
20110928	57790	57781	1200, C	
20110929	57812	57808	1200, C	
20111103	58447	58453	1200, A	
20121106	64614	64609	1320, A	
20131003	69880	69870	1800, A	
20131006	69952	69951	1800, A	
20131101	70431	70422	1620, A	

20131108	70577	70576	1800,	A	
20131128	70844	70843	420,	C	Cut sec 0 – 1080 and 1320 – 1620
20131224	71189	71191	2100,	A	
20131230	71341	71344	1800,	A	Cut sec 1140 – 1200
20140102	71421	71430	1200,	A	

Target and Cluster: Coma cluster

Date	Data	Flasher	Usable Duration (sec) & Weather		DQM Comments
20080306	39711	39693	1200,	A	
20080306	39712	39693	1200,	A	
20080312	39872	39874	840,	B	Cut sec 840 – 1200
20080312	39873	39874	480,	A	Cut sec 360 – 600 and 720 – 1200
20080313	39889	39874	1200,	A	
20080330	40098	40078	1200,	A	
20080330	40099	40078	1200,	A	
20080330	40100	40078	1200,	A	
20080330	40101	40078	900,	A	Cut sec 0 – 300
20080331	40126	40125	1200,	A	
20080331	40127	40125	1200,	A	
20080331	40128	40125	1200,	A	
20080331	40130	40125	1200,	A	
20080403	40196	40192	1200,	A	
20080403	40197	40192	1200,	A	

20080403	40198	40192	1200,	A
20080404	40227	40208	1200,	A
20080404	40228	40208	1200,	A
20080405	40251	40265	1200,	A
20080405	40252	40265	1200,	A
20080405	40253	40265	1200,	A
20080405	40256	40265	1200,	A
20080405	40257	40265	1200,	A
20080406	40284	40265	1200,	A
20080406	40285	40265	1200,	A
20080406	40286	40265	1200,	A
20080407	40316	40265	1200,	A
20080407	40317	40265	1200,	A
20080408	40337	40265	1200,	A
20080408	40338	40265	1200,	A
20080409	40364	40355	1200,	A
20080409	40365	40355	1200,	A
20080409	40366	40355	1200,	A
20080410	40393	40355	1200,	A
20080410	40394	40355	1200,	A
20080410	40395	40355	1200,	A
20080410	40396	40355	1200,	A
20080411	40426	40355	1200,	A
20080411	40427	40355	1200,	A

20080411	40428	40355	1200,	A	
20080411	40429	40355	1200,	A	
20080412	40455	40355	1200,	A	
20080425	40493	40355	1200,	A	
20080425	40494	40355	1200,	A	
20080426	40509	40355	1200,	A	
20080426	40510	40355	1200,	A	
20080427	40521	40355	1200,	A	
20080427	40522	40355	1200,	A	
20080428	40536	40355	840,	A	
20080428	40537	40355	1200,	A	
20080428	40538	40355	1200,	A	
20080429	40559	40355	780,	A	Cut sec 120 – 660
20080430	40589	40355	1200,	A	
20080501	40613	40355	1200,	A	
20080501	40614	40355	1200,	A	
20080501	40615	40355	1200,	A	
20080501	40616	40355	1200,	A	

Target and Cluster: Perseus cluster

Some notes on the Perseus cluster: the Perseus cluster was observed in a variety of VERITAS observation campaigns, giving rise to distinct pointing strategies.

- NGC 1275 N,S,E,W 0.5° wobble offset pointing scheme (2009)
- IC 310 N,S 0.5° wobble offset pointing scheme (2012)
- NGC 1275 1,2,3,4 + IC 310 – 3 (NO IC 310 – 4) pointing scheme (2010 – 2013)
- Perseus points 1,2,3,4,5,6 pointing scheme (2013)

IC 310 did in fact have data taken in all four 0.5° wobble offset positions (N,S,E,W), but the data taken on the East and West wobbles did not satisfy the DQM criteria for inclusion. Figure B-1 shows the central 3° × 3° of the Perseus cluster with the last two pointing schemes plotted. The last two schemes take the shape of a tilted rectangle to enhance coverage of NGC 1275 and IC 310, two active galaxies within the Perseus cluster separated by 0.5° that have been detected in γ-rays. There was an error in the encoding of IC 310 – 4 which displaced it -1° in declination from its intended position. The angular separation of IC 310 – 4 is greater than 1.225° from the center of the cluster so data taken there is discarded. Subsequently, the locations of the six points were recalculated and relabeled as Perseus points 1,2,3,4,5,6.

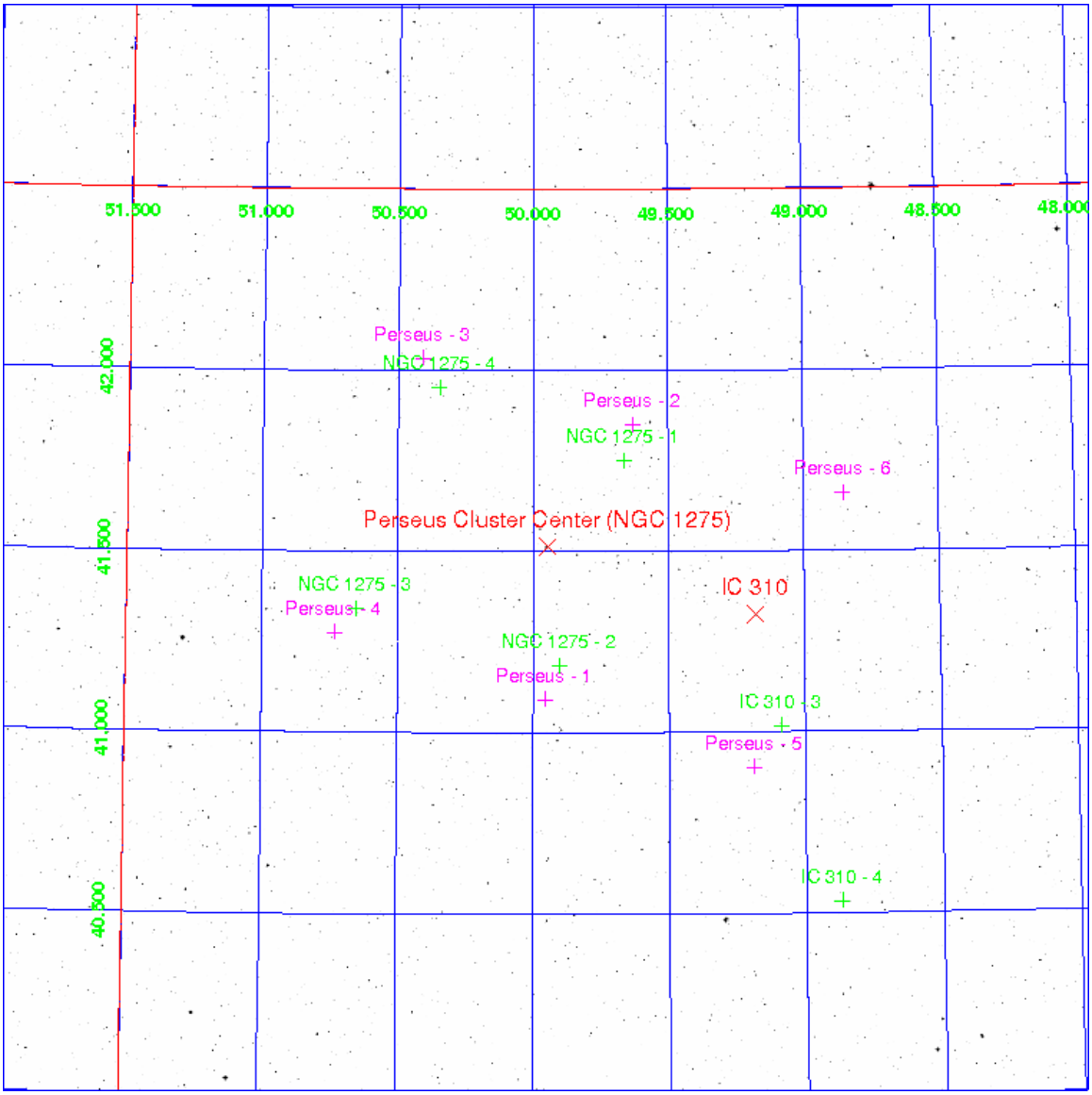

Figure B-1: The center of the Perseus cluster with the NGC 1275 1,2,3,4 + IC 310 – 3,4 and Perseus points 1,2,3,4,5,6 pointing schemes overlaid. Note: the NGC 1275 N,S,E,W and the IC 310 N,S 0.5° wobble offset pointing schemes were omitted for clarity (overlapping pointings)

NGC 1275 N,S,E,W 0.5° wobble offset pointing scheme

Date	Data	Flasher	Usable Duration (sec) & Weather	DQM Comments
20090115	43996	43992	1200, A	
20090115	43997	43992	1200, A	
20090115	43998	43992	1200, A	
20090115	43999	43992	1200, A	
20090116	44006	44005	1200, A	
20090116	44007	44005	1200, A	
20090116	44008	44005	1200, A	
20090116	44009	44005	1200, A	
20090116	44010	44005	1200, A	
20090116	44012	44005	1200, A	
20090118	44045	44027	1200, A	
20090118	44046	44027	1200, A	
20090118	44047	44027	1200, A	
20090213	44518	44525	1200, A	
20090213	44519	44525	1200, A	
20090214	44526	44525	1200, A	
20090214	44527	44525	1200, A	
20090214	44528	44525	1140, A	Cut sec 1140 – 1200
20090217	44546	44557	900, A	Cut sec 0 – 300
20090219	44567	44577	1200, A	
20090219	44568	44577	1200, A	

20090220	44600	44623	1200,	B	
20090221	44632	44646	1200,	B	
20090222	44651	44659	960,	B	Cut sec 300 – 540
20090222	44652	44659	1200,	B	
20090226	44683	44691	1200,	A	

IC 310 N,S 0.5° wobble offset pointing scheme

Date	Data	Flasher	Usable Duration (sec) & Weather		DQM Comments
20121019	64232	64234	660,	C	Cut sec 120 – 240 and 780 – 1200
20121115	64812	64816	1200,	C	
20121115	64813	64816	1200,	B	
20121119	64896	64900	900,	C	Cut sec 900 – 1800
20121120	64939	64951	1800,	B	
20121205	65217	65218	420,	C	Cut sec 0 – 120 and 720 – 1800

NGC 1275 1,2,3,4 + IC 310 – 3 pointing scheme

Date	Data	Flasher	Usable Duration (sec) & Weather		DQM Comments
20101106	53041	53023	1200,	A	
20101106	53042	53023	1200,	A	
20101106	53043	53023	1200,	A	
20101106	53044	53023	1200,	A	
20101106	53045	53023	1200,	A	

20101106	53046	53023	1140,	A	Cut sec 0 – 60
20111008	57985	57988	960,	A	Cut sec 960 – 1140
20111008	57986	57988	1200,	A	
20111008	57987	57988	1200,	A	
20111009	57991	57992	900,	A	Cut sec 0 – 300
20121205	65212	65208	1200,	A	
20121206	65250	65253	1200,	A	
20121206	65251	65253	600,	A	Cut sec 0 – 600
20121208	65307	65310	1200,	A	
20121208	65308	65310	1200,	A	
20121209	65334	65345	1020,	B	
20121211	65401	65369	1800,	A	
20121211	65402	65369	1800,	A	
20121212	65440	65458	1200,	B	
20130103	65741	65745	1200,	A	
20130106	65804	65825	1200,	A	
20130106	65806	65825	1200,	A	
20130106	65807	65825	1200,	A	
20130106	65808	65825	1200,	A	
20130109	65907	65919	1200,	A	
20130109	65908	65919	1200,	A	
20130109	65909	65919	1200,	A	
20130109	65910	65919	840,	A	Cut sec 840 – 900
20130109	65905	65919	1200,	A	

20130114	66040	66006	720,	A	Cut sec 360 – 600 and 840 – 1080
20130114	66042	66006	1140,	A	Cut sec 780 – 840
20130114	66043	66006	1200,	A	
20130130	66520	66278	1800,	A	
20130131	66523	66526	1200,	A	Cut sec 960 – 1560
20130131	66524	66526	1500,	A	Cut sec 0 – 300
20130131	66525	66526	1800,	A	
20130201	66532	66535	1680,	A	Cut sec 420 – 480 and 960 – 1020
20130202	66540	66547	1800,	B	
20130202	66541	66547	1800,	B	
20130202	66542	66547	1800,	B	
20130205	66552	66590	1800,	A	
20130205	66553	66590	1800,	A	
20130206	66575	66590	1800,	A	
20130206	66576	66590	1800,	A	
20130207	66598	66611	900,	A	Cut sec 0 – 600 and 1500 – 1800
20130207	66599	66611	1800,	A	
20130207	66600	66611	1680,	A	Cut sec 540 – 660
20130208	66621	66627	1500,	A	Cut sec 1500 – 1560
20130208	66622	66627	1500,	A	Cut sec 0 – 300
20130208	66623	66627	1800,	A	
20130210	66655	66659	1800,	A	
20130210	66656	66659	1800,	A	
20130210	66657	66659	1800,	A	

20130211	66674	66685	1800,	A	
20130211	66675	66685	1800,	A	
20130211	66676	66685	1800,	A	
20130213	66727	66743	1800,	A	
20130213	66728	66743	960,	A	Cut sec 840 – 1080 and 1200 – 1260
20130213	66729	66743	600,	A	
20130906	69489	69483	1800,	A	
20130906	69490	69483	1800,	A	
20130906	69491	69483	1800,	A	
20130906	69492	69483	720,	A	Cut sec 720 – 900

Perseus points 1,2,3,4,5,6 pointing scheme

Date	Data	Flasher	Usable Duration (sec) & Weather		DQM Comments
20130911	69524	69516	1080,	A	Cut sec 1080 – 1800
20130930	69817	69813	900,	A	Cut sec 900 – 1560
20131001	69839	69824	1800,	A	
20131001	69840	69824	1320,	A	Cut sec 1320 – 1620
20131003	69882	69870	1800,	A	
20131003	69883	69870	900,	A	
20131004	69912	69870	1740,	A	Cut sec 0 – 60
20131004	69913	69870	1800,	A	
20131005	69939	69928	1800,	A	
20131005	69940	69928	1800,	A	

20131006	69958	69951	1800,	A	
20131006	69959	69951	1800,	A	
20131007	69980	69969	1800,	B	
20131007	69981	69969	1800,	B	
20131008	70001	69991	1320,	B	Cut sec 0 – 180 and 660 – 960
20131009	70022	70024	1800,	A	
20131009	70023	70024	1800,	A	
20131012	70073	70077	1800,	A	
20131012	70074	70077	1740,	A	Cut sec 1440 – 1500
20131013	70096	70098	1800,	A	
20131013	70097	70098	1680,	A	Cut sec 780 – 900
20131014	70114	70116	600,	B	Cut sec 0 – 600 and 1200 – 1800
20131014	70115	70116	1200,	B	Cut sec 0 – 600
20131028	70316	70313	1800,	A	
20131030	70345	70338	1800,	B	
20131030	70346	70338	900,	B	
20131030	70348	70338	900,	A	
20131030	70349	70338	1800,	A	
20131030	70350	70338	1800,	A	
20131031	70372	70370	2700,	A	
20131031	70374	70370	1800,	A	
20131031	70375	70370	1800,	A	
20131101	70434	70422	1800,	A	
20131101	70435	70422	1800,	A	

20131101	70436	70422	1800,	A	
20131101	70437	70422	1800,	A	
20131102	70454	70446	720,	A	
20131102	70456	70446	1800,	A	
20131102	70457	70446	1800,	A	
20131102	70459	70446	780,	A	Cut sec 780 – 1080
20131102	70460	70446	2400,	A	
20131104	70481	70483	1380,	A	
20131104	70484	70483	1800,	A	
20131104	70485	70483	1800,	A	
20131104	70486	70483	1800,	A	
20131105	70511	70510	1200,	A	Cut sec 1200 – 1800
20131106	70528	70519	1800,	A	
20131106	70529	70519	1800,	A	
20131107	70550	70544	1200,	A	

Appendix C: Rolke Method

The Rolke method is the preferred method for upper limits calculations in VERITAS analyses when a source is not detected at the 5 σ level [136]. Such is the case with the DM in dSphs and this work follows that precedent. The statistical method builds upon the Feldman-Cousins method to allow estimation of limits in the presence of nuisance parameters [162]. Some examples of nuisance parameters are random variables such as simulation efficiency or uncertainties in either the signal or background regions. The Feldman-Cousins method is valid only when the nuisance parameter is known exactly, whereas the Rolke method allows for estimates with statistical or systematic errors. The Rolke method is included in ROOT as the TObject TRolke [163]. Both the Rolke and Feldman-Cousins methods are available for upper limits calculations in Stage 6 of VEGAS.

The maximum sensitivity of VERITAS (i.e., the weakest source that can be detected) defines what the mean upper limit on counts or flux will be. The 95% confidence level for counts or flux upper limit should cover the true DM annihilation signal 95% of the time for that particular cluster dataset. Therefore the true $<\sigma v>_{WIMP}$ should be less than $\langle\sigma v\rangle^{95\%\,CL}$ with 95% certainty. On an exclusion plot for a particular DM mass it is very likely that the true $<\sigma v>_{WIMP}$ would be plotted below $\langle\sigma v\rangle^{95\%\,CL}$, were the true $<\sigma v>_{WIMP}$ actually known.

The Li & Ma method mentioned in Section 2.6.5 is known by statisticians as a large-scale approximation to the likelihood ratio test statistic. The second page of the Rolke paper describes the likelihood method as follows. The full likelihood function can be written as:

$$L(\boldsymbol{\pi}, \boldsymbol{\theta}|X) = \prod_{i=1}^{n} f(X_i|\boldsymbol{\pi}, \boldsymbol{\theta}) \quad (C.1)$$

where L is the likelihood function, $\boldsymbol{\pi}$ is a set of model parameters to investigate (π_1, ... , π_k), $\boldsymbol{\theta}$ is a set of nuisance parameters to be minimized (θ_1, ... , θ_l) , $\boldsymbol{X}$ are independent observations (X_1, ... , X_n), and f is the probability mass function $f(X|\boldsymbol{\pi}, \boldsymbol{\theta})$ for each observation. To find confidence intervals with the full likelihood function, first propose the hypothesis H_0 that $\boldsymbol{\pi} = \boldsymbol{\pi}_0$. The corresponding null hypothesis H_a would say $\boldsymbol{\pi} \neq \boldsymbol{\pi}_0$. The ratio of the maximum likelihoods $H_0 : H_a$ is then:

$$\lambda(\boldsymbol{\pi}_0|X) = \frac{\max\{L(\boldsymbol{\pi}_0, \boldsymbol{\theta}|X);\ \boldsymbol{\theta}\}}{\max\{L(\boldsymbol{\pi}, \boldsymbol{\theta}|X);\ \boldsymbol{\pi}, \boldsymbol{\theta}\}} \quad (C.2)$$

where the ratio λ is called the profile likelihood. This is the same λ in equation 2.11 that gives the Gaussian significance. This approximation is valid because $-2 \ln \lambda$ approaches a χ^2 distribution with k d.o.f. for large numbers. Confidence intervals can be found by solving for the points where $-2 \ln \lambda$ increases by a factor defined by the confidence interval.

The Li & Ma method is well-suited for sources where the signal-to-noise ratio is large, hence the strong 5 σ threshold for a detection. At this level sources of error are dwarfed by the signal. For DM sources, however, this ratio is smaller and the method's predictive capabilities break down. Another concern of this method is that the quoted confidence levels are two-sided. A graph of the profile likelihood for a given confidence interval could include a region of negative signal rate. This makes no physical sense considering the way in which PMTs operate. Therefore it is necessary when deriving upper limits for observations without a detection to introduce a bounded limit. Figure C-1 demonstrates this behavior.

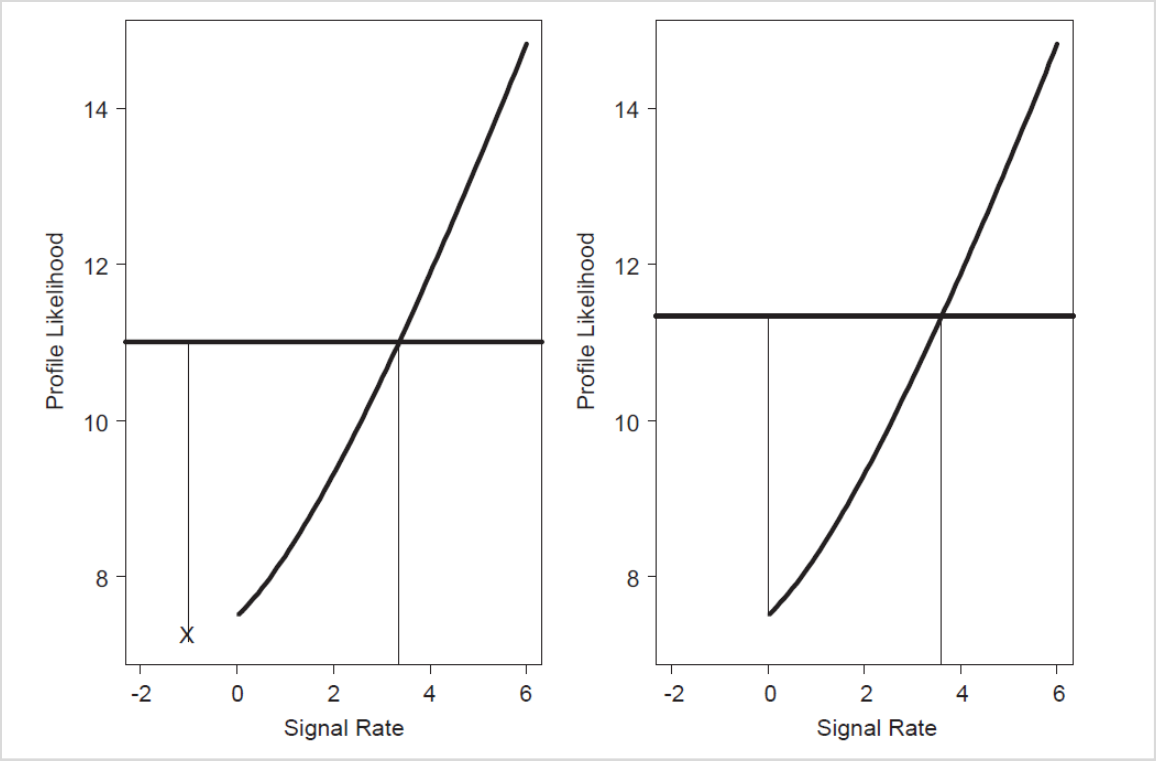

Figure C-1: Calculating bounded and unbounded intervals of the profile likelihood (credit: Wolfgang Rolke [136]). The caption on page 5 of the paper reads, "The case x = 2, y = 15 and τ = 5.0. In the left panel we use the unbounded likelihood method and find a 95% upper limit of 3.35. In the right panel using the bounded likelihood method the 95% upper limit is 3.6."

Page 3 of the Rolke paper handles these two considerations by taking them into account right at the beginning of the system of equations to be solved. Define a signal region *X* with *x* events and a background region *Y* with *y* events which are Monte Carlo simulated as Poisson distributions. Also include the Monte Carlo efficiency $= z/m$, the ratio of the surviving events to the total events simulated. The system can then be defined by three expressions:

$$X \sim Pois(e\mu + b),\ \ Y \sim Pois(\tau b),\ \ Z \sim Bin(m, e)\ \ (C.3)$$

where *Pois* and *Bin* are the Poisson distribution and the Binomial random variable, μ is the signal rate, b is the background rate, and τ is ratio of the probability that an event falls

in the background region to the probability that an event falls in the signal region (equivalent to the reciprocal of the VERITAS α parameter.) In this case the profile likelihood is found by fixing the signal rate and taking partial derivatives of the natural logarithm of the full likelihood function with respect to the background rate and efficiency:

$$\frac{\partial}{\partial b}\ln L(\mu, b, e|x, y, z) = \frac{x}{e\mu + b} - 1 + \frac{y}{b} - \tau = 0 \quad (C.4)$$

$$\frac{\partial}{\partial e}\ln L\,(\mu, b, e|x, y, z) = \frac{x}{e\mu + b} - \mu + \frac{z}{e} - \frac{m - z}{1 - e} = 0 \quad (C.5)$$

These nonlinear differential equations are solvable only via numerical integration techniques. The paper gives a similar treatment for Gaussian distributions instead of Poisson if the standard deviations of the background rate and efficiency are known. The rest of the paper discusses coverage by comparing the performance of this method to that of the Feldman-Cousins method, $-2\ln\lambda$, and the minimization code MINUIT [164]. Their conclusions were that a modest improvement in precision was realized, especially for the bounded method.

LIST OF REFERENCES

LIST OF REFERENCES

[1] Planck Collaboration, “Planck 2013 results. I. Overview of products and scientific results” arXiv:1303.5062 (2013)

[2] Ringwald, A., “Ultralight particle dark matter” arXiv:1310.1256 (2013)

[3] Freese, K., “Can scalar neutrinos or massive Dirac neutrinos be the missing mass?” *Phys. Lett. B*, **167**, 295 (1986)

[4] Milgrom, M., “A modification of the Newtonian dynamics as a possible alternative to the hidden mass hypothesis” *Astrophys. J.*, **270**, 365 (1983)

[5] Bekenstein, J. D., “Relativistic gravitation theory for the modified Newtonian dynamics paradigm” *Phys. Rev. D,* **70**, 083509 (2004)

[6] Conrad, J., Cohen-Tanugi, J., & Strigari, L., “WIMP searches with gamma rays in the Fermi era: challenges, methods and results” arXiv:1503.06348 (2015)

[7] Arkani-Hamed, N., et al., “A theory of dark matter” *Phys. Rev. D,* **79,** 015014 (2009)

[8] Cirelli, M., “Indirect searches for dark matter: a status review” arXiv:1202.1454 (2012)

[9] The VERITAS Collaboration, “VERITAS search for VHE gamma-ray emission from dwarf spheroidal galaxies” *Astrophys. J.*, **720**, 1174 (2010)

[10] Bovy, J., & Tremaine, S., “On the local dark matter density” *Astrophys. J.,* **756**, 89 (2012)

[11] Busha, M. T., et al., “Statistics of satellite galaxies around Milky Way-like hosts” *Astrophys. J.*, **743**, 117 (2011)

[12] Piffl, T., et al., “Constraining the Galaxy's dark halo with RAVE stars” *Mon. Not. Royal Astron. Soc.*, **445**, 3133 (2014)

[13] Zwicky, F., “Die rotverschiebung von extragalaktischen nebeln (the redshift of extragalactic nebulae)” *Helvetica Physica Acta*, **6**, 110 (1933)

[14] Merritt, D., “The distribution of dark matter in the Coma cluster” *Astrophys. J.*, **313**, 121 (1987)

[15] Rubin, V. C., Ford, W. K. Jr., & Thonnard, N., “Rotational properties of 21 Sc galaxies with a large range of luminosities and radii, from NGC 4605 (R = 4kpc) to UGC 2885 (R = 122 kpc)” *Astrophys. J.*, **238**, 471 (1980)

[16] van Albada, T. S., et al., “Distribution of dark matter in the spiral galaxy NGC 3198” *Astrophys. J.*, **295**, 305 (1985)

[17] Schneider, P., Kochanek, C. S., & Wambsganss, J., “Gravitational lensing strong, weak and micro” Springer, New York (2006)

[18] Clowe, D., et al., “A direct empirical proof of the existence of dark matter” *Astrophys. J. Lett.*, **648**, 109 (2006)

[19] Francis, M., “Lensing.png” http://galileospendulum.org/2011/07/14/seeing-through-gravitys-lens-transcript/ (2011)

[20] Rogerson, J., “Bullet Cluster: Evidence for Dark Matter” http://jesserogerson.com/2013/08/bullet-cluster-evidence-for-dark-matter/ (2013)

[21] Shaw, S., “detection1.png” http://www.quantumdiaries.org/author/sallys/ (2014)

[22] The CRESST Collaboration, “Results on low mass WIMPs using an upgraded CRESST-II detector” arXiv:1407.3146 (2014)

[23] CDMS Collaboration, “Silicon detector dark matter results from the final exposure of CDMS II” *Phys. Rev. Lett.*, **111**, 251301 (2013)

[24] Sanglard, V., et al., “Final results of the EDELWEISS-I dark matter search with cryogenic heat-and-ionization Ge detectors” *Phys. Rev. D*, **71**, 122002 (2005)

[25] Boccone, V. (for the ArDM Collaboration), “The ArDM project: A liquid argon TPC for dark matter detection” *J. Phys.: Conf. Ser.*, **160**, 012032 (2009)

[26] The XENON100 Collaboration, “Response of the XENON100 dark matter detector to nuclear recoils” *Phys. Rev. D,* **88**, 012006 (2013)

[27] Akerib, D., et al., “The Large Underground Xenon (LUX) experiment” *Nucl. Instrum. Meth. Phys. Res. A*, **704**, 111 (2013)

[28] Drees, M., & Gerbier, G. (for the Particle Data Group), “24. Dark Matter” http://pdg.lbl.gov/2013/reviews/rpp2013-rev-dark-matter.pdf (2013)

[29] Sembranos, J. A. R., et al., “Photon spectra from WIMP annihilation” *Phys. Rev. D*, **83**, 083507 (2011)

[30] The Fermi-LAT Collaboration, “The Large Area Telescope on the Fermi Gamma-ray Space Telescope mission” *Astrophys. J.*, **697**, 1071 (2009)

[31] The Nobel Foundation, “Enrico Fermi – Biographical” http://www.nobelprize.org/nobel_prizes/physics/laureates/1938/fermi-bio.html (2014)

[32] The Fermi-LAT Collaboration, “Fermi: Science - Instruments – LAT” http://fermi.gsfc.nasa.gov/science/instruments/table1-1.html (2011)

[33] Ciprini, S. (on behalf of the Fermi-LAT Collaboration), “The extragalactic sky in the Fermi era: some highlights” presented at the conference “Integral’s Journey through the High Energy Sky” INAF Observatory of Rome, Rome, Italy http://www.iaps.inaf.it/sz/integral2013/talks-posters/5-FermiLATExtragalSky_SCiprini_IntegralRomeOct2013.pdf (2013)

[34] The Fermi-LAT Collaboration, “Dark matter constraints from observations of 25 Milky-Way satellite galaxies with the Fermi Large Area Telescope” *Phys. Rev. D*, **89**, 042001 (2014)

[35] The Fermi-LAT Collaboration, “Search for gamma-ray spectral lines with the Fermi Large Area Telescope and dark matter implications” *Phys. Rev. D*, **88**, 082002 (2013)

[36] Simmonet, A., “article05_image01.jpg” http://www.symmetrymagazine.org/article/december-2009/fermis-excellent-adventure NASA/Sonoma State University (2009)

[37] H.E.S.S. Collaboration, “The H.E.S.S. Site in Namibia” http://www.mpi-hd.mpg.de/hfm/HESS/pages/about/site/ (2015)

[38] The Nobel Foundation, “Victor F. Hess – Biographical” http://www.nobelprize.org/nobel_prizes/physics/laureates/1936/hess-bio.html (2014)

[39] H.E.S.S. Collaboration, “High Energy Stereoscopic System” http://www.mpi-hd.mpg.de/hfm/HESS/pages/about/ (2015)

[40] Becherini, Y., Punch, M., & H.E.S.S. Collaboration, “Performance of HESS-II in multi-telescope mode with a multi-variate analysis” *AIP Conf. Proc.*, **1505**, 741 (2012)

[41] H.E.S.S. Collaboration, “Search for dark matter annihilation signatures in H.E.S.S. observations of dwarf spheroidal galaxies” *Phys. Rev. D*, **90**, 112012 (2014)

[42] Wakely, S., & Horan, D., “TeVCat Gamma-Ray Source Summary: Galactic Centre (VisPlot)” http://tevcat.uchicago.edu/?mode=1&showsrc=81 (2015)

[43] H.E.S.S. Collaboration, “Constraints on an annihilation signal from a core of constant dark matter density around the Milky Way center with H.E.S.S.” *Phys. Rev. Lett.*, **114**, 081301 (2015)

[44] van de Groenendaal, H., “HESS-smaller.jpg” http://www.ee.co.za/article/first-gamma-ray-pulsar-measured-southern-sky-ground-level.html (2014)

[45] MAGIC Collaboration, “MAGIC site | MAGIC” https://magic.mpp.mpg.de/newcomers/magic-site/ (2015)

[46] MAGIC Collaboration, “Home | MAGIC” https://wwwmagic.mpp.mpg.de/ (2015)

[47] MAGIC Collaboration, “Technical implementation | MAGIC” https://magic.mpp.mpg.de/newcomers/technical-implementation/ (2015)

[48] Cortina, J., et al. (for the MAGIC Collaboration), “Technical performance of the MAGIC telescopes” *Proc. 31st ICRC*, arXiv:0907.1211 (2009)

[49] Aleksić, J., et al. (MAGIC Collaboration), “Optimized dark matter searches in deep observations of Segue 1 with MAGIC” *J. Cosmol. Astropart. Phys.*, **02**, 008 (2014)

[50] MAGIC Collaboration, “Upper limit for gamma-ray emission above 140 GeV from the dwarf spheroidal galaxy Draco” *Astrophys. J.*, **679**, 428 (2008)

[51] MAGIC Collaboration, “Upper Limits on the VHE gamma-ray emission from the Willman 1 satellite galaxy with the MAGIC telescope” *Astrophys. J.*, **697**, 1299 (2009)

[52] MAGIC Collaboration, “MAGIC gamma-ray telescope observation of the Perseus cluster of galaxies: implications for cosmic rays, dark matter, and NGC 1275” *Astrophys. J.*, **710**, 634 (2010)

[53] Colafrancesco, S., Marchegiani, P., & Giommi, P., “Disentangling the gamma-ray emission of NGC 1275 and that of the Perseus cluster” *Astron. Astrophys.*, **519**, A82 (2010)

[54] ETH Institute for Particle Physics, “MAGIC-I.jpg?hires” Zurich http://www.ipp.phys.ethz.ch/research/magic_telescope (2013)

[55] HAWC Collaboration, “HAWC Site: Parque Nacional Pico de Orizaba” http://www.hawc-observatory.org/observatory/site.php (2015)

[56] HAWC Collaboration, “Water Cherenkov Tanks” http://www.hawc-observatory.org/observatory/tanks.php (2015)

[57] HAWC Collaboration, “The HAWC Gamma-Ray Observatory” http://www.hawc-observatory.org/ (2015)

[58] HAWC Group at UW-Madison, “HAWC Science” https://hawc.wipac.wisc.edu/hawc/science (2015)

[59] Abeysakara, A. U., et al., “Sensitivity of the High Altitude Water Cherenkov detector to sources of multi-TeV gamma rays” *Astropart. Phys*., **50**-**52**, 26 (2013)

[60] Abeysakara, A. U., et al. (HAWC Collaboration), “Sensitivity of HAWC to high-mass dark matter annihilations” *Phys. Rev. D*, **90**, 122002 (2014)

[61] HAWC Collaboration, “88677_web.jpg” http://www.eurekalert.org/pub_releases/2015-03/uom-hot031915.php (2015)

[62] Actis, M., et al. (CTA Consortium), “Design concepts for the Cherenkov Telescope Array” *Exp. Astron.*, **32**, 193 (2011)

[63] CTA Consortium, “CTA Instrument” https://portal.cta-observatory.org/Pages/Instrument.aspx (2015)

[64] CTA Consortium, “CTA Performance” https://portal.cta-observatory.org/Pages/CTA-Performance.aspx (2015

[65] Feng, J., “WIMPS: an overview, current constraints, and WIMP-like extensions” presented at the conference “8th Harvard-Smithsonian Conference on Theoretical Astrophysics” Cambridge, MA, http://www.cfa.harvard.edu/events/2014/sackler/index/talks/Harvard2014_Feng.pdf (2014)

[66] CTA Consortium, “Seeing the High-Energy Universe with the Cherenkov Telescope Array - The Science Explored with the CTA” *Astropart. Phys.*, **43**, 1-356 (2013)

[67] Pérez Díaz, G., “cta_concept_lr1.jpg” Instituto de Astrofísica de Canarias (Servicio Multimedia) http://www.observatorio-cta.es/images/Documentos/CTA%20Images/cta_concept_lr1.jpg (2012)

[68] Lefevre, C., “LHC: the guide” http://cds.cern.ch/record/1092437/files/CERN-Brochure-2008-001-Eng.pdf (2008)

[69] Jepsen, K., & Werners-Herron, A., “The search for dark matter at the LHC” http://www.symmetrymagazine.org/article/the-search-for-dark-matter-at-the-lhc (2014)

[70] Abercrombie, D., et al., “Dark matter benchmark models for early LHC run-2 searches: report of the ATLAS/CMS dark matter forum” arXiv:1507.00966 (2015)

[71] Abdallah, J., et al., “Simplified models for dark matter searches at the LHC” arXiv:1506.03116 (2015)

[72] Siegel, E., “lhc-sim.jpg” http://scienceblogs.com/startswithabang/2008/05/05/will-the-lhc-create-dark-matter/ (2008)

[73] Buckley, J., “CTA and the road ahead” presented at the conference “Trevorfest” Tucson, AZ, http://www.physics.utah.edu/trevorfest/TF2013/Speakers_files/09_jb_trevorfest_13.pdf (2013)

[74] Bringmann, T., Bergstrom, L., & Edsjo, J., “New gamma-ray contributions to supersymmetric dark matter annihilation” *J. High Energy Phys.*, **0801**, 049 (2008)

[75] National Radio Astronomy Observatory, “Inverse-Compton Scattering” http://www.cv.nrao.edu/course/astr534/InverseCompton.html (2015)

[76] Kawecki, P., “synchrotronradiationv2.gif” http://patrykkawecki.republika.pl/synchrotronradiation.htm (2015)

[77] Gonzales-Morales, A. X., Profumo, S., & Queiroz, F. S., “Effect of black holes in local dwarf spheroidal galaxies on gamma-ray constraints on dark matter annihilation” to appear in *Phys. Rev. D*, arXiv:1406.2424 (2014)

[78] Aliu, E., et al. (for the VERITAS Collaboration), “VERITAS deep observations of the dwarf spheroidal galaxy Segue 1” *Phys. Rev. D*, **85**, 062001 (2012)

[79] Einasto, J., “Kinematics and dynamics of stellar systems” *Trudy Astrofiz. Inst. Alma-Ata*, **5**, 87 (1965)

[80] de Vaucouleurs, G., “Recherches sur les nebuleuses extragalactiques (research on extragalactic nebulae)” *Annales d'Astrophysique*, **11**, 247 (1948)

[81] Navarro, J. F., Frenk, C. S., & White, S. D. M., “The structure of cold dark matter halos” *Astrophys. J.*, **463**, 563 (1996)

[82] Merritt, D., et al., “Empirical models for dark matter halos. I. nonparametric construction of density profiles and comparison with parametric models” *Astron. J.*, **132**, 2685 (2006)

[83] Dutton, A. A., & Maccio, A. V., "Cold dark matter haloes in the Planck era: evolution of structural parameters for Einasto and NFW profiles" arXiv:1402.7073 (2014)

[84] Giodini, S., et al., "Scaling relations for galaxy clusters: properties and evolution" arXiv:1305.3286 (2013)

[85] Sánchez-Conde, M. A., et al., "Dark matter searches with Cherenkov telescopes: nearby dwarf galaxies or local galaxy clusters?" *J. Cosmol. Astropart. Phys.*, **1112**, 011 (2011)

[86] Ghez, A. M., et al., "Measuring distance and properties of the Milky Way's central supermassive black hole with stellar orbits" *Astrophys. J.*, **689**, 1044 (2008)

[87] Cembranos, J. A. R., Gammaldi, V., & Maroto, A. L., "Spectral study of the HESS J1745-290 gamma-ray source as dark matter signal" *J. Cosmol. Astropart. Phys.*, **04**, 051 (2013)

[88] Daylan, T., et al., "The characterization of the gamma-ray signal from the central Milky Way: a compelling case for annihilating dark matter" arXiv:1402.6703 (2014)

[89] Nezri, E., et al., "γ-rays from annihilating dark matter in galaxy clusters: stacking vs single source analysis" *Mon. Not. Royal Astron. Soc.*, **425**, 477 (2012)

[90] Smith, A., & Beilicke, M. (for the VERITAS Collaboration), "VERITAS observations of the Galactic Center ridge above 2 TeV" arXiv:1508.06311 (2015)

[91] Reiprich, T. H., & Böhringer, H., "The mass function of an X-ray flux-limited sample of galaxy clusters" *Astrophys. J.*, **567**, 716 (2002)

[92] Voges, W., et al., "The ROSAT all-sky survey bright source catalogue" *Astron. Astrophys.*, **349**, 389 (1999)

[93] Yoon, J. H., et al., "A spectrophotometric search for galaxy clusters in SDSS" *Astrophys. J. Supp.*, **176**, 414 (2008)

[94] McCann, A., “VListBuilder” (internal VERITAS website tool) https://hastur.uchicago.edu/vlistbuilder (2015)

[95] National Astronomical Observatory of Japan/Astronomy Data Center, “Digitized Sky Survey Data Archive” http://dss.nao.ac.jp/ (2015)

[96] Smithsonian Astrophysical Observatory, “SAOImage DS9” http://ds9.si.edu/site/Home.html (2015)

[97] Cherenkov, P. A., “Visible emission of clean liquids by action of γ radiation” *Doklady Akad. Nauk SSSR,* **2**, 451 (1934)

[98] Longair, M., “High energy astrophysics” 2nd ed., Cambridge University Press, New York, (1992)

[99] de La Calle Pérez, I., & Biller, S. D., “Extending the sensitivity of air Cerenkov telescopes” *Astropart. Phys*., **26**, 69 (2006)

[100] Stanev, T., “High energy cosmic rays” 2nd ed., Praxis Publishing Ltd, Chichester, UK, (2004)

[101] Tsallis, C., Angos, J. C., & Borges, E. P., “Fluxes of cosmic rays: a delicately balanced stationary state” *Phys. Lett. A*, **310**, 372 (2003)

[102] Aloisio, R., Berezinsky, V., & Gazizov, A., “Transition for galactic to extragalactic cosmic rays” *Astropart. Phys.*, **39**, 129 (2012)

[103] JEM-EUSO, “2_energyspectrum_big.gif” http://jemeuso.riken.jp/en/about2.html (2015)

[104] Cronin, J. W., Gaisser, T. K., & Swordy, S. P., “Cosmic rays at the energy frontier” *Sci. Am.*, **276**, 44 (2007)

[105] Blandford, R., Simeon, P., & Yuan, Y., “Cosmic ray origins: an introduction” *Nucl. Phys. B (Proc. Suppl.)*, **256**, 9 (2014)

[106] Poirier, J., Roesler, S., & Fassò, A., "Distributions of secondary muons at sea level from cosmic gamma rays below 10 TeV" *Astropart. Phys.*, **17**, 441 (2002)

[107] Meurer, C., et al., "Muon production in extensive air showers and its relation to hadronic interactions" *Czech. J. Phys.*, **56**, A211 (2006)

[108] "Atmospheric Cherenkov telescopes for high-energy γ-ray astronomy" (VERITAS public website) http://veritas.sao.arizona.edu/about-veritas-mainmenu-81/atmospheric-cherenkov-technique-and-veritas-technologies-mainmenu-87 (2015)

[109] Hillas, A. M., "Cerenkov light images of EAS produced by primary gamma" *Proc. 19th ICRC*, 445 (1985)

[110] "VERITAS Specifications" (VERITAS public website) http://veritas.sao.arizona.edu/about-veritas-mainmenu-81/veritas-specifications-mainmenu-111 (2015)

[111] Davies, J. M., & Cotton, E. S., "Design of the quartermaster solar furnace" *J. Solar Energy Sci. and Eng.*, **1**, 16 (1957)

[112] Holder, J., et al., "The first VERITAS telescope" *Astropart. Phys.*, **25**, 391 (2006)

[113] Roache, E., et al., "Mirror facets for the VERITAS telescopes" *Proc. 30th ICRC*, **3**, 1397 (2008)

[114] McCann, A., et al., "A new mirror alignment system for the VERITAS telescopes" *Astropart. Phys.*, **32**, 322 (2010)

[115] Galante, N., & Gibbs, K., "File:NewArray.jpg" (internal VERITAS website) https://veritas.sao.arizona.edu/wiki/index.php/File:NewArray.jpg (2009)

[116] Kieda, D. B. (for the VERITAS Collaboration), "The gamma ray detection sensitivity of the upgraded VERITAS observatory" *Proc. 33rd ICRC*, arXiv:1308.4849 (2013)

[117] Holder, J., “File:On track3.jpg” (internal VERITAS website) https://veritas.sao.arizona.edu/wiki/index.php/File:On_track3.jpg (2012)

[118] “Quantum efficiency test results of the VERITAS PMTs” (internal VERITAS website) https://veritas.sao.arizona.edu/wiki/index.php/Quantum_Efficiency_Test_Results_of_the_VERITAS_PMTs (2015)

[119] “Moonlight observations” (internal VERITAS website) https://veritas.sao.arizona.edu/wiki/index.php/Moonlight_Observations (2015)

[120] “Study of the L1 trigger threshold” (internal VERITAS website) https://veritas.sao.arizona.edu/wiki/index.php/Study_of_L1_trigger_threshold (2012)

[121] Anderson, J. T., et al., “Commissioning and performance of a fast level-2 trigger system at VERITAS” In Real Time Conference (RT), *18th IEEE-NPSS*, 1, (2012)

[122] Cogan, P. (for the VERITAS Collaboration), “Analysis of Flash ADC data with VERITAS” *Proc. 30th ICRC* (2007)

[123] Hays, E., “VERITAS data acquisition” (poster) presented at *30th ICRC* (2007)

[124] Brun, R., & Rademakers, F., “ROOT – an object oriented data analysis framework” *Nucl. Instrum. Meth. Phys. Res. A*, **389**, 81 (1997)

[125] Offline Analysis Working Group, “VEGAS Version 2.5” (internal VERITAS website) https://veritas.sao.arizona.edu/OAWGwiki/index.php/2.5 (2015)

[126] Hanna, D., McCann, A., & Nikkinen, L., “An LED-based flasher system for VERITAS” (internal VERITAS memo) McGill University https://veritas.sao.arizona.edu/wiki/images/1/14/McGill-LED-Flasher-System.pdf (2009)

[127] Weekes, T., et al., “Observation of TeV gamma rays from the Crab nebula using the atmospheric Cerenkov imaging technique” *Astrophys. J.*, **342**, 379 (1989)

[128] Gall, D., “Multi-wavelength studies of VHE gamma-ray blazars” (VERITAS thesis) Purdue University http://veritas.sao.arizona.edu/documents/Theses/Gall_Thesis.pdf (2010)

[129] Şentürk, G., “The disp method for analysing large zenith angle gamma-ray data” *Proc. 32nd ICRC* (2011)

[130] Millis, J., “Observation of high energy emission from pulsar wind nebulae using VERITAS” (VERITAS thesis) Purdue University http://veritas.sao.arizona.edu/documents/Theses/MillisThesis.pdf (2008)

[131] Krawczynski, H., et al., “Gamma hadron separation methods for the VERITAS array of four imaging atmospheric Cherenkov telescopes” *Astropart. Phys.*, **25**, 380 (2006)

[132] Zitzer, B. J., “Template background method” presented at the conference “VERITAS Summer Collaboration Meeting” Galway, Ireland, https://veritas.sao.arizona.edu/wiki/images/b/b4/GalwayTalkB4.pdf (2015)

[133] Zitzer, B. J., & Geringer-Sameth, A., “Crescent background model analysis” (Internal VERITAS memo) Argonne National Laboratory https://veritas.sao.arizona.edu/wiki/images/8/83/Zitz_CresentBGMemo_v3.pdf (2012)

[134] Daum, A., et al., “First results of the performance of the HEGRA IACT” *Astropart. Phys.*, **8**, 1 (1997)

[135] Li, T., & Ma, Y., “Analysis methods for results in gamma-ray astronomy” *Astrophys. J.*, **272**, 317 (1983)

[136] Rolke, W., et al., “Limits and confidence intervals in the presence of nuisance parameters” *Nucl. Instrum. Meth. Phys. Res. A*, **551**, 493 (2005)

[137] Krause, M., Pueschel, E., & Maier, G., "Boosted decision trees for the gamma-hadron-separation in eventdisplay" (internal VERITAS website) https://veritas.sao.arizona.edu/wiki/images/2/2e/BDT-GammaHadron-Note.pdf (2015)

[138] Catena, R., & Ullio, P., "A novel determination of the local dark matter density" *J. Cosmol. Astropart. Phys.*, **08**, 004 (2010)

[139] Lemoine-Goumard, M., Degrange, B., & Tluczykont, M., "Selection and 3D-reconstruction of gamma-ray-induced air showers with a stereoscopic system of atmospheric Cherenkov telescopes" *Astropart. Phys.*, **25**, 195 (2006)

[140] Lafferty, G. D., & Wyatt, T. R., "Where to stick your data points: the treatment of measurements within wide bins" *Nucl. Instrum. Meth. Phys. Res. A*, **355**, 541 (1995)

[141] Sembroski, G., "Spectrum Analysis" (internal VERITAS website) https://veritas.sao.arizona.edu/wiki/index.php/Spectrum_Analysis (2010)

[142] Tucci, J. V., Finley, J. P., & Zitzer, B. J. (for the VERITAS Collaboration), "Upper limits on dark matter in dwarf spheroidal galaxies at VERITAS" (poster) presented at the conference "HEAD 14th Meeting" Chicago, IL (2014)

[143] Sjöstrand, T., et al., "PYTHIA" http://home.thep.lu.se/~torbjorn/Pythia.html (2015)

[144] Geringer-Sameth, A., Koushiappas, S. M., & Walker, M., "Dwarf galaxy annihilation and decay emission profiles for dark matter experiments" arXiv:1408.0002 (2014)

[145] "VERITAS Run Log Generator" (internal VERITAS website) https://veritasm.sao.arizona.edu/DQM/loggen.html (2015)

[146] Vaisala, "CL51 Ceilometer for High-Range Cloud Height Detection" http://veritas.sao.arizona.edu/documents/CL51_B210861EN-A-LoRes.pdf (2010)

[147] The VERITAS Collaboration with Pfrommer, C., & Pinzke, A., "Constraints on cosmic rays, magnetic fields, and dark matter from gamma-ray observations of the Coma cluster of galaxies with VERITAS and Fermi" *Astrophys. J.*, **757**, 123 (2012)

[148] Charbonnier, A., Combet, C., & Maurin, D., "CLUMPY: a code for γ-ray signals from dark matter structures" *Comp. Phys. Comm.*, **183**, 656 (2012)

[149] Duffy, A. R., et al., "Dark matter halo concentrations in the Wilkinson Microwave Anisotropy Probe year 5 cosmology" *Mon. Not. Royal Astron. Soc.*, **390**, L64 (2008)

[150] Piffaretti, R., et al., "The MCXC: a meta-catalogue of x-ray detected clusters of galaxies" *Astron. Astrophys.*, **534**, A109 (2011)

[151] Bullock, J. S., et al., "Profiles of dark haloes: evolution, scatter and environment" *Mon. Not. Royal Astron. Soc.*, **321**, 559 (2001)

[152] Zhao, H., "Analytical models for galactic nuclei" *Mon. Not. Royal Astron. Soc.*, **278**, 488 (1996)

[153] Bonnivard, V., et al., "CLUMPY: Jeans analysis, γ-ray and neutrino fluxes from dark matter (sub-)structures" arXiv:1506.07628 (2015)

[154] Sánchez-Conde, M. A., & Prada, F., "The flattening of the concentration-mass relation towards low halo masses and its implications for the annihilation signal boost" *Mon. Not. Royal Astron. Soc.*, **442**, 2271 (2014)

[155] Cirelli, M., "PPPC 4 DM ID - A Poor Particle Physicist Cookbook for Dark Matter Indirect Detection" http://www.marcocirelli.net/PPPC4DMID.html (2015)

[156] Cirelli, M, et al., "PPPC 4 DM ID: a poor particle physicist cookbook for dark matter indirect detection" *J. Cosmol. Astropart. Phys.*, **1103**, 051 (2011)

[157] Ciafaloni, P., et al., "Weak corrections are relevant for dark matter indirect detection" *J. Cosmol. Astropart. Phys.*, **1103**, 019 (2011)

[158] Bähr, M., et al., "Herwig++ physics and manual" arXiv:0803.0883 (2008)

[159] Kertzman, M. P., & Sembroski, G. H., “Computer simulation methods for investigating the detection characteristics of TeV air Cherenkov telescopes” *Nucl. Instrum. Meth. Phys. Res. A*, **343**, 629 (1994)

[160] Resvanis, L. K., et al., “The Haleakala gamma ray observatory” *Nucl. Instrum. Meth. Phys. Res. A*, **269**, 297 (1988)

[161] Maier, G. (for the VERITAS Collaboration), “Monte Carlo studies of the VERITAS array of Cherenkov telescopes” *Proc. 30th ICRC* (2007)

[162] Feldman, G. J., & Cousins, R. D., “Unified approach to the classical statistical analysis of small signals” *Phys. Rev. D*, **57**, 3873 (1998)

[163] ROOT Developers, “TRolke Class Reference” https://root.cern.ch/doc/master/classTRolke.html (2015)

[164] James, F., “Interpretation of the shape of the likelihood function around its minimum” *Comp. Phys. Comm.*, **20**, 29 (1980)

VITA

VITA

James Tucci was born in La Jolla, California on July 22, 1988 to his parents, Lisa and Stephen Tucci. In 2006 James graduated from The Bishop's School in La Jolla, California. He spent the next four years at the University of Notre Dame in Notre Dame, Indiana where he received a Bachelor of Science degree in Advanced Physics in 2010. He then went on to Purdue University in West Lafayette, Indiana for the next six years, earning a Master of Science degree in High Energy Astrophysics in 2013 and later his PhD in 2016.

James and his wife Elissa were married on September 12, 2015. He is in the process of applying for postdoctoral research positions that begin in fall 2016.